Carnegie Mellon University

CARNEGIE INSTITUTE OF TECHNOLOGY

THESIS

SUBMITTED IN PARTIAL FULFILLMENT OF THE REQUIREMENTS

FOR THE DEGREE OF Doctor of Philosophy

TITLE Optimization, Dynamics and Stability of Non-Linear Separation Processes

PRESENTED BY Max Fahrenkopf

ACCEPTED BY THE DEPARTMENT OF

Chemical Engineering

JAMES SCHNEIDER	4/1714
CO-ADVISOR	DATE
B. ERIK YDSTIE	4/17/14
CO-ADVISOR	DATE
LORENZ BIEGLER	4/17/14
LORENZ BIEGLER, DEPARTMENT HEAD	DATE

APPROVED BY THE COLLEGE COUNCIL

VIJAYAKUMAR BHAGAVATULA	4/17/14
DEAN	DATE

Optimization, Dynamics and Stability of Non-Linear Separation Processes

Submitted in partial fulfillment of the requirements for

the degree of

Doctor of Philosophy

in

Chemical Engineering

Max A. Fahrenkopf

B.S., Chemical Engineering, University of Wyoming

Carnegie Mellon University
Pittsburgh, PA

May, 2014

Acknowledgments

"She did not know the nature of her loneliness. The only words that named it were: This is not the world I expected."

– Ayn Rand, *Atlas Shrugged*

This thesis is not at all what I expected it would be. When I was an undergraduate, my vision of chemical engineering was very well defined. I thought then that my PhD work would be a direct extension of my undergraduate vision of chemical engineering. But instead of finding the clear extension of undergraduate chemical engineering, I found all the grey area surrounding the theory I thought I knew well. I found that most of what I had learned before was only applicable in the simplest of cases and that solving real problems took a lot of time. In the end this thesis was not at all what I expected, but in a way it was everything I expected just not the way I expected it to happen.

This adventure began with a lot of help from Prof. Jim Schneider. Through group meetings and presentations, From Jim, I learned of the art of clarity and the sovereignty of physics. I had learned that satisfied KKT conditions is apparently not what makes a physical system optimal. This took me longer than I care to admit to understand. Later in my PhD, Erik Ydstie showed me how to find my way back after getting "lost in the forest". I would like to express my deepest gratitude to both of my advisers, Jim and Erik, for guiding me through this work. I would also like to thank my committee: Larry Biegler, Aditya Khair, and especially Tamal Mukherjee. Tamal has been effectively my third co-adviser and has helped me considerably in this work. This research was financially supported by the CFD Research Corporation under NIH Grant 2R44HG00429002. Additional funding was provided by NSF Grant 0932536, the Center for Advanced Process Decision-making at Carnegie

Mellon University, and the John E. Swearingen fellowship.

I would also like thank my friends for their support through this work. I would especially like to thank Anthony Kotula for helping me with some scaling analysis and for making me feel like I was never quite working enough, John Goldman for our conversations about DNA electrophoresis and many late night adventures, Sayta Amaran for our great conversations in the office, Matt Reichert for getting me out of bed every morning for 7 am weights and chatting with the FMS guys, Reza Rock for laughing at my awful jokes, Tim McFarland for putting up with me as a roommate (and inadvertently introducing me to Erin), John Riley for beating me at racquetball every single time, Ben Yezer for not winning at racquetball as often as John, Yash Puranik for being the Marathi Hammer, German Oliveros for his easy going nature, Blake Rawlings for pushing me out of the raft during my bachelor party, thanks Blake, and Jonathan Chung for our conversations over lunch about equity trading.

Finally none of this would have been possible without the support of my family. Thank you Diego, Sasha, Ingrid, Axel, Dad, Mom, Papa, Cherie and Michael for everything. Most of all I would like to thank my beautiful wife Erin. This thesis would not have been the same without her unending (and often misunderstood) encouragement. I cannot wait to go through all the future fads in eating and pop music with you my love.

Abstract

In this thesis we develop a non convex non-linear programming problem that determines the minimum run time of a rapid, gel-free DNA separation technique called micelle end-labeled free solution electrophoresis (ELFSE). Micelle ELFSE is typically performed in capillary electrophoresis where the capillary length, electric field strength, and micelle drag tag size are the primary tuning variables. Using optimization, we demonstrate that capillary electrophoresis can be used to separate up to 600 bases in under 50 minutes. A significant improvement in performance is then shown to be achievable by using parallel capillaries which can separate up to 600 bases in under 5 minutes. Even more improvement is shown to be possible by using alternative separation modes, such as using an EOF counter-flow which enables 600 bases to be separated in under 4.5 minutes using a single capillary, and microfluidics utilizing snapshot detection to yield 600 bases in under 3.5 minutes. Long DNA, above 5000 bases, is particularly challenging to separate quickly. Using Brownian dynamics simulations we show the viability of integrating two DNA separation techniques: end-labeled DNA electrophoresis and entropic trapping. We present simulation results that demonstrate improved performance of the integrated device over entropic trapping alone. Brownian dynamics simulations are very computationally expensive, often taking over 24 hours per data point. We present an acceleration technique called projective integration which may be useful for simulations with a large amount of integration steps. We show that, using a model built from linear regression, periodic extrapolations can be used to decrease computational time. Finally we present the stability of the multi-component distillation column. We demonstrate, through the use of thermodynamics, that the distillation column is asymptotically stable when using pressure, temperature, and level control on the reboiler and condenser.

Contents

List of Figures

Chapter 1

Introduction

Transport and separation problems described by non-linear systems can often be difficult to model by simple closed form equations. This makes the further analysis, such as of optimization and stability analysis, difficult to perform. Despite this difficulty, significant benefits can be derived by application of these systems level analysis techniques. Global optimization, for instance, has been used with success in applications including water treatment [1], protein folding [2], pooling and blending [3], robust process control [4], and the prediction of phase and chemical equilibrium [5] just to name a few with more details found in a review by [6].

The algebraic models that describe the many different transport processes vary significantly in complexity and structure. Given a general non-convex, non-linear programming (NLP) problem, the task of rigorously and reliably finding the global minimum is a challenging problem. Non-convex functions may have multiple local minima. Rigorous methods for solving these problems to global optimality rely on spatial branch and bound techniques to manually search the feasible region of the problem [7–9]. A spatial branch and bound algorithm is designed to reduce the gap between the upper bound,

the smallest of the known local solutions, and the lower bound, the solution to a convex relaxation of the original problem. The efficiency of state-of-the-art global solvers αBB [7], BARON [8, 10], LindoGLOBAL [11], etc. is realized by utilizing tight convex relaxations for known functional forms such as bilinears, xy, [12, 13], linear fractionals, x/y, [14, 15] and concave univariates such as a square root function, $\sqrt{x}$, [16]. Symbolic reformulation [16] and reformulation-linearization techniques for polynomial terms [17], for instance, can also be used to restructure the original problem to further ensure a tight convex relaxation. With these principles in mind, global optimization becomes tractable for many applications.

The analysis of system dynamics and stability can also lead to significant improvements in several transport and separation processes. Some of these applications include the control of distillation columns [18–20], enhanced oil recovery [21–23], and the control of colloidal and Brownian particles [24–26]. While the dynamics and stability properties of linear systems have, for the most part, been well characterized [27], non-linear systems remain difficult to analyze. Non-linear dynamical system analysis often makes use of Lyapunov stability theory, dissipativity, or passivity to show if a system is stable [28], although the use of these techniques hinges on the ability to satisfy specific inequalities that are difficult to guarantee.

The work in this thesis began with the systems level analysis of a recently developed micelle end-labeled DNA separation technique designed for rapid length based separation of DNA [29, 30]. Length based separation is an important step in many DNA analysis techniques such as short-tandem repeat analysis [31, 32], mutation detection for cancer diagnosis [33–35] and sequencing [36–38]. Typically length based DNA separation is completed using gel electrophoresis, but gels are inherently slow due in part to the large

amount of friction they impart onto the DNA. A Gel-free alternative called end-labeled free-solution electrophoresis (ELFSE) [39, 40] (also referred to as free-solution conjugate electrophoresis (FSCE) [35, 38]) is much faster, resolving DNA lengths up to 265 bases in 30 minutes, with single-base resolution. These methods require that a highly monodisperse drag-tag be attached to the end of the DNAs in the sample. A variation of this technique is micelle-ELFSE electrophoresis [29, 30], which instead uses ensembles of transiently end-attached surfactant micelles as drag-tags. Here, stochastic variations in micelle size provide a highly uniform drag, despite a polydispersity of micelle size in the overall sample. Micelle-ELFSE allows the size of the drag-tag to be chosen simply by using buffers with a desired micelle size, without further chemical modification. This presents an opportunity to decrease run times by performing separations of longer DNA using larger drag-tags, and those for shorter DNA using shorter drag-tags. Another design trade-off is presented by the choice of electric field and capillary length. Use of high electric fields will give fast run times, but will cause excessive band broadening due to insufficient micelle size-sampling.

We demonstrate how to formulate a conventionally detected capillary electrophoresis DNA separation problem as a non-convex NLP in chapter 2. In conventionally detected capillary electrophoresis, the primary design variables for micelle-ELFSE are the capillary length, the applied voltage, and the size of the micelle. The optimization reveals that DNA up to 600 bases can be resolved in under 50 minutes. Resolving DNA of this length requires a large drag tag. It is therefore beneficial to use parallel capillaries to split the separation task. The non-convex NLP is easily reposed for parallel capillaries allowing us to identify what micelle drag tags to use in which capillaries. The optimization shows that using parallel capillaries can reduce the run time to

less than 5 minutes for separating 600 bases of DNA.

In chapter 3 we investigate the viability of alternative detection modes that may be used to speed up the micelle-ELFSE DNA separation method. In conventionally detected capillary electrophoresis, the elution order for DNA is from long to short. Short DNA, which is tagged with a large micelle, will take significantly longer to migrate to the detector. We therefore propose using a counter-flow to reverse the elution order of the DNA lengths. Optimization of the counter-flow enables up to 600 bases of DNA to be separated in under 4.5 minutes using a single capillary. Snap-shot detection is another method that can be used to speed up the micelle ELFSE DNA separation. Snap-shot detection observes every DNA length in the separation channel at some instant in time. Snap-shot detection, however, typically requires the use a motorized stage to allow scanning of the separation channel. This limits the overall area over which the separation can take place, requiring the use of microfluidic devices with turns to be able to fit long channel lengths into small areas. We show that a non-convex NLP can lead to the optimal design of either a serpentine or a spiral to separate 600 bases of DNA in under 3.5 minutes.

Long DNA can be particularly difficult to separate according to length. Once the DNA length becomes long enough it undergoes bias reptation in a gel and the length based mobility of DNA is lost [41, 42]. Pulsed field gel electrophoresis can be used to separate long DNA although it can take up to 24 hours [43–46]. Modern separation techniques employ microfabricated obstacle course, such as entropic traps [47–49], nanofilter arrays [50–52], nanopits [53, 54], and nanopost arrays [55–58], can separate long DNA on the order of minutes. While microfabricated devices are capable of dramatic speed up in long DNA separation, they are difficult to tune. Brownian dynamics simulations can by employed to offer some insights in the design process [58–62]

although the computational times can often exceed 24 hours which precludes the use of direct optimization.

In chapter 4 we use Brownian dynamics simulations to show how end-labeled DNA separation can be integrate in to entropic trap devices to improve the separation performance. Entropic traps and end-labeled DNA electrophoresis are compatible separation methods as DNA elutes long to short in both methods. We demonstrate that the resolution of this novel integrated separation techniques is significantly improved with the increasing size of the drag tag. The physical reason for why such an improvement is observed is elucidate through the use of a scaling analysis. We propose that the drag tag effects the diffusivity of the DNA such that short DNA diffuses at significantly longer time scales over long DNA.

Design on novel DNA separation methods using Brownian dynamics simulations is a slow process due to the large number of states, integration steps, and realizations required to get good estimates of the statistical distribution of the results. Unfortunately it is also often difficult to derive closed form algebraic models for these novel separation methods, such that optimization cannot be easily applied. It may then be useful to utilize an acceleration technique such that the simulations can be more rapidly executed. One such acceleration technique is equation-free projective integration [63–65]. After some work with equation-free projective integration it was clear that it is not the ideal technique to accelerate Brownian dynamics simulations. Along the way, however, we discovered some general improvements to the projective integration method.

In chapter 5 we purpose a novel projective integration technique that breaks with the equation-free method. Projective integration uses a two coupled integration methods to rapidly integrate a problem with both fast and slow

dynamics. First a detailed inner-integrator is used to damp out any slow dynamics. Next the outer-integrator is used to extrapolate out over a long horizon. The inner-integrator is then restarted and the process continues until the desired integration is completed. The standard, equations-free method makes the extrapolation using a model derived using finite-difference calculations. With this method it is difficult to account for the interaction between states and estimate error propagation. In our proposed method, we use linear regression to build a model which can then be used in the outer-integration step. An error bound can be derived from the model which allows for the adaptive update of the projection horizon. We demonstrate that our proposed projective integration technique works well for small ordinary differential equations, but does not significantly accelerate large differential equations. This likely stems from the reduced predictive accuracy for models that found from under-determined linear regression, which is typically required when the number of states is large. Projective integration works particularly well for stable (or contracting) non-linear systems.

Analysis of stability of non-linear systems is important for design of control systems. In chapter 6 we demonstrate the use of thermodynamics to show stability of the multi-component distillation column. We make us of an availability function [66] to build a Lyapunov function. The Lyapunov function reveals explicitly what controls are required for asymptotic stability. Although previous work has demonstrated stability of binary system [19, 20], we believe this is the first time a general stability analysis has been successful for the multi-component system.

Chapter 2

Micelle End-labeled DNA Separation using Conventional Detection Modes

In this chapter we discuss the optimal length based separation of micelle end-labeled DNA in single and parallel capillaries. Single and parallel capillary electrophoresis systems are readily available from vendors such as Beckman-Coulter and ABI. In order to achieve minimum run time we treat the capillary lengths, applied electric field strength, and micelles size as design variables. We select these three parameters because they are easy to change by the user and their impact is significant on the quality and run time of the separation. An important implication associated with choosing the micelle size as a design variable is that the micelle sizes must be previously characterized from a known surfactant type, mixture, and concentration. Specifically, we make no attempt to find the identify the appropriate surfactants to use to achieve minimum run time separations.

We begin this chapter with a general discussion of minimum run time DNA

separations. We then focus on the micelle end-labeled DNA separation problem. The optimization reveals general run conditions to yield fast DNA separations, such as using the shortest capillaries and maximum voltage available. The optimization allows for quick prototyping of different run configurations such a parallel capillaries. We show that the run time of the separation can be significant reduced by using parallel capillaries in the optimal configuration. Other configurations for rapid DNA separation by micelle end-labeled electrophoresis will be discussed in the next chapter.

2.1 General DNA Separation Problem

Length based separation of DNA is successful when the DNA length of interest is resolved from the other lengths. A typical apparatus for completing this task is a capillary electrophoresis system with a diagram shown in figure 2.1. In capillary electrophoresis charge molecules separate over some distance l_D driven by an electric potential difference V_{app}. The charged molecules separate as they migrate at different rates down the capillary at rate dictated by their electrophoretic mobility

$$u = \mu E \tag{2.1}$$

where u is the analyte velocity, μ is the electrophoretic mobility and E is the applied electric field given by

$$E = \frac{V_{app}}{l_C} \tag{2.2}$$

where V_{app} is the applied voltage and l_C is the total length of the capillary. Molecules with naturally differing electrophoretic mobilities μ can be separated in free-solution capillary electrophoresis without the addition of a sepa-

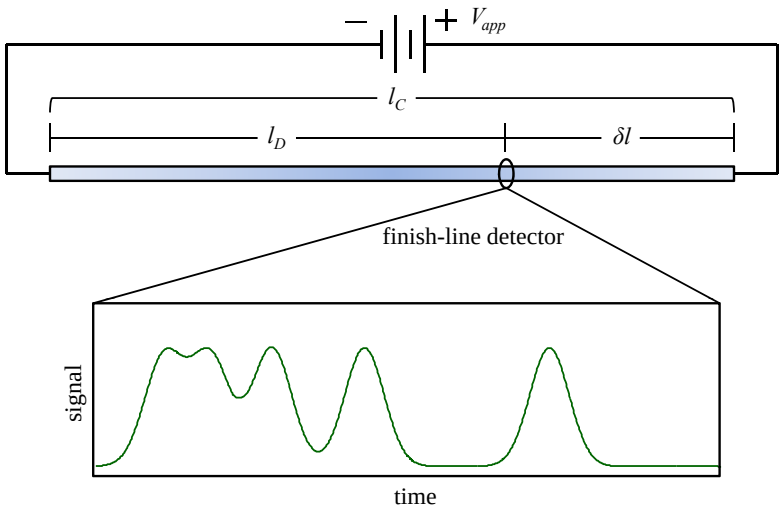

Figure 2.1: Schematic of a capillary electrophoresis system. DNA is separated and detected after a distance l_D away from injection with throughput controlled by the applied electric field E which is the applied voltage V_{app} over the total capillary length l_C.

ration matrix. Many interesting molecules such as DNA, however, have electrophoretic mobilities μ that scale independently of length [67]. The length independent scaling can be broken with the addition of separation matrix to the capillary. Gel electrophoresis is commonly used to separate DNA but recent advances in end-labeled free-solution electrophoresis has identified an alternatives means of breaking the length independent scaling of the electrophoretic mobility [38–40]. The addition of a uncharged drag tag to DNA acts as a molecular parachute and has the advantage of significant speed-up over typical gel electrophoresis runs.

Separation of DNA using capillary electrophoresis is a semi-batch process, i.e. DNA is first injected as one plug, then the electric field is applied and the analytes migrate down the capillary and separate according to their differing mobilities μ and create separate concentration bands. When the concentration bands are detected they are observed as Gaussians with some full-width at half-maximum w_i and mean migration time t_i. The width of the Gaussian

signal is the result of various disturbances on the velocity of each analyte i. The quality of a length based separation is quantified by the resolution factor for each analyte R_i. The resolution between two bands is the ratio of the Gaussians' broadness to their spacing

$$R_i = \frac{w_{i+1} + w_i}{2\,|t_{i+1} - t_i|} \tag{2.3}$$

where w_i is the full width at half-maximum of the Gaussian, and t_i is the mean migration time for the analyte i. For a Gaussian profile, the full width at half-maximum is described in terms of its variance, σ_i^2, such that $w_i = 2\sqrt{2\ln(2)\sigma_i^2}$. When the resolution factor in Eq. (2.3) is less than 1.5 then two concentration bands are considered resolved from each other.

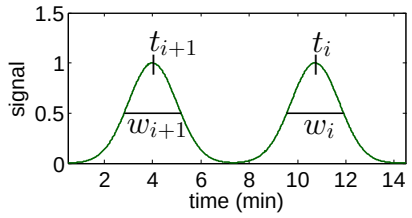

Figure 2.2: Two resolved Gaussians

The run conditions such as V_{app}, l_C and properties of the separation matrix, such as gel concentration, directly determine both the run time and the resolution for each analyte i. The separation is complete when all analytes i are resolved. The optimal run conditions for length-based separations using capillary electrophoresis can be found by solving the optimization problem Eq.

(2.4)

$$
\begin{aligned}
\min_{\mathbf{z}} \quad & t_{run}(\mathbf{z}) = \max_{i \in I}\{t_i(\mathbf{z})\} \\
\text{s.t.} \quad & R_i(\mathbf{z}) \leq 1.5, \quad \forall i \in I \\
& R_i(\mathbf{z}) = \frac{w_{i+1}(\mathbf{z}) + w_i(\mathbf{z})}{2\left|t_{i+1}(\mathbf{z}) - t_i(\mathbf{z})\right|} \\
& w_i(\mathbf{z}) = 2\sqrt{2\ln(2)\sigma_i^2(\mathbf{z})} \\
& \sigma_i^2(\mathbf{z}) = s_i(\mathbf{z}) \\
& t_i(\mathbf{z}) = h_i(\mathbf{z}) \\
& \mathbf{g}(\mathbf{z}) \leq 0 \\
& \mathbf{z} \in \mathbb{R}^n
\end{aligned}
\tag{2.4}
$$

where $s_i : \mathbb{R}^n \to \mathbb{R}$ is the model for the variance generation during the separation, $h_i : \mathbb{R}^n \to \mathbb{R}$ is the model for the migration time and $\mathbf{g} : \mathbb{R}^n \to \mathbb{R}^m$, $m < n$ are the constraints on the system and the states $\mathbf{z}$. The run time is the longest migration time of all the analytes, $t_{run} = \max_{i \in I}\{t_i\}$ which is typically known to correspond to either the smallest or largest analyte depending on the separation method.

The models in the optimization problem Eq. (2.4) define two important features of the DNA separation problem: t_i the migration time and σ_i^2 the variance generated for each analyte i. Both of these functions dependent of the separation mode used. In the next section, we will discuss some of the sources of variance that occur during capillary electrophoresis.

2.2 Minimum run time DNA separation using micelle ELFSE

The optimization framework developed in the previous section can be utilized to find the optimal run conditions for micelle end-labeled free-solution elec-

trophoresis (ELFSE). Micelle ELFSE is a rapid DNA separation method that is an attractive alternative to gel electrophoresis, since gels can be slow and difficult to use. The optimization model in Eq. (2.4) requires definition of migration time t_i and the variance σ_i^2 for each analyte i. In this section we discuss the micelle ELFSE model in detail and how it fits into our optimization framework.

In free-solution, DNA undergoes electrophoresis at a rate independent of its length. End-labeled free-solution electrophoresis (ELFSE) is a length based separation method that applies additional hydrodynamic friction to each DNA length through an end-attached drag tag which breaks the length independent scaling of DNA electrophoresis. From Eq. (2.1), the electrophoretic mobility dictates the velocity for each DNA length L. The electrophoretic mobility of the DNA drag-tag complex is given by

$$\mu = \mu_0 \left(\frac{L}{L + \alpha} \right) \tag{2.5}$$

where μ_0 is the free-solution mobility of DNA, L is the length of DNA in terms of bases and α is the size of the drag tag in units of the number of DNA bases with equivalent hydrodynamic drag [39, 68]. The migration time for each DNA length L is then given by using Eq. (2.1) and Eq. (2.5) so that

$$t = \frac{l_D}{\mu_0 E} \left(1 + \frac{\alpha}{L} \right) \tag{2.6}$$

where l_D is the length to the detector and E is the applied electric field strength. The migration time is function of capillary length l_D, applied voltage V_{app} and the "drag tag size" α which define the state variables $\mathbf{z} = [l_D, V_{app}, \alpha]^T$ for this specific problem and the free-solution mobility μ_0 is taken to be a constant parameter, $\mu_0 = 2.4 \times 10^{-4}$ cm^2/V·s, [69] for some implicit temperature,

salt concentration and salt type [70] not defined in the model.

Modeling the migration time alone does not give a complete description of the separation process; we must also define a model for the variance generated during the separation. The physics behind many velocity disturbances are modeled as random walks that are statistically independent from each other [71–73]. As independent random walks, the variance generated from each disturbance can be summed to yield the total variance $\sigma^2 = \sum \sigma^2_{\text{source}}$. These variance sources are most naturally modeled as disturbances observed in space, so that we denote the variance as σ_x^2. For ELFSE using capillary electrophoresis, the significant sources of variance are diffusion, wall adsorption, and Joule heating resulting in the total spatial variance [38–40]

$$\sigma_x^2 = \sigma_{diff}^2 + \sigma_{wall}^2 + \sigma_{JH}^2 \tag{2.7}$$

injection, drag tag polydispersity and other small effects are neglected. It is important to note that the concentration bands are observed at a fixed position l_D away from injection and propagate in time as they pass the "finish-line" detector. The spatial variance is therefore observed as temporal variance under the transformation

$$\sigma_t^2 = \left(\frac{\partial t}{\partial x}\right)^2 \sigma_x^2 = \frac{\sigma_x^2}{u^2}. \tag{2.8}$$

The variance defined in the optimization problem Eq. (2.4) is, in fact, the total temporal variance for each analyte i, $\sigma_i^2 = \sigma_{t,i}^2$.

Diffusion variance σ_{diff}^2 follows from thermal agitations causing stochastic motion in each DNA molecule of length L and is modeled by

$$\sigma_{diff}^2 = 2Dt \tag{2.9}$$

where D is the diffusion coefficient of the DNA of length L [71] and t is the migration time given by Eq. (2.6). The diffusion coefficients can be typically found in the literature, measured experimentally, or, if the analyte is a polymer, the diffusion coefficient can be estimated from well known scaling relations [67, 74, 75]. The scaling $D = D_1/\sqrt{L+\alpha}$ works well for single-stranded DNA with $D_1 = 4.43 \times 10^{-6}$ cm^2/s [76].

Wall adsorption contributes to the variance as DNA molecules randomly adsorb to the capillary wall, cease migration, and eventually desorb and continue migration. Wall adsorption can typically be quatified as

$$\sigma^2_{wall} = W u l_D \tag{2.10}$$

where W is a capillary specific parameter [72] that is some measure of the equilibrium between adsorption and desorption. The parameter W has been measured experimentally to be 16.7 μs using BigDye(TM) in an ABI 310. Although the W parameter will vary with capillary treatment and dye terminator, we will assume it is consistent for the different capillary configurations we consider in this chapter.

Joule heating occurs when the applied electric field warms the capillary buffer. This effect causes a parabolic temperature profile between the capillary core, where the temperature is maximum, and the capillary wall which typically interfaces with coolant. The temperature causes a viscosity gradient which ultimately results in a parabolic velocity profile for the DNA which results in variance generation referred to as Taylor-Aris dispersion [77–82]

$$\sigma^2_{JH} = \frac{J \mu E^5 l_D}{D} \tag{2.11}$$

where J is salt specific parameter which scales as $J \sim d_c^6$ with capillary inner

diameter d_c. For a standard salt buffer of 1x TBE in a 50 μm inner diameter capillary, the parameter J was measured to be 2.72×10^{-12} cm^2/kV^4.

Equipped with the models for migration time and variance generation for each DNA length we can formulate the optimization problem to find the drag tag size α, the capillary length to the detector l_D, and the applied voltage V_{app} that yield the minimum run time for resolving DNA from lengths $L_0 = 26$ bases to the length of read L which is varied from $30, 40, \ldots, 600$ to show the trade offs between read frame size and run time. The optimization problem

Eq. (2.4) can now be restated as

$$
\begin{aligned}
\min \quad & t_{run} = \frac{l_D}{\mu_0 E}\left(1 + \frac{\alpha}{L_0}\right) \\
\text{s.t.} \quad & R_L \leq 1.5 \\
& R_L = \frac{2\sqrt{2\ln(2)\sigma_t^2}}{|\partial t/\partial L|} \\
& \left|\frac{\partial t}{\partial L}\right| = \frac{l_D}{\mu_0 E}\frac{\alpha}{L^2} \\
& E = V_{app}/l_C \\
& l_C = l_D + \delta l \\
& \sigma_t^2 = \frac{\sigma_x^2}{(\mu E)^2} \\
& \sigma_x^2 = \sigma_{diff}^2 + \sigma_{wall}^2 + \sigma_{JH}^2 \\
& \sigma_{diff}^2 = 2Dt \\
& D = \frac{D_1}{\sqrt{L+\alpha}} \\
& \sigma_{wall}^2 = W\mu E l_D \\
& \sigma_{JH}^2 = \frac{J\mu E^5 l_D}{D} \\
& t = \frac{l_D}{\mu E} \\
& \mu = \mu_0\left(\frac{L}{L+\alpha}\right) \\
& 0 \leq \alpha \leq \alpha_{\max} \\
& l_{\min} \leq l_D \leq l_{\max} \\
& 0 \leq V_{app} \leq V_{\max}.
\end{aligned}
\tag{2.12}
$$

The NLP (2.12) is written using a few assumptions and simplifications to the problem Eq. (2.4) developed above. First of all, the run time is known a priori to correspond to the migration time of the shortest DNA length, $t_{run} = t_{L_0}$, since the smallest DNA length, L_0, has the least amount of charge

available to electrophoreses against the drag tag and consequently migrates the slowest. The resolution constraint is also simplified as it can be shown that $R_{L_0} \leq R_{L_0+1} \leq \ldots \leq R_L$. Furthermore the full width at half-maximum w_L is assumed to be equivalent to the full width of the next DNA length $w_L \approx w_{L+1}$ and the difference in migration time is calculated using a derivative $|t_{L+1} - t_L| \approx |\partial t/\partial L|$ which introduces negligible error for large L [39]. Under these simplifications, only two DNA lengths need to be considered in the optimization problem: the length of read L which is the longest DNA length to be resolved during the separation and the shortest DNA length in the separation L_0 which sets the run time. The shortest DNA length in the separation is typically between 18 and 26 bases [39, 40, 69], for this work we use $L_0 = 26$. The DNA physical properties μ_0, D_1, the system property δl and the micelle physical property B' are taken as constant parameters.

The optimization problem Eq. (2.12) can be re-written using some algebraic manipulation to reveal the structure of the optimization problem shown in Eq. (2.13)

$$\begin{aligned}
\min \quad & t_{run} = \frac{p_1 \alpha l_D}{E} + \frac{p_2 l_D}{E} \\
\text{s.t.} \quad & p_3 s_x \left(L + \alpha\right)^2 L^2 \leq l_D^2 \alpha^2 \\
& s_x = s_{diff} + s_{wall} + s_{JH} \\
& s_{diff} E = p_4 l_D \frac{\sqrt{L + \alpha}}{L} \\
& s_{wall} \left(L + \alpha\right) = p_5 L E l_D \\
& s_{JH} \sqrt{L + \alpha} = p_6 L E^5 l_D \\
& V_{app} = \left(l_D + p_7\right) E \\
& 0 \leq \alpha \leq \alpha_{\max} \\
& l_{\min} \leq l_D \leq l_{\max} \\
& 0 \leq V_{app} \leq V_{\max}
\end{aligned} \tag{2.13}$$

where $s_x = \sigma_x^2$ and L is the length of read specified by the user. The parameter groupings p_j are fixed numbers given by $p_1 = \mu_0^{-1} L_0^{-1}$, $p_2 = \mu_0^{-1}$, $p_3 = 2.464$, $p_4 = 2D_1\mu_0^{-1}$, $p_5 = W\mu_0$, $p_6 = J\mu_0/D_1$, and $p_7 = \delta l$ where we use parameter values $\mu_0 = 0.24$ cm^2/kV·s, $D_1 = 4.43 \times 10^{-6}$ cm^2/s, the parameter δl is equipment specific and is typically $\delta l = 10$ cm, and W is taken to be 16.7 μs. The optimization problem Eq. (2.13) is a non-convex NLP problem. Non-convex problems may have multiple local minima. The global optimization code BARON [8] uses spatial branch and bound and symbolic reformulation to efficiently find the global minimum. For this work, we use BARON version 9.0.6 supplied in GAMS version 23.6.2.

Special care must be taken when choosing the units and scaling used for the problem. Large differences in variable values can result in poorly conditioned numerics that lead to an infeasible optimization problem. Also BARON works by making variable substitutions until functional forms that have known convex relaxations can be identified. Reformulating the problem to Eq. (2.13) simplifies the task for BARON which helps accelerate convergence to the global optimum.

2.3 Parallel capillaries

Certain capillary electrophoresis systems, such as the Applied Biosystems Prism 310 Genetic Analyzer and the Applied Biosystems Prism 3130xl, are designed to separate analytes with a capillary array. Capillary arrays are useful for parallel separations under the same applied voltage and capillary length with differing separation mediums (e.g. different sized micelles). Given the original optimization problem Eq. (2.13), it is straightforward to reformulate this problem to allow for a capillary array by copying the constraints for

each capillary. The applied voltage and capillary length is the same for each capillary when a capillary array is used, but the drag tag size α in each capillary can be different. Each capillary must resolve part of the read frame and the optimization problem must therefore include a DNA length L_j which is split between two capillaries with one capillary resolving between the shortest length L_{j-1} and the split length L_j and the other capillary resolves from the split length L_j up to the next split length L_{j+1}. The specified length of read L is defined as L_N, where N is the total number of capillaries used and the specified shortest length of interest is set as L_0.

$$\begin{aligned}
\min \quad & t_{run} = \max_i \{t_i\} \\
\text{s.t.} \quad & t_i = \frac{l_D}{\mu_0 E}\left(1 + \frac{\alpha_i}{L_{i-1}}\right), \quad i = 1, \ldots, N \\
& \left(\text{constraints from NLP (2.13) for capillary } i\right) \\
& L_{j-1} \leq L_j \leq L_{j+1} \qquad j = 1, 2, \ldots, N-1
\end{aligned} \tag{2.14}$$

The objective function $t_{run} = \max\{t_i\}$ is discontinuous and non-differentiable, however the optimization problem is reformulated to an equivalent NLP Eq. (2.15)

$$\begin{aligned}
\min \quad & \eta \\
\text{s.t.} \quad & t_i \leq \eta, \qquad\qquad i = 1, \ldots, N \\
& t_i = \frac{l_D}{\mu_0 E}\left(1 + \frac{\alpha_i}{L_{i-1}}\right) \\
& \left(\text{constraints from NLP (2.13) for capillary } i\right) \\
& L_{j-1} \leq L_j \leq L_{j+1}, \qquad j = 1, 2, \ldots, N-1
\end{aligned} \tag{2.15}$$

which is non-convex and solved to global optimality using BARON. The split

length L_j is treated as a design variable in the optimization problem. The total set of design variables are $\mathbf{z} = [\alpha_1, \cdots, \alpha_N, L_1, \cdots, L_{N-1}, V_{app}, l_D, \eta]^T$ for N parallel capillaries. The length of read L_N and the shortest DNA length of interest L_0 are specified by the user.

2.4 Optimization results and discussion

The optimization problem is set to find the conditions that resolve all the DNA lengths of interest in minimum time. The optimal conditions must therefore carefully balance the trade off between large variance generation and peak spacing. Fig 2.3 shows the variance generated in a single capillary with equipment specifications consistent with an ABI 3130xl ($l_D = 22$ cm, $\delta l = 10$ cm, $V_{\max} = 20$ kV). The variance is shown to decrease for increasing length of read. Small DNA are easy to separate using even a smaller drag tag, therefore resolution can be attained by letting the variance be quite large. This follows physically as small DNA has a much larger diffusion coefficient leading to greater diffusion. The small DNA is separated with a small drag tag which results in greater velocity than the long DNA which requires a larger DNA tag. Variance generated by wall adsorption is shown to decrease with increasing length of read owning to the long DNA large micelle complex having small velocity. Joule heating is negligible for nearly every length of read, contributing to less than 5% to the total variance. Joule heating is very sensitive to electric field, however, and it can be expected to increase steeply if higher electric fields were accessible.

Large drag tags are required to resolve long DNA. The optimal drag tag size can be seen to be increasing with increasing length of read in Fig 2.4(a) and 2.4(b) regardless of the instrument used (The ABI 310 has specifications

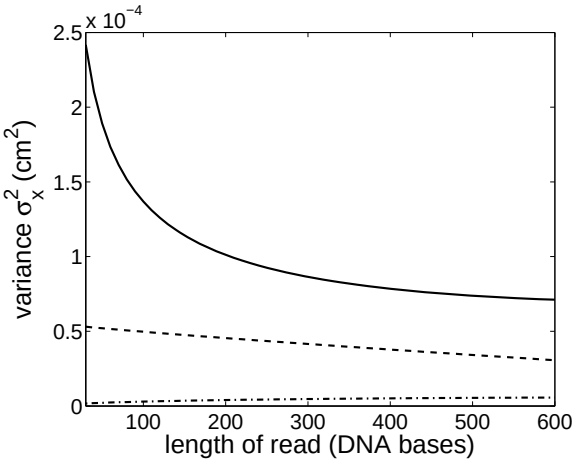

Figure 2.3: Variance sources as a function of length of read in single capillary in an ABI 3130xl. Diffusion (—) is shown to dominate over wall adsorption (– –) and Joule heating (– · –).

l_D = 30.5 cm, δl = 10 cm, $V_{\max}$ = 15 kV). Large drag tags lead to low velocity for the primer (26 bases long) which must pass the detector before the separation is considered complete. Parallel capillaries, therefore, lead to significant reduction in run time as shown in Fig 2.5(a) and 2.5(b) as the optimal drag tag can be selected to separate different groupings of the DNA lengths of interest.

Fig 2.6 shows that benefit derived from using parallel capillaries drops of steeply with increasing capillary number. There is not much benefit in going beyond three parallel capillaries.

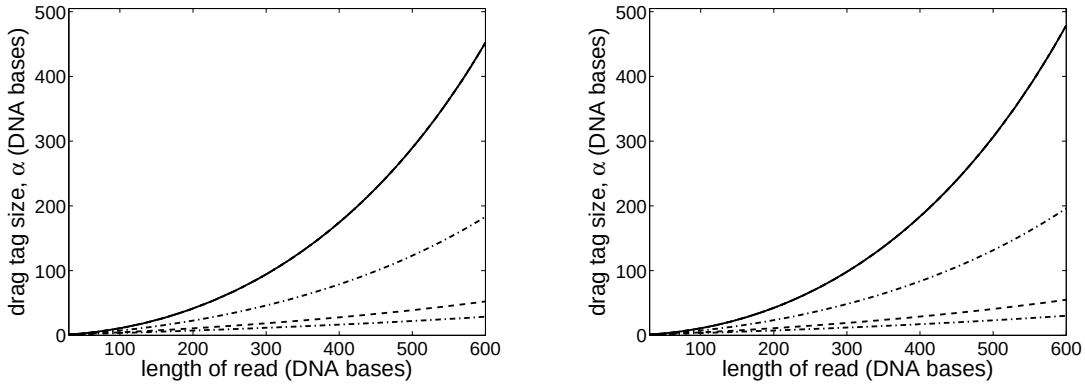

(a) (b)

Figure 2.4: Optimal drag tag sizes as a function of length of read in an ABI 310 (left) and in an ABI 3130xl (right) for (—) single capillary, (– –) double capillaries, and (– · –) triple capillaries. The optimal drag tag size is shown for each capillary. The optimal drag tag size for the first capillary in a parallel array overlaps with that of a single capillary.

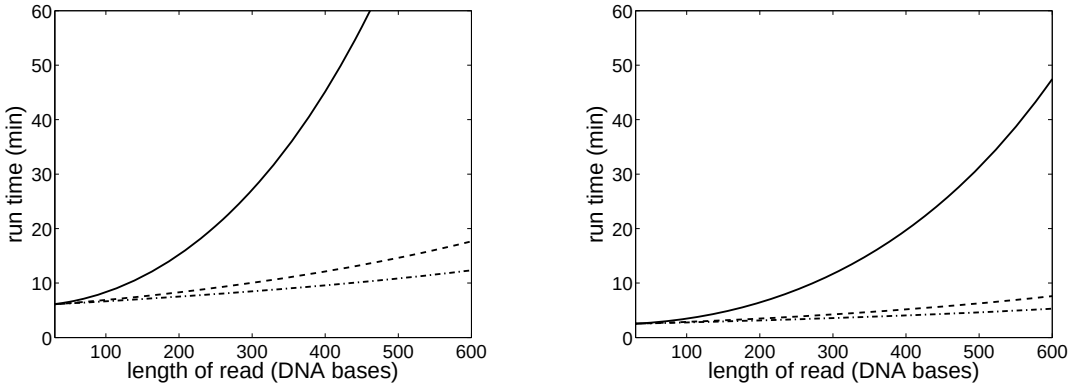

(a) (b)

Figure 2.5: Minimum run time as a function of length of read in an ABI 310 (left) and in an ABI 3130xl (right) for (—) single capillary, (– –) double capillaries, and (– · –) triple capillaries.

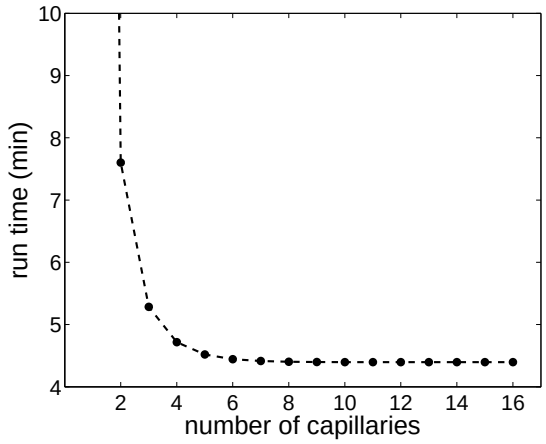

Figure 2.6: Optimal run time for a length of read of 600 bases shown as function of the number of capillaries in a parallel array. The ABI 3130xl offers a maximum of 16 capillaries.

2.5 Summary

In this chapter we showed the optimization of micelle end-labeled free solution electrophoresis in single and parallel capillaries. Parallel capillaries are shown to reduce the run time of the DNA separation by as much as 91%, with 89% reduction in run time realized with just three parallel capillaries. Diffusion is shown to be the greatest contribution to the variance and the total variance is shown to decrease for increasing length of read. The fastest run conditions are generally found by using the maximum voltage and shortest capillary length available.

Nomenclature

D	diffusivity
D_1	scaling coefficient for DNA diffusivity
d_c	capillary inner diameter
E	applied electric field strength

J	Joule heating coefficient
L	DNA length in number of bases
L_0	shortest DNA length of interest
l_C	total capillary length
l_D	capillary length to detector
$\mathbf{g}$	constraints on capillary electrophoresis system
h_i	model for elution time of DNA
p_j	fixed parameters in optimization
R_i	resolution between DNA length i and $i+1$
s_i	model for variance generation of DNA length i
t_i	elution time of DNA length i
u	electrophoretic velocity
V_{app}	applied voltage
W	wall adsorption coefficient
w_i	full width at half-maximum of DNA length i
$\mathbf{z}$	design variables for capillary electrophoresis system
α	size of the drag tag in units of DNA bases
δl	difference between l_C and l_D
μ	electrophoretic mobility
μ_0	free solution electrophoretic mobility
σ^2_{diff}	diffusion variance
σ^2_{JH}	Joule heating variance
σ^2_{wall}	wall adsorption variance
σ^2_i	variance of DNA length i

σ_t^2	total temporal variance
σ_x^2	total spatial variance

Chapter 3

Micelle End-labeled DNA Separation using Alternate Detection Modes

In conventional micelle end-labeled free solution electrophoresis, electro-osmotic flow is suppressed and a finish-line detector is used to observe long DNA migrate first with short DNA to eventually follow. This detection mode is considered conventional as it is readily available through the use of commercial capillary electrophoresis devices. The conventional detection mode is ideal for gel electrophoresis which is the current standard method for DNA separation. This detection mode is not necessarily ideal, however, for end-labeled free solution electrophoresis.

In end-labeled free solution electrophoresis long DNA migrates the fastest and is also the most difficult to resolve. Once the long DNA is resolved, every other DNA length in the capillary is also resolved, but the separation is not complete until the short DNA passes the detector. The short DNA moves very slowly when it has a micelle attached. For end-labeled free solution

electrophoresis it is thus advantageous to detect all the DNA lengths of interest as soon as the length of read becomes resolved.

In this chapter we will see two practical methods for imaging the long DNA as soon as it becomes resolved. The first method makes use of a partially suppressed electro-osmotic flow (EOF) to reverse the elution order of the DNA lengths. The second method discussed in this chapter uses snap-shot detection in a microfluidic device to detect all the DNA lengths of interest the instant they become resolved.

3.1 Controlled EOF counter-flow

McCormick and Slater [76] presented a theoretical study on how to use an electro-osmotic flow (EOF) to reverse the elution order of the separation. Long DNA, bearing more charge than short DNA, can better fight an EOF counter-flow and will stay in the capillary longer giving it more time to separate. Short DNA, which is easily separated, elutes out of the capillary quickly. Unfortunately using an EOF counter-flow opens the possibility of having DNA either eluting too quickly (under separated) or not eluting at all when EOF balances with electrophoresis. McCormick and Slater showed that a range of EOF counter-flows will significantly extend the read frame of ELFSE separations. This read frame extension comes at the expense of run time, however which requires some consideration to examine the tradeoff.

The negative charge laden glass capillary wall is balanced by positive counter-ions within the double layer while the bulk is electro-neutral. When an electric field is applied the positive counter-ions will slip toward the cathode pulling the bulk fluid in an electro-osmotic flow. DNA is negatively charged and will undergo electrophoresis in the opposite direction. The net electroki-

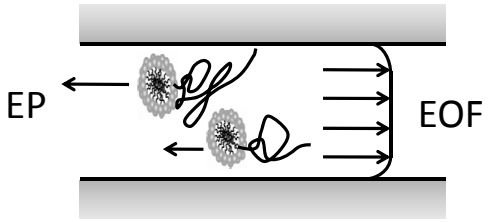

Figure 3.1: Diagram of an EOF active micelle ELFSE separation. EP labels electrophoresis and EOF labels electro-osmotic flow.

netic mobility of the drag-tag DNA complex is

$$\mu = \mu_{EOF} - \mu_0 \left(\frac{L}{L+\alpha} \right) \tag{3.1}$$

where μ_{EOF} is the electro-osmotic mobility, μ_0 is the free solution electrophoretic mobility of DNA, L is the number of DNA bases, and α is the size of drag tag. The elution time is then calculated by $t = l_D/\mu E$ or

$$t = \frac{l_D}{E} \left(\frac{L+\alpha}{\mu_{EOF}\,(L+\alpha) - \mu_0 L} \right) \tag{3.2}$$

where l_D is the capillary length to the detector, E is the applied electric field strength, and μ_{EOF} is the EOF mobility. If EOF mobility is greater than the free solution electrophoretic mobility of DNA ($\mu_{EOF} > \mu_0$) then EOF dominates and DNA will elute from shortest to longest as short DNA bears little charge to fight against EOF and is pushed out of the capillary first. This is commonly the situation when working with bare-silica capillaries which have typical EOF mobilities of $\mu_{bare} = 3.6 \times 10^{-4}$ cm^2/V·s compared to a typical free solution DNA mobility of $2.4{\times}10^{-4}$ cm^2/V·s. Unfortunately bare-silica capillaries impose such a large EOF that the DNA is poorly separated when it elutes passed the detector. The separation of DNA lengths in CE is given

by the temporal spacing

$$\left|\frac{\partial t}{\partial L}\right| = \frac{l_D}{E}\frac{\alpha\mu_0}{\left(\mu_{EOF}(L+\alpha)-\mu_0 L\right)^2} \tag{3.3}$$

which is a strong function of the drag tag size and EOF. The proper choice of EOF mobility and drag tag size will yield infinite separation for DNA length L but the elution time will also go to infinity as this particular DNA length has zero net mobility. Using EOF, the temporal spacing can be optimized to suit the separation of long DNA. The increased DNA separation comes at the expense of long (possibly infinite) elution times, however and the tradeoff must be considered carefully.

Temporal spacing alone is not sufficient to quantify the quality of the separation. In CE, DNA is injected into the capillary as a square plug which, over the course of the separation, evolves to a Gaussian profile due to diffusion and other velocity perturbing effects such as wall adsorption and drag tag polydispersity. If the Gaussians are broad compared to the spacing then the profiles will be poorly resolved as indicated by the resolution factor, R_L

$$R_L = \frac{\sqrt{8\ln(2)\sigma_t^2}}{|\partial t/\partial L|} \tag{3.4}$$

where σ_t^2 is the variance of the Gaussian profile so that the resolution factor is the ratio of the full-width at half maximum of the Gaussian to the temporal spacing. If $R_L \leq 1.5$ then the separation method produces single base resolution. The temporal variance is related to the spatial variance through the velocity

$$\sigma_t^2 = \frac{\sigma_x^2}{(\mu E)^2} \tag{3.5}$$

where μ is given by Eq. (3.1). As seen in chapter 2 significant contributions to

the variance are given by diffusion, wall adsorption, and Joule heating [38, 39]

$$\sigma_x^2 = 2Dt + W\mu E l_D + \frac{J\mu E^5 l_D}{D} \tag{3.6}$$

where D is the DNA diffusivity, which scales with DNA length according to $D = D_1/\sqrt{L+\alpha}$, with $D_1 = 4.43 \times 10^{-6}$ cm^2/s, W is the wall adsorption parameter with $W = 16.7$ μs, and J is the Joule heating parameter with $J = 2.72 \times 10^{-12}$ cm^2/kV^4.

Now that we have defined the variance generation and the peak spacing above, we can identify the optimal EOF mobility, drag tag size, capillary

length, and electric field strength by solving the NLP

$$
\begin{aligned}
\min \quad & t_{run} = \frac{l_D}{\mu_0 E}\left(1+\frac{\alpha}{L}\right) \\
\text{s.t.} \quad & R_L \leq 1.5 \\
& R_L = \frac{2\sqrt{2\ln(2)\sigma_t^2}}{|\partial t/\partial L|} \\
& \left|\frac{\partial t}{\partial L}\right| = \frac{l_D}{E}\frac{\alpha\mu_0}{\left(\mu_{EOF}(L+\alpha)-\mu_0 L\right)^2} \\
& E = V_{app}/l_C \\
& l_C = l_D + \delta l \\
& \sigma_t^2 = \frac{\sigma_x^2}{(\mu E)^2} \\
& \sigma_x^2 = 2Dt + W\mu E l_D + \frac{J\mu E^5 l_D}{D} \\
& D = \frac{D_1}{\sqrt{L+\alpha}} \\
& t = \frac{l_D}{\mu E} \\
& \mu = \mu_{EOF} - \mu_0\left(\frac{L}{L+\alpha}\right) \\
& \mu \geq 0 \\
& 0 \leq \mu_{EOF} \leq \mu_{bare} \\
& 0 \leq \alpha \leq \alpha_{\max} \\
& l_{\min} \leq l_D \leq l_{\max} \\
& 0 \leq V_{app} \leq V_{\max}
\end{aligned}
\tag{3.7}
$$

This optimization problem is similar to the one presented in Eq. (2.12). One key differences is that the run time is set by the length of read as the constraint $\mu \geq 0$ ensures EOF dominates the flow throughout the design space which leads to a reversal of the elution order of the DNA. The optimization problem can also be reformulated for the electrophoresis dominant case

by replacing $\mu \rightarrow -\mu$ and $E \rightarrow -E$ indicating that the net mobility now causes DNA to move in the opposite direction but still heads to the detector as the polarity of the electric field is flipped. Optimization shows that the electrophoresis dominant case should be run completely EOF suppressed and is therefore identical to the conventional method discussed above.

In the results section, we will see that partially suppressed EOF active capillaries can be used to significantly speed up the DNA separation. Partial suppression of EOF can be difficult to control, however. We will also see that the optimal EOF mobility strongly depends on the free solution electrophoretic mobility of DNA μ_0 which may vary between experiments. We take the bare-silica EOF mobility to be $\mu_{bare} = 3.6 \times 10^{-4}$ cm^2/V·s.

3.2 EOF-ELFSE Optimization results

The minimum run times of the partially suppressed EOF active ELFSE DNA separation is shown in fig 3.2. The optimization shows that a single partially EOF suppressed capillary in an ABI 3130xl can separate 600 bases in 4.35 minutes, which is two seconds faster than using 16 parallel capillaries in the EOF suppressed case reported in fig 2.6. Fig 3.3 shows the optimal EOF mobility and the optimal run time for a length of read of 600 bases is a strong function of the free solution electrophoretic mobility of DNA.

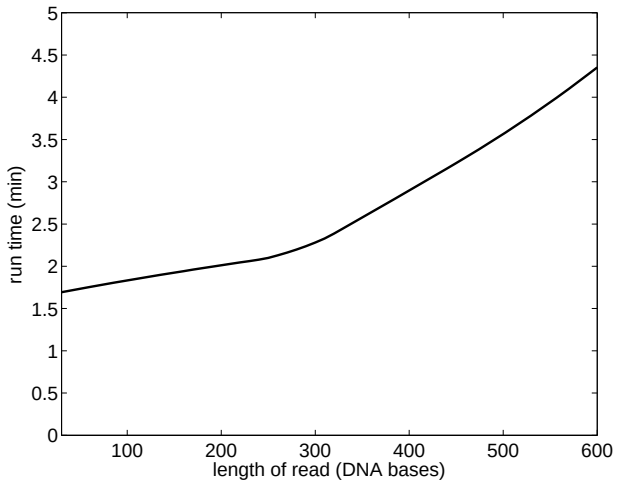

Figure 3.2: Optimal run time for partially EOF suppressed capillaries (—)

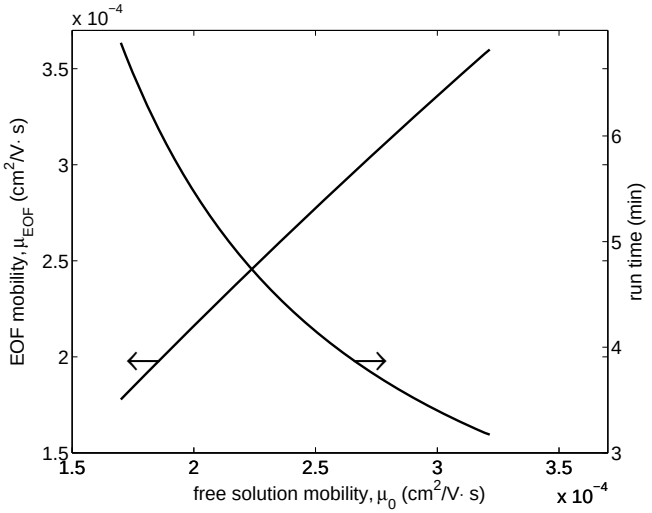

Figure 3.3: Sensitivity of optimal EOF mobility and optimal run time to free solution mobility for 600 bases of length of read. The typical value is $\mu_0 = 2.4 \times 10^{-4}$ cm^2/V$\cdot$ s. The arrows point each curve to their y-axis.

3.3 Snap-shot detection

In this section, we will discuss the modeling and optimization framework for using snap-shot detection mode in micelle end-labeled free solution electrophoresis DNA separations. Snap-shot detection is the instantaneous imaging of the entire separation channel. Snap-shot detection is capable of imaging the entire DNA separation the moment the length of read is resolved. Snap-shot detection is not without its own challenges however. Instantaneous imaging of an entire separation channel (typically between 5 and 20 cm) can be performed using a microfluidic device on a motorized stage. Microfluidic devices are typically between 3 cm $\times$ 3 cm up to 10 cm $\times$ 10 cm. Turns are often required in order to fit a sufficiently long channels on to the microfluidic device. Figure 3.4 shows the serpentine and spiral configurations which are commonly used to fit long separation channels on a small chip area. Pfeiffer et al. [83] showed that a non-linear programming problem can be posed to find the smallest microfluidic device to complete a generic separation using electrophoresis. In this section we show how to formulate an optimization problem that is used to design a microfluidic device for minimum run time DNA separations using micelle ELFSE under the snap-shot detection mode.

When using snap-shot detection, there is no benefit in reversing the elution order of the DNA by using an EOF counter flow. DNA will migrate the fastest with EOF full suppressed. Hence, the electrophoretic mobility, μ, of the micelle-DNA complex is

$$\mu = \mu_0 \frac{L}{L + \alpha} \tag{3.8}$$

where μ_0 is the free-solution mobility of DNA, L is the length of DNA in bases, and α is the size of the micelle in units of uncharged DNA bases that

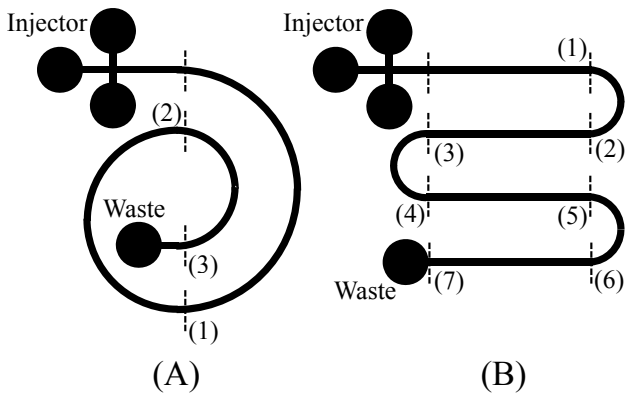

Figure 3.4: (A) Microfluidic spiral, (B) microfluidic serpentine. The different configurations are composed of either straight sections or semi-circular turn sections which are indicated by dashed line.

have the equivalent drag of the micelle. With snap-shot detection the DNA molecules are observed as they migrate down the separation channel. As the DNA molecules migrate down the separation channel, they separate into different concentration profiles that are Gaussian in shape, when averaged across the cross-section of the separation channel, as shown in Figure 3.5. The con-

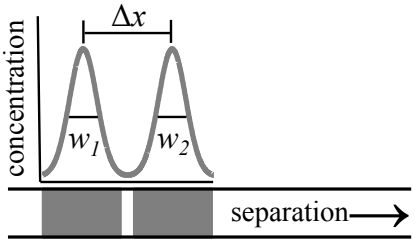

Figure 3.5: Band broadening in snap-shot detection.

centration profiles are resolved from each other when the average full-width at half-maximum, w_L, is less than 1.5 times the spacing between maximums, Δx_L,

$$R_L = \frac{w_L + w_{L+1}}{2\Delta x_L} \leq 1.5 \tag{3.9}$$

where R_L is the resolution factor. The spacing between Gaussians is given by

$$\Delta x_L \approx \frac{\partial x}{\partial L} = \mu_0 E t \frac{\alpha}{(L+\alpha)^2} \tag{3.10}$$

where t is the time at which the Gaussians are detected. With snap-shot detection, the full-width at half-maximum is a measure of the Gaussians width as it evolves in space

$$w_L = 2\sqrt{2\ln(2)\sigma_x^2} \tag{3.11}$$

where σ_x^2 is the spatial variance for DNA of length L.

The convection-diffusion equation can be used to model the effect of the microfluidic device topology on the concentration profiles as the DNA lengths migrate through the microfluidic device

$$\frac{\partial c_L}{\partial t} + \mathbf{u}\cdot\nabla c_L = D\nabla^2 c_L \tag{3.12}$$

where c_L is the concentration profile of DNA of length L, D is the diffusivity, and $\mathbf{u}$ is the electrophoretic velocity vector. The convection-diffusion equation (3.12) can be solved analytically, using a few simplifying assumptions, to reveal the model for the variance generation σ_x^2 as the concentration profile propagates down the microfluidic channel [84–86].

The primary simplification to the convection diffusion equation (3.12) deals with the velocity of the DNA in a curved microfluidic channel. In a straight channel, the velocity is constant. In a microfluidic turns, the DNA velocity varies across the interior of the channel. This is because the outside channel has a longer contour length than the inside channel which also results in an electric field gradient. Defining the x coordinate to be along the axial direction of the microfluidic channel and the y coordinate to be pointing to the interior of the microfluidic channel (see figure 3.6), the velocity is given by $\mathbf{u} = u(y)\mathbf{e}_x$ where $\mathbf{e}_x$ is the unit vector pointing in the axial direction [84–86].

The convection-diffusion equation (3.12) is two-dimensional in (x, y) and is solved analytically to determine σ_x^2 as a function of the microfluidic structure

[85, 86],

$$\sigma_x^2 = \sigma_0^2 + 2Dt + \sum_{i \in I} \sigma_{skew,i}^2 + \sum_{j \in J} \sigma_{turn,j}^2 + \sigma_{other}^2 \tag{3.13}$$

where σ_0^2 is the initial variance of the injected Gaussian profile, $2Dt$ is the variance caused by diffusion over the migration time t, DNA diffusivity scales as $D = D_1/\sqrt{L + \alpha}$ where D_1 is constant [76], $\sigma_{skew,i}^2$ is the variance caused by a skewed concentration profile as it enters section i, I is the set of all sections in the microfluidic device, $\sigma_{turn,j}^2$ is the variance caused by the concentration profile migrating through each turn, J is the set of all turn sections in the microfluidic device, and σ_{other}^2 is any other source of variance not modeled by the convection-diffusion equation. Here a section is defined as either a straight channel or a semi-circular turn. A spiral consists only of semi-circular turn sections while a serpentine

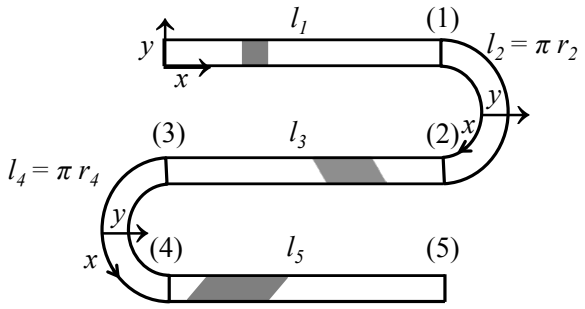

Figure 3.6: Concentration profiles are broadened by turns. The variance of the concentration profile is increased during each turn and quantified by $\sigma_{turn,j}^2$. The initial concentration profile is unskewed. After the first turn the concentration profile becomes skewed and diffusion is enhanced by the concentration gradient which results in variance generation $\sigma_{skew,3}^2$. The second turn is complementary which subtracts some variance $\sigma_{skew,4}^2$. The index of each section i is specified at the section exit.

Figure 3.6 shows the variance generated by turns in a microfluidic device. After a turn, the concentration band becomes skewed. The skewed concentration band causes the variance to increase as the concentration gradient cause diffusion to be exacerbated. The variance increase due to concentration profile

skew is

$$\sigma^2_{skew,i} = \sum_{n=1,3,5,\ldots}^{\infty} S_n^{(i)} \Gamma_n^{(i)} \tag{3.14}$$

where $\Gamma_n^{(i)} = \pm \frac{8\mu E w_c^2}{r_i D (n\pi)^4} \left(1 - e^{-(n\pi)^2 D t_i / w_c^2}\right)$, μ is the mobility given by Eq. (3.8), E is the applied electric field, w_c is the channel width, r_i is the radius of the center-line of the turn, D is the diffusivity, t_i is the time it takes to get through the turn or straight section i, i.e. $t_i = l_i / (\mu E)$ where l_i is length of the turn or straight channel. The term $S_n^{(i)}$ indicates the concentration band skewness as it enters section i.

$$S_n^{(i)} = \begin{cases} S_n^{(i-1)} e^{-(n\pi)^2 D t_i / w_c^2}, & (i-1) \in K \\ S_n^{(i-1)} e^{-(n\pi)^2 D t_i / w_c^2} + \Gamma_n^{(i-1)}, & (i-1) \in J \end{cases} \tag{3.15}$$

where K is the set of straight sections, J is the set of turn sections, and the initial concentration profile is assumed to be unskewed, $S_n^{(1)} = 0$. The sign on the terms $\sigma^2_{skew,i}$ and $\Gamma_n^{(i)}$ is indicated by the orientation of the turns with respect to the y-axis. If the center of the turn is pointing away from the positive y-direction then the sign on $\sigma^2_{skew,i}$ and $\Gamma_n^{(i)}$ is positive, if the center of the turn is pointing toward the positive y-direction then the sign on $\sigma^2_{skew,i}$ and $\Gamma_n^{(i)}$ is negative. In figure 3.6 the sign of $\sigma^2_{skew,i}$ and $\Gamma_n^{(i)}$ on the right turn is positive and the sign on the left turn is negative. The sign changes with each successive turn which indicates how the complementary turns can be used in a serpentine to mitigate against large variance development. The sign on $\sigma^2_{skew,i}$ and $\Gamma_n^{(i)}$ is always positive for a straight channel (after a turn) and a spiral. The spiral configuration does not allow for complementary turns and instead uses large turn radii to mitigate against large variance development. As the turn radius tends to large values, the turn can be well approximated as a straight channel as variance generation due to the race track effect becomes

negligible.

Turns in microfluidic devices introduce variance into the concentration profile due to the non-uniform velocity across the width of the channel. This variance generation is quantified by

$$\sigma_{turn,j}^2 = \left(\frac{8\mu E w_c^3}{r_j D}\right)^2 \sum_{n=1,3,5,\ldots}^{\infty} \frac{\Phi_n(t_j)}{(n\pi)^8} \tag{3.16}$$

where $\Phi_n(t_j) = -1 + e^{-(n\pi)^2 D t_j / w_c^2} + (n\pi)^2 D t_j / w_c^2$.

The term σ_{other}^2 in Eq. (3.13) refers to any other sources of variance not modeled by the convection-diffusion equation (3.12). As presented above, the other significant sources of variance are wall adsorption and Joule heating rendering the complete variance

$$\sigma_x^2 = \sigma_0^2 + 2Dt + \sum_{i\in I} \sigma_{skew,i}^2 + \sum_{j\in J} \sigma_{turn,j}^2 + W\mu E l_D + \frac{J\mu E^5 l_D}{D}. \tag{3.17}$$

The run time for micelle ELFSE in a microfluidic device is set by the instant the longest DNA length of interest (the length of read) is resolved. At that instant, the entire microfluidic device is scanned by the snap-shot detection and every DNA length is detected. The minimum snap-shot run time can be

found by solving the following non-convex optimization problem

$$
\begin{aligned}
\min \quad & t_{run} = \frac{l_D}{\mu_0 E}\left(1+\frac{\alpha}{L}\right) \\
\text{s.t.} \quad & \text{Eq. (3.8) – Eq. (3.11)}, \\
& \text{Eq. (3.14) – Eq. (3.17)} \\
& D = D_1/\sqrt{L+\alpha} \\
& E = V_{app}/l_D \\
& l_D = \sum_{i\in I} l_i \\
& 0 \le \alpha \le \alpha_{\max} \\
& 0 \le V_{app} \le V_{\max} \\
& g(l_i, r_j) \le X_{\max} \\
& h(r_j) \le Y_{\max} \\
& c(l_i, r_j) \le 0
\end{aligned}
\tag{3.18}
$$

where L is the length of read. The constraints g, h, and c are geometric constraints that ensures that the microfluidic device fits the specified area and ensures that all the sections are contiguous, $g(l_i, r_j) = h(r_j) = 2r_j$, $\forall j \in J$ for a spiral or $g(l_i, r_i) = l_i + r_{i+1} + r_{i-1}$, $\forall i \in I$ and $h(r_j) = \sum_{j\in J} 2r_j$ for a serpentine, X_{max} and Y_{max} is the maximum length allowed for the horizontal and vertical side of the microfluidic device, respectively. A serpentine is assumed to have straight channels aligned in the horizontal direction. In addition, spirals have the constraint $c(l_i, r_j) = \delta r - (r_{j-1} - r_j)$, $\forall j \in J$, which prevents the turns from overlapping. For serpentines the constraint $c(l_i, r_j) = l_i - l_{i-1}$, $\forall i \in I$ guarantees connectivity between the turns and each straight channel.

The parameters are specified to match DNA in a micelle solution, i.e. $\mu_0 = 2.4 \times 10^{-4}$ cm^2/V·s, $D_1 = 4.43 \times 10^{-6}$ cm^2/s, $\alpha_{\max} = 502$ and $W = 16.7\,\mu$s.

The maximum dimensions of the device are set at $X_{\max} = Y_{\max} = 10$ cm. The minimum gap between turns in a spiral δr is set at 0.1 cm, which allows for practical fabrication of the device [87]. The maximum applied voltage is $V_{\max} = 20$ kV.

3.4 Snap-shot detection optimization results and discussion

The minimum run times of the snap-shot detection modes are shown in fig 3.7. For convenience we also show the results from chapter 2 for single and parallel capillaries in an ABI 3130xl, and the EOF-ELFSE results from the previous section.

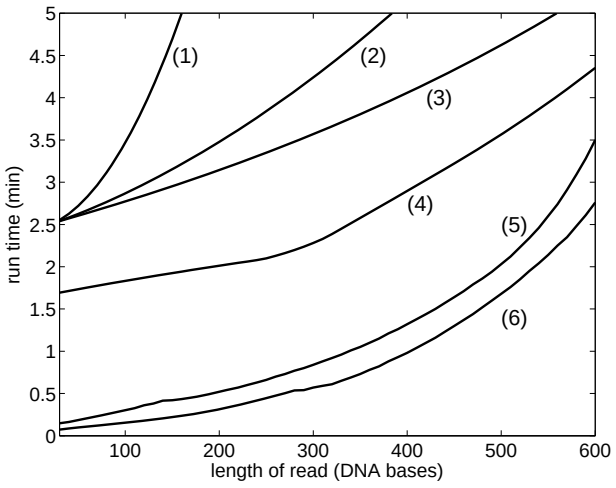

Figure 3.7: Optimal run time for (1) single capillary, (2) two parallel capillaries, (3) three parallel capillaries, (4) partially suppressed EOF counter-flow, (5) spiral microfluidic device, and (6) serpentine microfluidic.

From the optimization results, it is clear that snap-shot detection implemented using microfluidics offers significant speed up over partially EOF suppressed capillaries and parallel capillaries operating in the conventional detection mode. The optimal microfluidic structure for a length of read of 600

bases is the serpentine composed of five sections (or two turns). Fig 3.8 shows the minimum run time for achieving a length of read of 600 bases in both a serpentine and a spiral. For serpentines the run time decreases as the number of sections increases although the total channel length is identical for serpentines with more than five sections. This requires tighter turn radii which can be mitigated by design of the complementary turns. For spirals the run time increases with increasing number of sections. The design constraints are such that the spiral must increase the channel length every time an additional turn is used even though the increased channel length comes at the expense of run time.

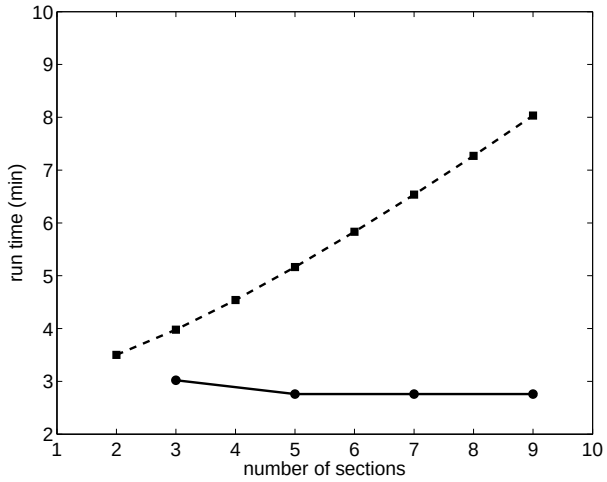

Figure 3.8: Optimal run time for a length of read of 600 bases as a function of the number of sections in a microfluidic serpentine (—●—) and a microfluidic spiral (−−■−−).

3.5 Summary

In this chapter we showed that alternate detection modes, such as a controlled EOF counter-flow and snap-shot detection can be used to significantly reduce the run time for micelle end-labeled free solution electrophoresis DNA separations. Microfluidic serpentines are shown to be the optimal configuration for micelle ELFSE which can separate 600 bases in 2.76 min using five sections. Spirals can be used to resolve a length of read of 600 bases in 3.50 min using two turn section. The partially EOF suppressed capillary is the slowest of the these alternate modes, resolving 600 bases in 4.35 min in an ABI 3130xl.

Nomenclature

c	geometry constraint for microfluidic device
c_L	concentration profile of DNA length L
D	diffusivity
D_1	scaling coefficient for DNA diffusivity
E	applied electric field strength
g	geometry constraint for microfluidic device
h	geometry constraint for microfluidic device
J	Joule heating coefficient
L	DNA length in number of bases
L_0	shortest DNA length of interest
l_C	total capillary or channel length
l_D	capillary or channel length to detector
l_i	channel length of mircofluidic section i

R_L	resolution between DNA length L and $L+1$
r_j	turn radius in microfluidic turn j
$S_n^{(i)}$	skew coefficient in microfluidic section i
t	elution time of DNA length L
u	electrophoretic velocity
V_{app}	applied voltage
W	wall adsorption coefficient
w_L	full-width at half-maximum of Gaussian signal for DNA length L
w_c	channel width in microfluidic device
α	size of the drag tag in units of DNA bases
$\Gamma_n^{(i)}$	skew generated between microfluidic section i and $i+1$
Δx_L	spacing between Gaussians
δl	difference between l_C and l_D
μ	net electrokinetic mobility
μ_0	free solution electrophoretic mobility
μ_{bare}	electro-osmotic mobility of a bare-silica capillary
μ_{EOF}	electro-osmotic mobility
Φ_n	turn variance factor
σ^2_{other}	variance not modeled by convection-diffusion equation
$\sigma^2_{skew,i}$	skew variance for microfluidic section i
σ_t^2	total temporal variance
$\sigma^2_{turn,j}$	turn variance for turn j
σ_x^2	total spatial variance

Chapter 4

Micelle End-labeled DNA Separation using Entropic Trapping

In the previous chapters we have discussed micelle end-labeled free solution electrophoresis (ELFSE) as a method for rapid DNA separation. The read frames previously reported ranged from 30 to 600 bases, which is well within the range to be useful for short-tandem repeat analysis, a common forensic analysis [31, 32]. However, separation of long DNA (above 5000 bases) is important for many other DNA analysis techniques including DNA fingerprinting and miRNA detection. Separation of long DNA using micelle ELFSE is difficult without the use of extremely large micelle drag tags. Unfortunately large micelles introduce additional complications such as causing DNA sieving [88].

Pulse Field Gel Electrophoresis (PFGE) was the first techniques to push DNA separation into the long DNA regime [89]. Long DNA migrates through gel in a length intensive process called biased reptation [41]. Before DNA can undergo steady-state biased reptation it must first orient itself along the elec-

tric field direction. Switching field direction compels the DNA to reorient itself yielding a length dependent delay time before steady state biased reputation can be re-established. The process continues for around 12 to 24 hours to separate DNA up to the 700 kilobasepair (kbp) range [89]. Optimization of the field strengths and oscillation frequency can speed-up the separation mode to reported separations of DNA lengths 0.1 to 10.0 kbp in 30 minutes [90], 0.125 to 23.1 kbp in 9 minutes [91], 8.3 to 48.5 kbp in 45 minutes [45], and 48.5 kbp to 1 Mbp in 3 hours [45].

At the dawn of the 21st century, innovations in microfabrication techniques created the possibility for rapid separation of long DNA. Microfabricated post arrays, for instance, can separate λ-DNA and T4 DNA, 48.5 kbp and 166 kbp respectively, in under 30 seconds [57]. The difference in length between λ-DNA and T4 DNA is substantial. For smaller gaps in DNA length post arrays are not quite as fast, for instance post arrays separate from 2.3 kbp to 23 kbp with 2 kbp resolution in 11.4 minutes [57]. A comparable technique for rapid separation of long DNA in a microfabricated obstacle course is entropic trapping which can separate from 5 kbp to 30 kbp with 5 kbp resolution in 15 minutes [49].

An interesting feature of entropic trapping is that long DNA elutes first through the separation channel. Scaling analysis [49, 92, 93], Monte Carlo simulations [94, 95] and Brownian dynamics simulations [96–98] were employed to show that the primary mechanism behind long DNA eluting first is that long DNA has a greater probability than short DNA of encountering the high electric field within the slit of the entropic trap. Short DNA will stay within the deep well until Brownian motion causes it to encounter the slit. Each DNA length must overcome an entropic penalty to travel through the slit which is primarily a function of the stiffness of the DNA and the radius of

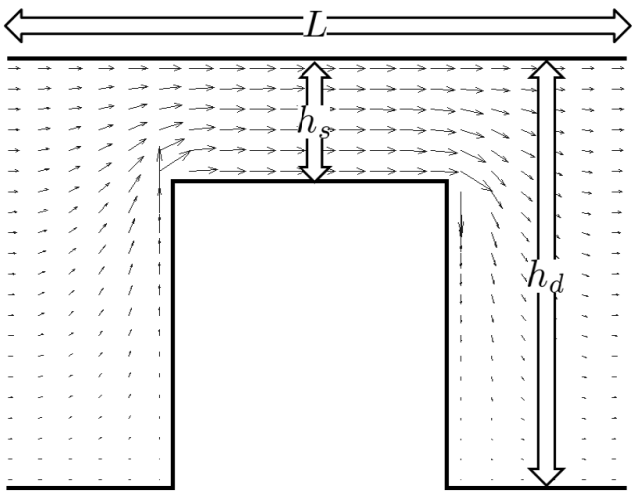

Figure 4.1: Electric field in an entropic trap. The pitch L, the height of the slit h_s, and the height of the deep well h_d are labeled.

gyration of the DNA relative to the height of the slit. Improving the separation performance of entropic trapping is difficult. The primary tuning parameters are the height of the slit, the height of the deep well, and the applied electric field [49].

In this chapter we introduce the use of a drag tag as an additional tuning parameter which may significantly improve separation performance. Without the trap, the DNA will undergo end-labeled free solution electrophoresis which was the focus of previous chapters. With the trap, the DNA will undergo a combination of end labeled electrophoresis and entropic trapping that we will here after refer to as end-labeled entropic trapping electrophoresis (ELETE). We employ Brownian dynamics simulations to test the performance increase of ELETE over entropic trapping alone. We use Brownian dynamics simulations due to its success at modeling DNA stretching in flow [60, 99, 100], DNA dynamics in a post array [61, 101–103], DNA in confinement [104–109], and DNA in entropic traps and nanopits [54, 96–98].

In the next section we will outline the Brownian dynamics simulations used in this work. In the results section we will see that the drag tag not

only separates DNA in the deep wells but also improves the entropic trapping phenomena itself leading to increased separation performance. We end with some discussion on the physical mechanism for the improved performance.

4.1 Brownian dynamics simulations

Brownian dynamics simulations are course grained stochastic simulations that approximate a polymer by a series of bead-springs (or bead-rods). Newton's second law of motion is enforced at each bead i such that

$$F_i^D + F_i^E + F_i^B + F_i^S + F_i^{EV} = m\frac{d^2 r_i}{dt^2} \approx 0 \tag{4.1}$$

where F_i^D is the drag force on bead i, F_i^E is the electrophoretic force, F_i^B is the Brownian motion force, F_i^S is the spring force between beads, F_i^{EV} is the excluded volume force, m is the mass of bead i, and r_i is the position vector of bead i, i.e. $r_i = [x_i, y_i, z_i]^T$. These course grain simulations are useful at length and time scales that render then left hand side of Eq. (4.1) to be significantly larger than the mass times acceleration [110], it is therefore taken to be zero to reduce the order of the differential equations.

The drag force is modeled as Stoke's flow over a spherical bead such that

$$F_i^D = -\xi_i \frac{dr_i}{dt} \tag{4.2}$$

where ξ_i is the drag coefficient for bead i. The drag coefficient ξ is identical for each bead except for the first bead which is tagged with a drag tag taking on drag coefficient $\xi_1 = \xi\ (1 + \alpha)$. In this work we take the drag coefficient ξ to be constant which neglects hydrodynamic interactions. The diffusion coefficient is known, however, to change significantly during confinement [104, 109, 111].

This phenomena cannot be captured with the proposed simulation.

The bead-spring is driven by an electrophoretic force $F_i^E = \xi_i \mu_i E_i$ with electrophoretic mobility μ_i and electric field at the bead coordinates $E_i = E(r_i)$. The electric field for an entropic trap is found by solving Laplace's equation, $\partial^2\phi/\partial x^2 + \partial^2\phi/\partial y^2 = 0$, over the interior of the entropic trap shown in fig 4.1, with homogeneous Neumann boundary conditions on the walls, and Dirichlet boundary conditions $\phi(0, y) = 1$ and $\phi(1, y) = 0$ using the MATLAB PDE toolbox. The electric field is then calculated as $E = -\nabla\phi$ and converted to units consistent with the simulation.

The Brownian motion of each bead follows from solvent molecules randomly bombarding the bead due to thermal agitations. The random fluctuations are isotropic and dissipated by drag over some infinitesimally small time dt so that

$$\begin{aligned} \mathbb{E}\big[F_i^B(t)\big] &= 0 \\ \mathbb{E}\big[F_i^B(t) F_i^B(t+dt)^T\big] &= 2kT\xi_i\delta(dt)I \end{aligned} \tag{4.3}$$

where $\mathbb{E}$ is the expectation operator, k is the Boltzmann constant, T is the temperature, $\delta(\cdot)$ is the Dirac-delta function, and I is the idem factor [112]. Eq. 4.3 is more conveniently written as

$$F_i^B dt = \sqrt{2kT\xi_i}\, dw_i \tag{4.4}$$

where dw_i is a Wiener process with zero mean and variance dt. Eq. (4.1) therefore renders the stochastic differential equations (SDE) for each bead i

$$dr_i = \left(\mu_i E_i + \frac{1}{\xi_i}\big(F_i^S + F_i^{EV}\big)\right) dt + \sqrt{\frac{2kT}{\xi_i}}\, dw_i. \tag{4.5}$$

It is convenient at this point to non-dimensionalize the SDE with length, time

and force dimensions

$$l_{dim} = l_s, \quad t_{dim} = \frac{\xi l_s^2}{kT}, \quad F_{dim} = \frac{kT}{l_s} \tag{4.6}$$

respectively, where l_s is the length of the spring (the maximum length between beads), ξ is the drag coefficient per bead that does not have a drag tag attached, yielding the dimensionless stochastic differential equations

$$\begin{aligned} d\tilde{r}_1 &= \left(Pe\,\tilde{u}_1 + \tilde{F}_1^S + \tilde{F}_1^{EV}\right)\frac{d\tilde{t}}{1+\alpha} + \sqrt{\frac{2}{1+\alpha}}\,d\tilde{w}_1 \\ d\tilde{r}_i &= \left(Pe\,\tilde{u}_i + \tilde{F}_i^S + \tilde{F}_i^{EV}\right)d\tilde{t} + \sqrt{2}\,d\tilde{w}_i, \quad i = 2 \ldots N_b \end{aligned} \tag{4.7}$$

where $Pe = \mu_0 E_0 l_s \xi / kT$ is the bead Peclet number, E_0 is the applied field strength, $\tilde{u}_i = E_i/E_0$, and tildes denote a dimensionless quantity. The first bead models DNA tagged with a drag tag of size α in units of equivalent number of beads of uncharged DNA. For comparison to experimental data we choose the parameter, $l_s = 206$ nm, which, when compared to the length per basepair of fluorescently stained DNA $l_b = 0.45$ nm, models 5000 basepairs (5 kbp) of DNA using 12 beads. We take the drag coefficient per bead to be $\xi/kT = 5.11\times10^{-2}$ s/μm^2 which is consistent with a diffusion coefficient of $D = kT/\xi N_b = 1.63$ μm^2/s for 5 kbp (untagged) DNA with $N_b = 12$ beads. The free solution mobility of DNA is taken to be $\mu_0 = 2.4 \times 10^{-4}$ cm^2/V·s yielding an effective charge per bead of $\xi\mu_0 = 31.5\,e$ at room temperature ($T = 298$ K) where e is the charge of an electron. The first bead, which models DNA tagged with a drag tag, has an identical effective charge of $\xi(1+\alpha)\mu_0/(1+\alpha)$. The effective charge per bead models the screened charge of DNA which is well below the native charge of at least 600 e per bead. Here after we will present only dimensionless quantities and drop the tildes for the sake of brevity.

The stochastic differential equations Eq. (4.7) models a polymer as a num-

ber of beads connected by springs. The spring force accounts for entropic penalty for deforming the polymer. The spring force is proportional to the stiffness of the polymer which is measured by the persistence length l_p. The Marko Siggia spring force law closely matches force extension curves for double stranded DNA [113, 114]. The spring force law is valid for a segment of DNA composed of at least 20 persistence lengths ($\sim$1 μm, or 3120 bp) [115]. Theoretical improvements by Underhill and Doyle [115] allow the updated spring force law to be valid for a segment of DNA composed of approximately 4 persistence lengths ($\sim$0.2 μm, or 624 bp). The spring force is

$$F_i^S = f_i \frac{r_{i+1} - r_i}{\|r_{i+1} - r_i\|} - f_{i-1} \frac{r_i - r_{i-1}}{\|r_i - r_{i-1}\|} \tag{4.8}$$

where the magnitude of the force caused by stretching bead i from $i+1$ is

$$f_i = \frac{\lambda q_i}{\left(1 - q_i^2\right)^2} - \frac{7 q_i}{1 - q_i^2} + C_s q_i + D_s q_i \left(1 - q_i^2\right) \tag{4.9}$$

where $\lambda = l_s / l_p$, $q_i = \|r_{i+1} - r_i\|$ is the distance between beads and coefficients

$$\begin{aligned} C_s &= 3\lambda/32 - 3/4 - 6/\lambda \\ D_s &= \frac{0.4063\lambda^3 + 0.8172\lambda^2 - 14.79\lambda}{\lambda^2 - 4.225\lambda + 4.87}. \end{aligned} \tag{4.10}$$

In this work we take $l_p = 53.1$ nm, which yields $\lambda = 3.88$. It is important to note that the spring is finitely extensible so that the maximum distance between beads is $q_i = 1$. Furthermore, there is no spring force when the springs are completely compressed and the beads are free to overlap without an additional force term.

The excluded volume force term in Eq. (4.7) prevents the beads from

overlapping and is modeled as the force resulting from a soft Gaussian potential

$$F_i^{EV} = -\sum_{j=1}^{N_b} \frac{9v^{EV}}{2}\left(\frac{3}{4\sqrt{\pi}}\right)^3 \lambda^{9/2} \exp\left(-\frac{9}{4}\lambda \left\|r_j - r_i\right\|^2\right)(r_j - r_i) \qquad (4.11)$$

where v^{EV} is a tuning parameter used to match the bead spring radius of gyration to match experimental data [116]. In this work we take $v^{EV} = 0.01625$ in dimensionless units ($v^{EV} l_s^3 = 1.3 \times 10^{-4}\,\mu\text{m}^3$) which yields the correct radius of gyration for λ-DNA modeled by 111 beads with $l_s = 200$ nm [109]. A soft potential favors numerical stability over strict model accuracy.

A hard potential is often used to model the excluded volume force caused by a bead penetrating a wall. Unfortunately hard potentials can introduce numerical instabilities. Heyes and Melrose [103, 117] developed a numerically stable approximation which projects any penetrated beads the minimum distance to the surface of the wall. This approximation is computationally efficient and has shown success at modeling DNA in confinement or DNA interacting with obstacles [101, 103, 109].

The stochastic differential equations (4.7), with (4.8) – (4.11) are integrated using adaptive semi-implicit Euler's method [103, 118] with details in Appendix A. The stochastic simulation is repeated with 100 times and the first two statistical moments of the distribution are calculated.

4.2 Results and discussion

In this section we present the results from the Brownian dynamics simulations. The Brownian dynamic simulations yield the $x(t), y(t), z(t)$ coordinates of each of the beads as a function of time as they elutes through the simulated entropic trap. In this work the simulations are run for fixed number of integration steps. The elution time is recorded when the center of mass of the bead spring passes

the pitch length L the final time. The bead spring will continue to elute through multiple entropic traps during the simulation and each elution time per trap is recorded. The simulation is repeated 100 times and the mean of the elution time t for each trap and standard deviation from the first trap σ is used to calculate the resolution per trap

$$R_{trap} = \sqrt{2\ln(2)}\frac{\sigma_s + \sigma_l}{\langle t_s \rangle - \langle t_l \rangle} \tag{4.12}$$

where the subscripts s and l denote short DNA and long DNA, respectively and $\langle \cdot \rangle$ denotes the mean. Fig 4.2(a) shows the resolution per trap for a bead spring composed of 12 beads and another composed of 23 beads. When the simulation results are dimensionalized, these bead springs model 5 and 10 kbp DNA with a drag tag of size α in units of equivalent length of DNA. In fig 4.2(a) we can see the resolution improving significantly as the size of the drag tag increases. The DNA lengths are under-resolved after eluting through a single trap ($R_{trap} > 1.5$). If each trap is statistically independent of the other than the total variance is given by $\sigma_{tot} = \sigma\sqrt{n_t}$ and the total elution time is given by $t_{tot} = \langle t \rangle\, n_t$, where n_t is the number of traps, such that the total resolution is given by $R_{tot} = R_{trap}/\sqrt{n_t}$ [49]. The number of traps required to achieve resolution $R_{tot} = 1.5$ is shown in fig 4.2(b).

A physical mechanism for this improved performance can be elucidated by measuring the mobility from the simulation using

$$\mu = \frac{L}{\langle t \rangle\, E} \tag{4.13}$$

where, L is the pitch and E_0 is the applied electric field strength. The mobility measurements are shown in fig. 4.3(a). A closed form model for the mobility of end-labeled entropic trapping electrophoresis can be derived by extending

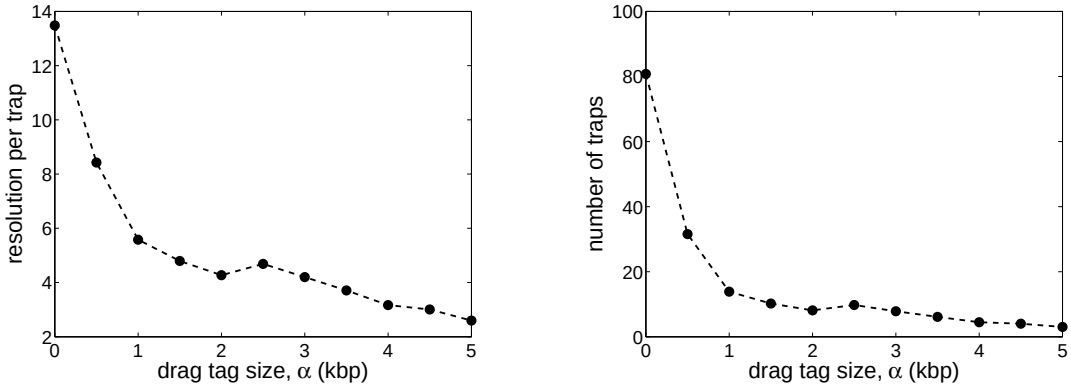

(a) (b)

Figure 4.2: (a) Resolution between 5 and 10 kbp DNA as a function drag tag size. (b) The number of traps necessary for a resolution factor of 1.5. The entropic trap is simulated with an applied electric field of 47 V/cm, pitch of 4 μm, well depth of 1.8 μm, and slit depth of 100 nm.

a mobility model for entropic trapping. The mobility of DNA in an entropic trap is modeled as

$$\frac{\mu}{\mu_\infty} = \frac{\tau_{\text{travel}}}{\tau_{\text{travel}} + \tau_{\text{trap}}} \tag{4.14}$$

where τ_{travel} is the trap free DNA travel time, τ_{trap} is the trapping time and μ_∞ is the trap free mobility of DNA [47, 49, 93, 94, 97]. The travel time is calculated by accounting for the electric field difference in the deep well and the slit, such that

$$\begin{aligned} E_d &= \frac{2h_s}{h_s + h_d} E_0 = \frac{2}{1+\gamma} E_0 \\ E_s &= \frac{2h_d}{h_s + h_d} E_0 = \frac{2\gamma}{1+\gamma} E_0 \end{aligned} \tag{4.15}$$

where h_d is the height of the deep well, h_s is the height of the slit, E_0 is the applied field strength, and $\gamma = h_d/h_s$. The travel time then follows

$$\tau_{\text{travel}} = \frac{L/2}{\mu_\infty E_d} + \frac{L/2}{\mu_\infty E_s} = \frac{L}{4\mu_\infty E_0} \frac{(1+\gamma)^2}{\gamma} \tag{4.16}$$

where the length of slit and the deep well is equivalent. The trap free mobility

is the end-labeled electrophoretic mobility given by

$$\mu_\infty = \mu_0 \frac{N}{N+\alpha} \tag{4.17}$$

where μ_0 is the free solution mobility of DNA, N is the number of DNA basepairs, and α is the size of the drag tag in units of equivalent DNA bases. The end-labeled entropic trapping electrophoretic mobility is then

$$\frac{\mu}{\mu_0} = \frac{1}{\left(1+\frac{\alpha}{N}\right) + \tau_{\text{trap}}\left(\frac{4\mu_0 E_0}{L}\frac{\gamma}{(1+\gamma)^2}\right)}. \tag{4.18}$$

Eq. (4.18) can be rearranged to calculate the trapping time τ_{trap} which is shown in fig 4.3(b). The trapping time follows an Arrhenius like expression for a polymer in a Kramer escape problem [49, 92, 93, 119, 120]

$$\tau_{\text{trap}} = \tau_0 \exp\left(\frac{\Delta U}{kT}\right) \tag{4.19}$$

where ΔU is the activation energy for DNA to escape the deep well into the slit, kT is the termal energy, and τ_0 is the pre-exponential factor. The activation energy scales with the inverse electric field strength in the slit, so that $\Delta U \sim E_s^{-1}$ and does no have any dependence on DNA size or drag. The pre-exponential factor τ_0 contains all the size relevant data. Sebastian and Paul [92], used a scaling analysis to show that DNA enters the slit by herniating, so that the pre-expontial factor scales as $\tau_0 \sim \xi_b N^{-1} E_0^{-1/2}$, where ξ_b is the drag coefficient per base. When a drag tag is attached to the DNA, the average drag per base is $\xi_b = \xi(N+\alpha)/N$ where ξ is the drag coefficient of DNA without a drag tag attached. The pre-exponential factor thus scales

as

$$\tau_0 \sim \left(1 + \frac{\alpha}{N}\right) \frac{\xi}{N\sqrt{E_0}}. \tag{4.20}$$

In fig 4.3(b) it can be seen that the trapping time is linear in the drag tag size α and solid line represents a fit of the form

$$\tau_{\text{trap}} = \frac{\beta_0}{N\sqrt{E_0}} \left(1 + \frac{\alpha}{N}\right) \exp\left(\frac{\beta_1}{E_s kT}\right) = \theta_0 + \theta_1 \alpha \tag{4.21}$$

where θ_0 and θ_1 are fitting parameters related to field strength E_0 and the DNA length N. According to the scaling analysis, the fitting parameters are related by $\theta_0 = \theta_1 N$. Least squares regression of Eq. (4.21) shown in fig 4.3(b) for 5 kbp yields parameters $\theta_0 = 0.7756$ and $\theta_1 N = 0.6810$ where as 10 kbp yields $\theta_0 = 0.3928$ and $\theta_1 N = 0.6776$. There is some discrepancy between the results shown here and what the scaling analysis predicts. This likely stems from the effect of excluded volume and the finite extensibility of the bead-springs which was not included in the analysis by Sebastian and Paul [92].

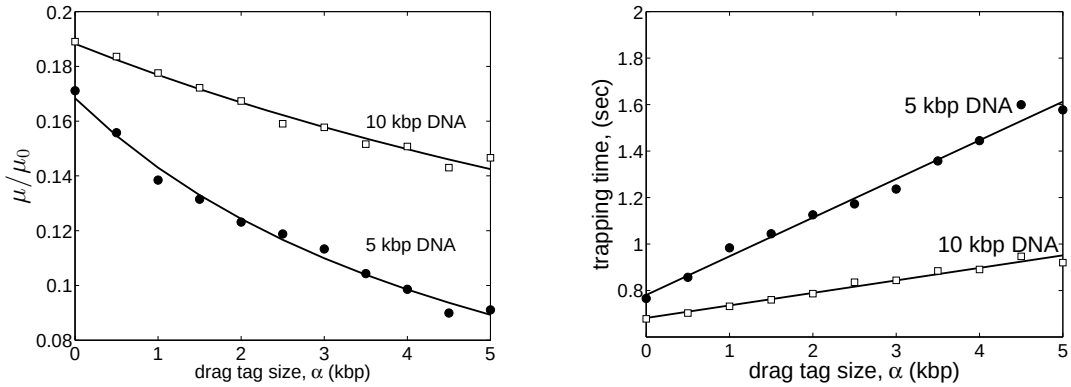

(a) (b)

Figure 4.3: (a) Mobility and (b) trapping time of tagged DNA in an entropic trap. The solid lines are fits using Eq. (4.18) with Eq. (4.21).

The physical explanation of why the trapping time depends on the drag tag size is that the drag tag effects the diffusivity D of DNA, which mani-

fested itself above as $\xi_b = \xi(N+\alpha)/N$, or equivalently $D = D_0/(N+\alpha)$, using Einstein's relation $D\xi_b N = kT$. This effects the frequency at which DNA can attempt to escape the deep well into the slit in a length dependent manner. This phenomena is the primary reason DNA can be separated according to length using an entropic trap to begin with. The addition of the drag tag exacerbates this phenomena where long DNA is not significantly effected by the drag tag and attempts to escape the deep well at about the same frequency as untagged DNA. The diffusion coefficient of short DNA, however, is significantly reduced by the addition of a drag tag leading to a lower frequency of attempted escape. The above scaling arguments are valid in the freely-draining limit (Rouse scaling) which is consistent with the simulations we performed [74]. Unfortunately, DNA diffusivity obeys Zimm scaling $D \sim N^{-0.6}$ in a good solvent due to hydrodynamic interactions [75]. This would call into the question even the scaling of our simulations results. However DNA in confinement does obey Rouse scaling [104–109, 111], although it is unclear what scaling the diffusion coefficient will obey as the DNA is in transition from the deep well to the slit. Interestingly Zhang, et al. [54] showed that including hydrodynamic interactions in a Brownian dynamics simulation of a nanopit device, which separates DNA using a similar trapping phenomena to entropic trapping, produces nearly identical scaling compared to a freely draining simulation of the trapping time with respect to DNA length, although there is strong quantitative disagreement between the predicted trapping times.

Indeed our freely draining Brownian dynamics simulations are only capable of reproducing the correct scaling from experimental data. Fig 4.4 shows the electrophoretic mobility as function of DNA length measured from both our Brownian dynamics simulations and the experimental results published by Han and Craighead [49]. Several assumptions must be made to compare

the entropic trap simulations of a single trap to experimental data of more 3700 traps. The key assumption is that the experimental data can be non-dimensionalized using the same units as the simulation shown in Eq. (4.6). These parameters will likely vary with each experiment. Another assumption is that the variance in elution time scales linearly with the number of traps n_t, so that $\sigma_{tot}^2 = \sigma_t^2 n_t$ and that the total elution time after n_t traps is $t_{tot} = tn_t$. We can then relate the variance in elution time to the variance in the electrophoretic mobility by,

$$\sigma_\mu^2 = \left(\frac{\partial \mu}{\partial t_{tot}}\right)^2 \sigma_{tot}^2 = \left(\frac{\mu}{t}\right)^2 \frac{\sigma_t^2}{n_t} \tag{4.22}$$

where $\partial\mu/\partial t_{tot} = \mu/t_{tot}$ using $\mu = L/t_{tot}E$, so that we can show the error bars in fig 4.4.

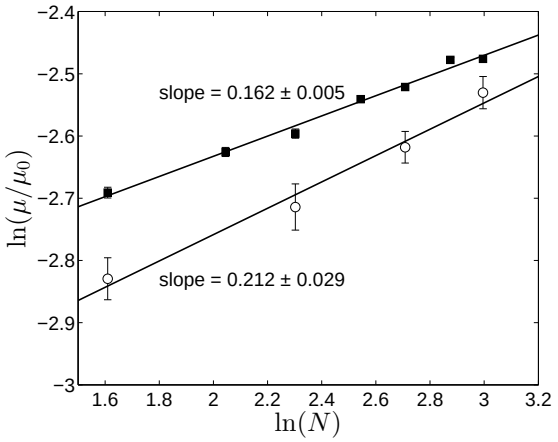

Figure 4.4: Comparison of mobility scaling from Brownian dynamics simulations (■) to experimental data from ref [49] (○). The entropic trap has a pitch of 4 μm, well depth of 1.8 μm, and slit depth of 100 nm and run with an applied field strength of 120 V/cm. The error bars are estimated from the variance in the elution time for each DNA length. Error bars for the data from the Brownian dynamics simulations are nearly the size of the markers. The solid lines are linear regressions. The data from the Brownian dynamics simulations are shifted vertically by an arbitrary constant to compare the slopes.

End-labeled entropic trapping electrophoresis (ELETE) is the combination

of two separation techniques. We shown above adding drag tags renders a significant improvement over entropic trapping alone. The question remains as to whether ELETE is an improvement over ELFSE alone. In fig 4.5 we show the mobility difference between a pair of DNA lengths as function of slit height. When the slit height is the same as the deep well, $h_s = h_d = 1.8\ \mu$m, we recover end-labeled free solution electrophoresis (ELFSE). From fig 4.5 we do indeed see an improvement for ELETE over ELFSE alone. The optimum slit height for maximizing mobility difference appears to be around 150 – 250 nm for separating 5, 10, and 15 kbp DNA with 5 kbp resolution. Interestingly the optimum separation mode for separating above 15 kbp appears to be ELFSE alone. This indicates that ELFSE out performs ELETE for long DNA for the system parameters we investigated here.

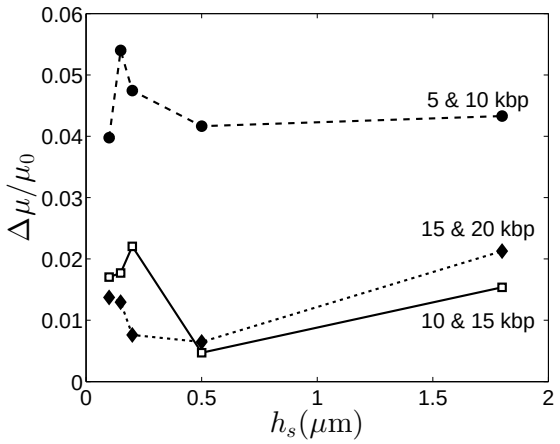

Figure 4.5: Mobility difference of tagged DNA ($\alpha = 500$ kbp) as function of slit height. At $h_s = 1.8\ \mu$m DNA is separated under end-labeled free solution electrophoresis. The mobility differences are shown for different DNA length pairs as indicated.

4.3 Summary

In this chapter we demonstrated the viability of a novel DNA separation technique that uses a hybrid of end-labeled free solution electrophoresis (ELFSE)

and entropic trapping to separate long DNA. The end-labeled entropic trapping electrophoresis separation technique is shown, through the use of Brownian dynamics simulations, to outperform both ELFSE and entropic trapping for separating DNA between 5 and 15 kbp. The physical mechanism behind this increased performance was due to an increased bias of long DNA to attempt to escape the deep well at greater frequency over short DNA. Our results have good scaling agreement with published experimental data and we expect quantitative agreement to be possible by including hydrodynamic interactions into the simulation. We expect, however, that the rational for why end-labeled entropic trapping out performs entropic trapping to remain unchanged.

Nomenclature

D	diffusion coefficient
E_0	applied electric field strength
E_d	electric field strength in deep well
E_s	electric field strength in slit
F_i^B	Brownian motion force on bead i
F_i^D	drag force on bead i
F_i^E	electrophoretic force on bead i
F_i^{EV}	excluded volume force on bead i
F_i^S	spring force on bead i
F_{dim}	force dimension in simulation
f_i	magnitude of spring force caused by stretching bead i from $i+1$
h_d	deep well height in entropic trap

h_s	slight height in entropic trap
I	idem factor
k	Boltzmann constant
L	pitch length of entropic trap
l_{dim}	length dimension in simulation
l_p	persistence length of double stranded DNA
l_s	length of spring
m	mass of DNA
N	number of DNA basepairs
N_b	number of beads
n_t	total number of traps
Pe	Peclet number
q_i	distance between bead i and $i+1$
R_{trap}	resolution per entropic trap
r_i	position vector of bead i
T	temperature
t	time
t_{dim}	time dimension in simulation
$\langle t_l \rangle$	mean elution time for long DNA length
$\langle t_s \rangle$	mean elution time for short DNA length
t_{tot}	total elution time
$\tilde{u}_i$	dimensionless electric (vector) field at position of bead i
v^{EV}	excluded volume factor
x	abscissa

y	ordinate
z	applicate
α	size of the drag tag in units of DNA bases
β_0, β_1	fitting parameters
γ	ratio of deep well height to slit height
ΔU	activation energy
δ	Dirac-delta function
θ_0, θ_1	fitting parameters
λ	ratio of spring length to persistence length
μ_∞	trap free DNA mobility
μ_i	electrophoretic mobility of bead i
σ_μ^2	variance in mobility
σ_t^2	temporal variance per trap
σ_{tot}^2	total temporal variance
σ_l	standard deviation of a long DNA length
σ_s	standard deviation of a short DNA length
τ_{trap}	trapping time scale
τ_{travel}	travel time scale
τ_0	pre-exponential factor
ϕ	potential difference in entropic trap
ξ_i	drag coefficient for bead i

Chapter 5

Approximate Dynamics from Long Simulations using Projective Integration

Large systems of non-linear differential equations are typically very computationally expensive to solve. This expense often precludes further analysis such as optimization or control studies. Stiff differential equations are particularly expensive to solve as they typically demand the use of implicit integration methods for numerical stability. Stiffness arises when the differential equations describe both fast and slow dynamics and frequently occur in chemical process systems due to chemical reactor kinetics and recycle streams [121, 122]. Proper exploitation of multiple time-scales in process systems has led to efficient control strategies, such as adaptive control, that stems from the use of reduced-order models [123].

Projective integration is a computationally efficient method for solving differential equations with both fast and slow dynamics. Projective integration works by utilizing two coupled integration methods with very different integra-

tion time steps. An inner integration is performed at small time steps to damp out fast dynamics. After a few inner integration steps an extrapolation is made over a large number of time steps which serves as the outer integration over the slow dynamics. This process is then repeated until the desired integration is completed [65]. Projective integration can be a particularly efficient method to integrate stiff differential equations because it avoids costly implicit integration methods [63]. Efficient integration of stiff differential equations represents just one example of the accelerating power of this method. Additional examples include accelerating stochastic simulation of nematic liquid crystals [124], accelerating kinetic Monte Carlo simulations of adsorption onto a metal substrate [125], and projective integration over space and time for accelerating the integration of partial differential equation [64].

Projective integration normally uses an equations-free approach that allows for cheap computations. The equations-free approach, however, is difficult to extend to yield better estimates of the interaction between states and error propagation. In this chapter we propose a projective integration scheme that uses an affine model[1] to make more accurate extrapolations for the outer integration. By applying this additional structure, important properties such as prediction error can be estimated and the projection horizon can be adjusted to balance the tradeoff between acceleration and accuracy. Related work in adaptive control has led to a number of stable and robust algorithms for extended-horizon adaptive control [126, 127]. In the following sections we outline the algorithm for adaptive projective integration and show three test problems for ordinary, stochastic and partial differential equations involving both fast and slow dynamics that can be exploited for computational speed-up using projective integration.

[1] An affine function has the form $y = Ax + b$ where A is a matrix and b is a vector.

5.1 Adaptive projective integration

This section describes the algorithm for adaptive projective integration. The system to be integrated contains both fast and slow dynamics represented by

$$\frac{dx}{dt} = g_1(x,t) + \frac{1}{\epsilon} g_2(x,t) \tag{5.1}$$

where $x \in \mathbb{R}^n$ and ϵ is a small number which indicates that the first term in the differential equation describes slow dynamics and the second term describes fast dynamics.

Projective integration uses a detailed inner integration to damp out the fast dynamics and then uses an outer integration to extrapolate over a long time horizon [63]. One such inner integration is explicit Euler's method with an integration time step, δt, at least as small as ϵ

$$x_{k+1} = x_k + \delta t \, g_1(x_k, t_k) + \frac{\delta t}{\epsilon} g_2(x_k, t_k) \tag{5.2}$$

which can be more simply written as $x_{k+1} = f(x_k)$ if we assume the system is autonomous. Because the integration time step, δt, is required to be small for numerical stability, integrating $x_{k+1} = f(x_k)$ to a long time horizon can be prohibitively expensive depending on the size and structure of $f(x)$. Typically projective integration then makes use of a linear model, identified by finite-difference, to extrapolate forward N steps [63]. After stepping the inner integration forward $h+1$ steps to damp out the fast dynamics, the outer integration is performed using

$$x_{k+h+1+N} = x_{k+h+1} + N \delta t \, s_{k+h+1} \tag{5.3}$$

where $s_{k+h+1} = (x_{k+h+1} - x_{k+h})/\delta t$ is an approximation of the rate of change of

x. This projective integration technique computes extrapolations very cheaply and does so in an "equations-free" manner [64]. In many case, however, the equation-free method is difficult implement for accurate projection whens the number of states is large. This is because the equations-free extrapolation method does not model any interactions between states within the same time step which typically do have strong interactions with each other.

We propose a method for projective integration, which can better capture the interaction between states, by fitting an affine function to the simulation data such that an accurate extrapolation can be made. This affine approximation of the system $f(x)$ takes on the form

$$y_{k+1} = Ay_k + a + w_k \tag{5.4}$$

where A is a constant matrix where the entries are found by the method of least-squares, a is a vector also fit using least-squares, and $w_k = f(x_k) - (Ay_k + a)$ is the projection error. A projection N steps into the future can be made using

$$y_{k+N} = A^N y_k + \sum_{i=0}^{N-1} A^i \left(a + w_{k+N-1-i}\right) \tag{5.5}$$

where the projection errors $w_{k+1}, w_{k+2}, \ldots, w_{k+N-1}$ are expensive to calculate. For the sake of computational efficiency, we assume that the projection error is time-invariant so that $w = w_k \approx w_{k+1} \approx \cdots \approx w_{k+N-1}$. Using the identity for a geometric series we arrive at

$$y_{k+N} = A^N y_k + (I - A)^{-1} \left(I - A^N\right) (a + w) \tag{5.6}$$

where the term $(I - A)^{-1} \left(I - A^N\right) w$ is the estimate of the error $x_{k+N} - y_{k+N}$.

Eq. (5.6) serves as the outer integration in the projective integration

method. Once the projection y_{k+N} is made using Eq. (5.6) the inner integration is restarted taking $x_{k+N} = y_{k+N}$. Because the system f is approximated by the affine function (5.4) in order to make the long time horizon projections, the projections introduce some additional integration error beyond the discretization error associated with Euler's method.

Before we summarize the projective integration method in an algorithm we will first outline theorem 5.1 which is used to determine the projection horizon as a function of the user specified error tolerance.

Theorem 5.1 *Let κw be the user specified error tolerance and $\lambda_{\max} = \max_i\{|\lambda_i|\}$ where λ_i is an eigenvalue of the matrix A in Eq. (5.4). When $\lambda_{\max} \geq 1$, the projection horizon N is bounded by*

$$N \leq \frac{\log\left(\kappa\lambda_{\max} - \kappa + 1\right)}{\log\left(\lambda_{\max}\right)} \tag{5.7}$$

so that the outer integration horizon N causes the projection error estimate $(I - A)^{-1}\left(I - A^N\right) w$ to be bounded by the error tolerance κw.

Proof. A bound on the projection horizon N can be derived several ways. For simplicity we use the eigenvalue problem

$$(I - A)^{-1}\left(I - A^N\right) w = \kappa w \tag{5.8}$$

where κ is an eigenvalue of the matrix $(I - A)^{-1}\left(I - A^N\right)$. Let λ be an eigenvalue of the matrix A so that $Av = \lambda v$. By induction we also have $A^N v = \lambda^N v$. Now we pre-multiply Eq. (5.8) by $(I - A)$ and distribute so that

$$w - A^N w = \kappa\left(w - Aw\right). \tag{5.9}$$

Recalling that the matrix $(I - A)^{-1}\left(I - A^N\right)$ is equivalent to $\sum_{i=0}^{N-1} A^i$ it then

follows that $(I-A)^{-1}\left(I-A^N\right)$ and A share eigenvectors due to the Spectral Mapping Theorem so that

$$w - \lambda^N w = \kappa\left(w - \lambda w\right) \tag{5.10}$$

which can be arranged to

$$N = \frac{\log\left(1-\kappa\left(1-\lambda\right)\right)}{\log\left(\lambda\right)}. \tag{5.11}$$

The largest eigenvalue of A yields the smallest projection horizon N resulting condition (5.7). If $|\lambda| \leq 1$ then the matrix A is stable so that

$$(I-A)^{-1}\left(I-A^N\right)w \to (I-A)^{-1}w$$

as $N \to \infty$ which may be below the user specified error tolerance κw. Because of such cases we only check condition Eq. (5.7) if $\max|\lambda| \geq 1$ $\square$.

The proposed algorithm for adaptive projective integration is as follows:

1. Starting at x_k, integrate h steps forward using the inner integrator, $x_{k+1} = f(x_k)$, to generate data $x_k, x_{k+1}, \ldots, x_{k+h+1}$.

2. Let $\phi = [x_k, \ldots, x_{k+h}]$ and $\Psi = [x_{k+1}, \ldots, x_{k+h+1}]$. Append a row vector of ones, $\mathbf{1}$, to the matrix ϕ so that $\Phi = [\phi; \mathbf{1}]$ where a semi-colon denotes a new row in the matrix. Fit the affine model $y_{k+1} = Ay_k + a_0$ using least-squares so that $\Theta = \Psi\Phi^+$ where Φ^+ is the pseudoinverse of Φ, found efficiently using a QR factorization, and $\Theta = [A, a]$.

3. Diagonalize A and calculate $N^* = \left\lfloor \frac{\log(\gamma_{\max})}{\log(\lambda_{\max})} \right\rfloor$ where $\lfloor \cdot \rfloor$ is the floor operator, $\gamma_{\max} = \kappa\lambda_{\max} - \kappa + 1$, and $\lambda_{\max} = \max\{|\lambda_i|\}$ is the largest modulus of the eigenvalues of A. If $\lambda_{\max} > 1$ set the projection horizon to $N = \min\{N^{\text{spec}}, N^*\}$, where N^{spec} is the user specified projection horizon, otherwise $\lambda_{\max} \leq 1$ and set $N = N^{spec}$.

4. Project forward N steps using $y_{k+1} = Ay_k + a$. If the eigenvalues are all unique, then we project forward efficiently using $y_{k+N} = PD^NP^{-1}y_k + PMP^{-1}a$, where $D^N = \text{diag}\{\lambda_i^N\}$, $M = \text{diag}\{(1-\lambda_i^N)/(1-\lambda_i)\}$ and P is a matrix whose columns are the eigenvectors of A, set $x_{k+h+1+N} = y_{k+h+1+N}$. When the projection is complete reset the index $k \leftarrow k+h+N+1$ and go to step 1.

The emphasis of this approach is fast and cheap computations to accelerate long simulations. In certain cases it may be advantageous to replace the matrix A in step 2 with a strictly diagonal matrix B so that the cost of diagonalization can be avoided. This introduces a tradeoff with accuracy, however, as the diagonal matrix B contains less information than the full least-squares solution A and the projection $y_{k+h+1+N}$ is correspondingly less accurate. Ultimately using a strictly diagonal matrix B will require smaller projection horizons N which can lead to increased CPU time yet again. Another approach is to omit step 3 in the algorithm completely. This approach requires some experimentation to identify a projection horizon N^{spec} that appropriately balances accuracy and acceleration of the simulation.

5.2 Applications in ordinary and stochastic differential equations

In this section we outline two useful examples to illustrate the algorithm for adaptive projective integration. The first example problem is a Brusselator with rapidly replenished source. This non-linear system describes an oscillating chemical reaction [63]. The following differential equations for the Brusselator with a rapidly replenishing source are

$$\begin{aligned} \frac{dx_1}{dt} &= \frac{p_1 - x_1}{p_2} - x_1 x_2 \\ \frac{dx_2}{dt} &= p_3 - (x_1 + 1)\, x_2 + x_2^2 x_3 \\ \frac{dx_3}{dt} &= x_1 x_2 - x_2^2 x_3 \end{aligned} \tag{5.12}$$

where the terms x_1 and p_3 represent the concentration of the reagents and the terms x_2 and x_3 represent the concentration of the products. The chemical reaction takes place in a large reservoir of reagents leading to the concentration, p_3, to be constant. The second reagent is rapidly replenished to its set point p_1 with a time scale p_2. The system has an unstable stationary point at $x_1 = p_1$, $x_2 = p_3$ and $x_3 = p_1/p_3$ and all other points lead to a stable limit cycle. The terms p_1, p_2 and p_3 are constant parameters with values $p_1 = 3$, $p_2 = 10^{-4}$, and $p_3 = 1$. The initial conditions are $x_1(0) = p_1$, $x_2(0) = p_3 + 0.1$, and $x_3(0) = p_1/p_3 + 0.1$. The system of differential of equations is stiff and is integrated using explicit Euler's method to $t_k = 10$ with a time step $\delta t = p_2 = 10^{-4}$. The results from explicit Euler's method are used as the standard to compare against the results from Adaptive Projective Integration.

Results are shown in figure 5.1 for different error factors $\kappa = 10^3$ and $\kappa = 10^6$. In step 1 of the algorithm the full simulation is integrated forward

4 steps. The affine model is then fit and the projection horizon is specified according to the error factor. When the affine model $y_{k+h+1} = Ay_{k+h} + a$ is stable the projection horizon is $N^{spec} = 10240$ otherwise the projection horizon is bounded by Eq. (5.7). In figure 5.1 we see that adaptive projective integration with an error factor $\kappa = 10^3$ leads to good agreement with data produced using Euler's method alone with correlation coefficients $r^2 = 0.79$, 0.81, and 0.79 for the states x_1, x_2, and x_3, respectively. When the error factor is set to $\kappa = 10^6$ the error increases substantially and the correlation coefficients drop to $r^2 = 0.01$, 0.02, and 0.01. Regardless of the large error introduced during the adaptive projective integration, we can see that the integration recovers quickly to the correct trajectory so that the error in the states at $t_k = 10$ is commensurate to when $\kappa = 10^3$. In this example the stable limit cycle helps to correct any over projections that occur. The CPU times for adaptive projective integration with $\kappa = 10^3$ and $\kappa = 10^6$ are 0.049 s and 0.016 s compared to 0.835 s using Euler's method alone. These computations were performed in MATLAB(R) using a desktop PC equipped with an Intel(R) i7 2.93 GHz quad-core processor ran in serial.

As the emphasis is on efficient computations, the algorithm for adaptive projective integration may be modified to better suit these needs. One approach is to omit step 3 of the algorithm which adjusts the projection horizon according to the user specified error factor κ and the eigenvalues of the fit matrix A. By omitting this step, the diagonalization of A is avoided but the projection horizon cannot be corrected. The user must typically specify a smaller projection horizon so that the projective integration algorithm does not introduce too much error. The integration results from using projective integration with an integration horizon $N^{spec} = 2560$ are nearly indistinguishable from the results generated by Euler's method with correlation coefficients

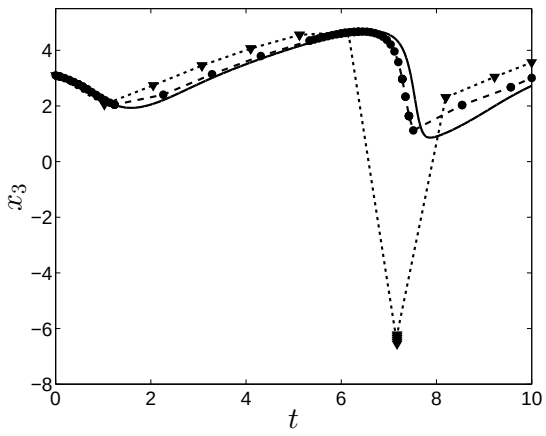

Figure 5.1: Brusselator example results. Euler's method is compared to the results from adaptive projective integration. The lines (——), $(-\bullet-)$, and $(\cdots\blacktriangledown\cdots)$ corresponds to Euler's method, projective integration with error factor $\kappa = 10^3$, and projective integration with error factor $\kappa = 10^6$, respectively. The specified projection horizon is $N^{spec} = 10240$ for both cases.

$r^2 = 0.999$, 0.996 and 0.999 for states x_1, x_2, and x_3, respectively. As the projection horizon is increased to $N^{spec} = 10240$ the correlation coefficients drop to $r^2 = 0.010$, 0.026, and 0.013. The CPU times for projective integration with a fixed horizon are 0.006 s and 0.002 s using $N^{spec} = 2560$ and $N^{spec} = 10240$, respectively, compared to 0.835 s using Euler's method alone. Projective integration also outperforms commercial integrators designed for stiff differential equations such as ode23s in MATLAB(R) which requires 0.02 s of CPU time to integrate Eq. (5.12) to the default accuracy.

Another useful example simulates DNA migrating through a microfabricated obstacle course under the action of electrophoresis. Here DNA is represented by N_b beads connected by springs. A momentum balance yields the stochastic differential equation

$$dr = \left(F^{elec}(r) + F^{EV}(r) + F^{s}(r)\right) dt + \sqrt{2}\, dw \tag{5.13}$$

where $r = [x_1, y_1, z_1, x_2, y_2, z_2, \ldots]^T$ is a vector containing the (x, y, z) coordi-

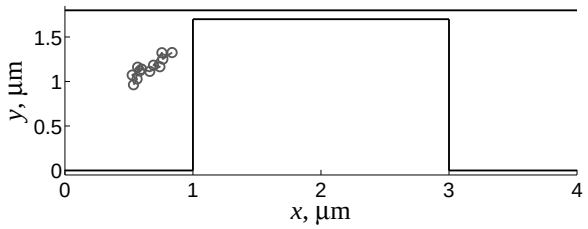

Figure 5.2: A bead-spring model in an obstacle course

nates of each bead, $F^{elec}(r)$ provides the force applied by the electric field in the obstacle course, $F^{EV}(r)$ is the excluded volume term that prevents the beads from overlapping, $F^{s}(r)$ is the spring force term that keeps the beads connected, and dw is a Wiener process represented by Gaussian white noise with zero mean and variance dt which accounts for Brownian motion.

The look up table for $F^{elec}(r)$ is generated by solving Laplace's equation $\partial^2 V/\partial x^2 + \partial^2 V/\partial y^2 = 0$ over the interior of the obstacle course, shown in figure 5.2, with homogeneous Neumann boundary conditions on the walls and Dirichlet boundary conditions of $V(0, y) = V_{app}$ and $V(1, y) = 0$. Laplace's equation is solved using the MATLAB PDE toolbox. The force can the be calculated using $F^{elec}(r) = -\nabla V$ and converted to units consistent with the simulations. The magnitude of the spring force term is given by

$$f_i = \frac{\lambda q_i}{\left(1 - q_i^2\right)^2} - \frac{7 q_i}{\left(1 - q_i^2\right)} + C_s q_i + D_s q_i \left(1 - q_i^2\right) \tag{5.14}$$

where $q_i = \|r_{i+1} - r_i\|$ is the distance between bead $i+1$ and bead i, λ is a unit fixing constant, C_s and D_s are constants, and the total spring force for each bead i is calculated by $F_i^s(r) = f_i \left(r_{i+1} - r_i\right)/q_i - f_{i-1} \left(r_i - r_{i-1}\right)/q_{i-1}$ [115]. The excluded volume term in Eq. (5.13) prevents the beads from overlapping

and is given by

$$F_i^{EV} = -\sum_j \frac{9v^{EV}}{2}\left(\frac{3}{4\sqrt{\pi}}\right)^3 \exp\left(-\frac{9}{4}\lambda \left\|r_j - r_i\right\|^2\right)(r_j - r_i) \tag{5.15}$$

where v^{EV} is constant parameter that specifies the strength of the repulsion between beads [128].

The stochastic differential equation (5.13) has $3N_b$ equations. These are solved N_e multiple times using a semi-implicit Euler's method [118] with N_t integration steps to yield estimates of the first two moments of r. In our example we use $N_b = 12$, $N_t = 5 \times 10^5$, and $N_e = 100$ with an integration time step $\delta t = 5 \times 10^{-4}$. The simulation requires 70.14 minutes of wall-clock time to complete the simulation using a desktop PC equipped with an Intel(R) i7 2.93 GHz quad-core processor ran in parallel using MATLAB(R).

The simulation of DNA electrophoresis in an obstacle course generates the (x, y, z) coordinates for each bead as they evolve through time. The size of the DNA as is moves through the obstacle course is indicated by the radius of gyration,

$$R_g^2 = \frac{1}{N_b}\sum_{i=1}^{N_b}\left\langle (r_i - r_{cm})^2 \right\rangle \tag{5.16}$$

where r_{cm} is the center of mass of the DNA and the brackets $\langle\cdot\rangle$ indicate an ensemble average over the N_e simulation realizations. The radius of gyration from the simulation is shown in figure 5.3. We apply the version of our adaptive projective integration method which fits a strictly diagonal matrix B for outer-integration model $y_{k+1} = By_k + b_0$ where $y_k = \langle r(t_k)\rangle$. The projection horizon is set at $N^{spec} = 5000$ and step 3 of the algorithm adaptive projective integration algorithm is omitted. The results from figure 5.3 show that projective integration results in overshooting the actual trajectory of the simulation, but the stability and dissipative properties of the simulation quickly correct

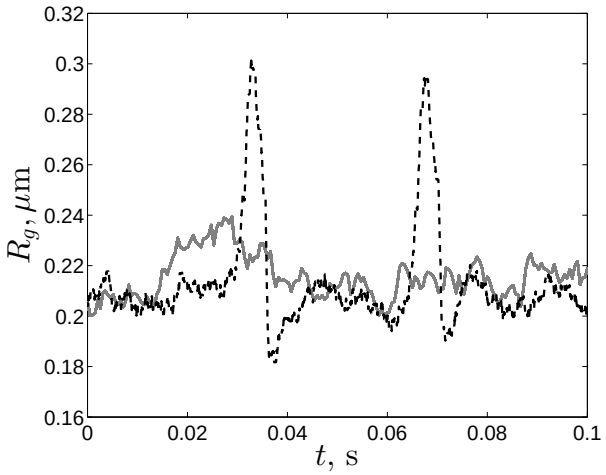

Figure 5.3: Radius of gyration of DNA as it migrates through the obstacle course. Integration results of Eq. (5.13) using semi-implicit Euler's method (—) are compared against adaptive projective integration (− −).

the overshoot and bring the results from the different integration techniques into qualitative agreement with each other. In general, quantitative agreement from stochastic simulations cannot be achieved without using a large number of realizations. The wall-clock time using adaptive projective integration is 57.48 minutes which is only a small decrease over the full simulation time of 70.14 minutes.

5.3 Applications to oil reservoir simulations

Oil reservoir simulations present a particularly interesting application for projective integration. Typical oil reservoir simulations, such as ECLIPSE by Schlumberger, solve systems of partial differential equations to determine the flow rates of oil, water, and gas out of the reservoir. The partial differential equations are discretized in space using finite volume method which results in a large system of ordinary differential equations which are integrated to describe the time evolution of the states. The simulations are computationally expensive due to the large number of grid blocks used to yield a high fidelity

simulation of the oil reservoir. Furthermore, it is not a straightforward process to implement many simulation acceleration techniques, such as reduced-order modeling, since most simulations are closed commercial software packages. Projective integration, however, is well suited for use with commercial software packages as the inner integrations can be performed by the commercial simulator and the outer integration can be performed by the user.

To test projective integration we use a simulation of a two dimensional square, with thin constant depth, oil reservoir with production wells in the four corners and water injection in the center which is similar to case considered previously in the literature [129]. The model is described in detail in Appendix B and can be summarized as implicit ODEs

$$\begin{aligned} f_o\left(P, S_w, \frac{dP}{dt}, \frac{dS_w}{dt}\right) &= 0 \\ f_w\left(P, S_w, \frac{dP}{dt}, \frac{dS_w}{dt}\right) &= 0 \end{aligned} \tag{5.17}$$

where $P \in \mathbb{R}_{+}^{N_{bk}}$ and $S_w \in \mathbb{R}_{[0,1]}^{N_{bk}}$ are vectors containing the pressure and saturation of water (volume fraction) at each grid block, $f_o(\cdot) \in \mathbb{R}^{N_{bk}}$ and $f_w(\cdot) \in \mathbb{R}^{N_{bk}}$ where N_{bk} is the total number of blocks. In the example shown here we use a 21×21 grid for a total of $N_{bk} = 441$ grid blocks, or 882 states. The model is a good candidate for potential speed up from using projective integration due to its exhibiting both fast dynamics in the pressure field and slow dynamics in the saturation field. In fact this property is commonly exploited when integrating the oil reservoir model using the popular IMPES (implicit pressure, explicit saturation) method.

Many commercial solvers utilize an adaptive time step to make the time integration more computationally efficient. We use an adaptive time step algorithm similar to the one used in *simsim* (simple simulator) developed by

Prof. Jan Dirk Jansen at TU Deflt

$$\delta t_{\mathrm{k+1}} = \delta t_k \frac{\Delta S_w^{\mathrm{target}}}{\|S_w^k - S_w^{k-1}\|_\infty} \tag{5.18}$$

where δt_k is the integration time step used in the kth integration step and $\Delta S_w^{\mathrm{target}} = 0.2$ is the target change in saturation per time step. The time step is initialized at $\delta t_1 = 30$ days. The non-linear equations that follow from time integration of Eq. (5.17) are solved using Newton's method. If Newton's method cannot satisfy the error tolerance $f^T f \leq 10^{-4}$, where $f^T = [f_o^T, f_w^T]$ from Eq. (5.17), fails to descend, or encounters a singular Jacobian matrix during one of the integration steps, then we shrink δt by 75%, i.e. $\delta t \rightarrow 0.25\,\delta t$, and re-attempt Newton's method for a maximum of ten times per integration step. The next time step increases according to Eq. (5.18) to a maximum of $\delta t^{\max} = 30$ days.

The projective integration algorithm we developed above assumes a discrete time formalism. Since the integration time step δt^k changes with each integration, it is more convenient to use a continuous time representation of the model. To build a simple model that can be cheaply projected, we build a matrix of approximate time derivatives of $u^T = [P^T, S_w^T]$, so that

$$\dot{u}_k = \frac{u_{k+1} - u_k}{t_{k+1} - t_k} + \mathcal{O}(\delta t_k) \tag{5.19}$$

where $\dot{u}_k$ denotes the time derivative at time step k. An affine model $\dot{u} = Bu + b$ can then be found using least squares as described above. The algorithm proceeds as previously discussed after a discrete time model $u_{k+1} = Au_k + a$ is recovered by using the implicit Euler's method such that $A = (I - B\,\delta t_n)^{-1}$ and $a = A\,b\,\delta t_n$ where δt_n is the last time step used before the model fit.

The results for integrating Eq. (5.17) using implicit Euler's method and

projective integration are shown in fig. 5.4. For these results, implicit Euler's method uses 75 integration steps where as projective integration uses 15 steps of implicit Euler's method then project forward 3 time steps using an affine model $u_{k+1} = Au_k + a$ and repeats the process a total of four 4 times.

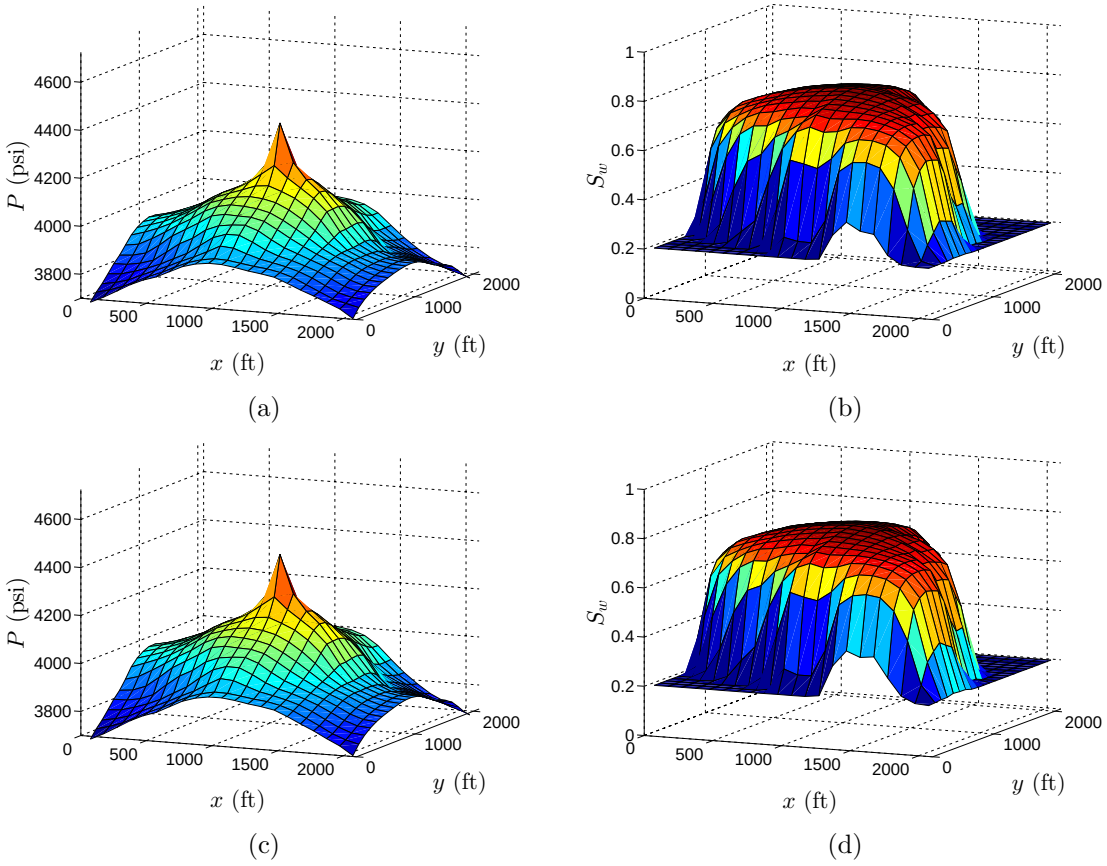

Figure 5.4: Oil reservoir simulation showing the oil field status after 1.55 years of production. The simulation integrates two PDEs in space using finite volume method and time integration is performed using implicit Euler's method (5.4(a) and 5.4(b)) or projective integration (5.4(c) and 5.4(d)).

The results in fig 5.4 show that projective integration produces consistent results to the full simulation although some error is introduced. The errors decrease when the inner integrator is used. This property follows from the highly dissipative nature of oil reservoirs. The dissipation causes most perturbations to be reduced as the system returns to a fast-attracting manifold [64].

Simulations that require solving partial differential equations are an attractive example for projective integration as it is straightforward to scale up the problem size by refining the discretization. The CPU time scaling for the oil reservoir simulation is shown in fig. 5.5. Here we see that projective integration scales almost identically to implicit Euler's method, which calls into question its utility as an fast integration scheme. It does, however, result in a 0.7 min to 1.9 minute reduction in CPU time over implicit Euler's method for this problem.

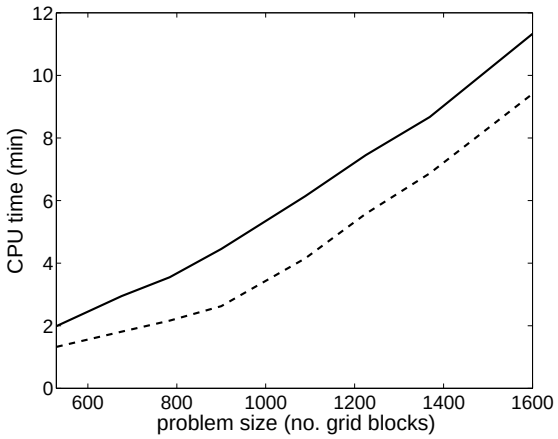

Figure 5.5: CPU time scaling for integrating the oil reservoir simulation using implicit Euler's method (—) and projective integration (– –).

Projective integration does not render a significant improvement over Euler's method for the oil reservoir simulation. This is perhaps not surprising when considering the projective integration is performed by extrapolating a linear regression model. In order for the model to be unique there must be more data than states which in our case implies that we need to run the simulation long enough to yield the sufficient quantity of data. Running the simulation for a long time is precisely what we are trying to avoid, however, which leads us to the situation where we must utilize models derived from under-determined linear regression. Since the problem is under-determined the solution to the linear regression is non-unique. There are several methods available to regu-

larize the linear regression, such as ridge regression and the LASSO, so that model predictions can be improved [130]. In this work, we found that solving the under-determined linear regression by application of QR factorization gave sufficient performance. Although the model predictions may be improved by regularization, the QR factorization method is very cheap to perform. Furthermore when the linear regression is under-determined, properties of the QR factorization are such that the matrices produced are sparse [131], which also allows for very cheap extrapolations of the linear regression model. The LASSO may otherwise be useful in this context as it also renders a sparse model but with improved model prediction properties. The LASSO requires solving a quadratic program, however, which likely nullifies any performance improvements due to the increased computational cost.

Improved model prediction may also be possible by parametrization of the pressure and saturation fields so that the number of states is reduced. We attempted two parametrization techniques: the discrete cosine transform, which has had success in parameterizing pressure and saturation fields for use in oil reservoir simulations [132, 133], and using a quadratic basis function to parametrize the saturation field while leaving the pressure at a full state description. Unfortunately, neither method resulted in appreciable improved performance, although other parametrization techniques may yield better results.

5.4 Summary

Adaptive projective integration is a method for computationally inexpensive integration of differential equations. In the algorithm, the differential equation is integrated forward for a small number a steps which generates data

that is used to construct an affine model. The linear model is used to project forward a large number of steps. Based on the eigenvalues of the linear model the projection horizon can be adjusted to help avoid large errors during the integration. We used the Brusselator problem as an example to highlight the different features of our approach. We found that using projective integration with a fixed projective horizon yields the best tradeoff between computational speed up and accuracy giving nearly an identical answer to Euler's method but with two orders of magnitude speed up in CPU time for the Brusselator problem. Less impressive speed up is observed using the stochastic simulation of DNA and the oil reservoir simulation. Modifications to the proposed method may provide better speed-up. However, the simple ideas motivated by adaptive control theory tested here do not yield sufficient speed-up to merit the application of projective integration for the problems considered here.

Nomenclature

A	constant matrix
a	constant vector
C_s, D_s	spring coefficients
dw	wiener process
F^{elec}	electrophoretic force
F^{EV}	excluded volume force
F^s	spring force
h	number of steps of inner integration
N	projective integration

N^*	projection horizon specified by error control
N^{spec}	user specified projection horizon
N_b	number of beads
N_{bk}	number of blocks
N_e	number of realizations of stochastic simulation
N_t	number of time steps
P	pressure
p_j	fixed parameters
q_i	distance between bead i and $i+1$
r	vector of positions
R_g	radius of gyration
S_w	saturation of water
t	time
v	eigenvector
V	potential difference
v^{EV}	excluded volume factor
w_k	projection for step k
x	state vector
y	approximation of state vector
δt	integration time step
ϵ	some small parameter
Θ	matrix of parameters found by linear regression
κ	user specified error factor
λ	eigenvalue, unit fixing constant

ϕ, Φ, Ψ	data matrices used for linear regression

Chapter 6

Stability of the multi-component distillation column

The distillation column is one of the primary unit operations for separations in the chemical and petroleum industries. Because of their significance, the literature for theory and practice of distillation columns is vast and mature. Despite the plethora of available theory, however, a general stability analysis of the multi-component distillation column has yet to be made.

Acrivos and Amundson [134] were the first to show that a distillation column modeled by constant molar overflow, and constant vapor-liquid equilibrium relations are asymptotically stable. Unfortunately, few columns can be accurately modeled by constant vapor-liquid equilibrium relations, which limits the scope of this work. Rosenbrock [19, 20] used Lyapunov's second method to show asymptotic stability of a binary distillation column modeled using constant molar overflow and Murphey efficiencies. Unfortunately, Rosenbrock's analysis is difficult to apply in the multi-component case. Doherty and

Perkins [135] developed a stability analysis for the multi-component distillation column modeled by constant molar overflow. It was later revealed that this analysis suffers a fatal flaw that cannot be easily rectified [136]. Rouchon and Creff [137] developed a stability analysis based on thermodynamics for the multi-component flash, but this analysis is difficult to extend to multi-stage distillation columns. Aggarwal and Ydstie [136] used contraction analysis and thermodynamics to show stability of the multi-component distillation column, but the analysis makes a few restrictive modeling assumptions that may be difficult to satisfy in practice.

In this chapter, we present an analysis for the multi-component distillation column that utilizes the thermodynamics availability function, first employed by Alonso and Ydstie [66], to show asymptotic stability of the distillation column using pressure, temperature, and level controllers on the reboiler and condenser. For this analysis, we model the multi-component distillation column as a stack of independent mass exchange units. This allows us to develop a Lyapunov function for each individual mass exchange unit, such that the overall Lyapunov function for the distributed system can be devised [138].

6.1 Modeling of the multi-component distillation column

The multi-component distillation column is governed by mass and energy balance such that

$$\begin{aligned} \frac{dN_i}{dt} &= V_{i-1}y_{i-1} + L_{i+1}x_{i+1} - V_i y_i - L_i x_i + F_i z_i^f \\ \frac{dU_i}{dt} &= V_{i-1}h_{i-1}^v + L_{i+1}h_{i+1}^l - V_i h_i^v - L_i h_i^l + F_i h_i^f + Q_i \end{aligned} \tag{6.1}$$

where $N_i = [N_{i,1}, \cdots, N_{i,n_c}]^T$ is molar hold-ups of each component on tray i, V_i and L_i are the vapor and liquid molar flow rates out of tray i, $y_i = [y_{i,1}, \cdots, y_{i,n_c}]^T$ and $x_i = [x_{i,1}, \cdots, x_{i,n_c}]^T$ are mole fractions of each component of tray i, F_i is the feed rate to tray i, $z_i^f = [z_{i,1}^f, \cdots, z_{i,n_c}^f]^T$ is the mole fraction of each component in the feed, n_c is the total number of components, U_i is the internal energy of the mixture on tray i, h_i^v and h_i^l is the molar enthalpy of the vapor and liquid part of the mixture on tray i, h_i^f is the molar enthalpy of feed, and Q_i is the external heat flow rate into tray i. The only trays with any external heat flow are the reboiler $Q_1 = Q_R$ and the condenser $Q_n = -Q_C$.

The model for the distillation column is complete by modeling each tray as an equilibrium stage such that

$$w_i^v = w_i^l \tag{6.2}$$

where $w_i = [1/T, P/T, -\mu_1/T, \cdots, -\mu_{n_c}/T]^T$ are the potentials of the vapor in tray i.

6.2 Availability of the mass exchange unit

In this section, we outline the availabilty function we use to show stability of the multi-component distillation column. The thermodynamic definition of the potentials is derived directly from the entropy such that

$$w = \frac{\partial S}{\partial z} \tag{6.3}$$

or equivalently, $dS = w^T dz$, where $z = [U, V, N_1, \cdots, N_{n_c}]^T$ are conserved inventories, T is the temperature, P is the pressure, μ_k is the chemical potential of component k, U is the internal energy, V is the volume, N_k is the number of

moles of component k, and n_c is the total number of components. The potentials are commonly referred to as intensive variables, i.e. they are independent of the size of the system. Thus the potentials are homogeneous degree zero $w(\lambda z) = w(z)$. The Gibbs-Duhem equation $dw^T z = 0$ directly follows [139]. This allows the entropy to be expressed in compact form

$$S = w^T z. \tag{6.4}$$

The entropy is maximized when a system has reached thermodynamic equilibrium, such that entropy is a concave function. Because of the concavity of entropy, we can use it to build a candidate Lyapunov function. Unfortunately the entropy does not possess the desired boundedness properties need for the analysis. We, therefore, define the availability

$$A(w^*, z) = (w^*)^T z - S(z) \tag{6.5}$$

where w^* is a fixed reference potential. The availability measures the dis-

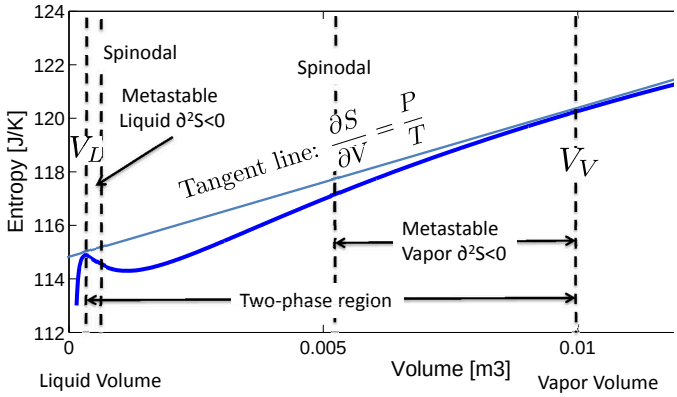

Figure 6.1: Availability of propane using the Van der Waals equation of state. Reprinted from Lin 2009 [140]

tance between the entropy $S(z) = w^T z$ and a supporting hyperplane, such that the availability is non-negative. The availability is used here due to its

favorable boundedness qualities [66]. The availability is zero when $w^* = w$ which is where the supporting hyperplane is tangent to the entropy curve. With sufficient controls, the availability can be used to form a candidate Lyapunov function which can be used to show stability of a dynamical system. A Lyapunov function must be strictly positive and decreasing with time to show asymptotic stability of a system. The rate of change of the availability is given by

$$\frac{dA}{dt} = -\left(w - w^*\right)^T \frac{dz}{dt} - \frac{dw}{dt}^T z$$

which is simplified considerably using the Gibbs-Duhem equation $dw^T z = 0$ or

$$\frac{dA}{dt} = -\Delta w^T \frac{d\Delta z}{dt} \tag{6.6}$$

where $\Delta w = w - w^*$, $\Delta z = z - z^*$ and we have held the equilibrium state z^* fixed such that $dz^*/dt = 0$. The availability is then a useful quantity for a stability analysis as the sign of the dA/dt is something that can be checked in a straightforward manner. We will next see an example of how the availability can be used to show stability of a multi-component distillation column.

The model of the distillation column is a system of differential algebraic equations (DAE) of index two [141]. Lyapunov stability theory does not directly apply to DAEs, however, the model can be reformulated to a system of ordinary differential equations by appropriate differentiation of the algebraic equations [137, 142]. The reformulation shows that if the inventories z are stable, then the potentials w are coerced into stability. It is therefore useful to consider the differential equations that model each phase as an independent *mass exchange unit*. The mass exchange unit is models the mass and energy

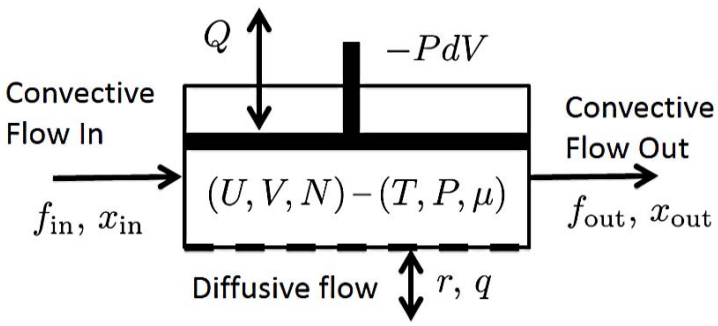

Figure 6.2: A mass exchange unit

balance of each liquid or vapor phase in each tray, such that

$$\begin{aligned}\frac{dU}{dt} &= f_{\text{in}}h_{\text{in}} - f_{\text{out}}h_{\text{out}} + rh_r + Q + q - P\phi \\ \frac{dV}{dt} &= \phi \\ \frac{dN}{dt} &= f_{\text{in}}x_{\text{in}} - f_{\text{out}}x_{\text{out}} + r\end{aligned} \tag{6.7}$$

where f_{in} is the molar flow rate into the mass exchange unit, r is the molar exchange rate between phases, q is external heat flow transferred between phases, and ϕ is the exchange of fluid volume between phases. Because the mass exchange unit models each independent phase, no equilibrium equations are considered.

The stability analysis developed in the previous section can now be directly employed. Starting with the availability $A(w^*, z) = -\Delta w^T z$, the rate of change is given by Eq. (6.6), and combined with Eq. (6.7) to give

$$\begin{aligned}\frac{dA}{dt} = &- \Delta\left(\frac{1}{T}\right)\Delta(f_{\text{in}}h_{\text{in}} - f_{\text{out}}h_{\text{out}} + rh_r + Q + q - P\phi) \\ &- \Delta\left(\frac{P}{T}\right)\Delta\phi \\ &+ \Delta\left(\frac{\mu}{T}\right)\Delta(f_{\text{in}}x_{\text{in}} - f_{\text{out}}x_{\text{out}} + r)\,.\end{aligned} \tag{6.8}$$

Eq. (6.8) can be expressed in a more useful form for the stability analysis (see

Appendix C for derivation)

$$\begin{aligned}\frac{dA}{dt} =& f_{\text{in}}(\tilde{A}+\tilde{A}^*)_{\text{in}} + \left(\frac{1}{TT^*}\right)_{\text{in}} \Delta P_{\text{in}} \Delta(Tfv)_{\text{in}} - \Delta X^T \Delta J \\ & - f_{\text{out}}(\tilde{A}+\tilde{A}^*)_{\text{out}} - \left(\frac{1}{TT^*}\right)_{\text{out}} \Delta P_{\text{out}} \Delta(Tfv)_{\text{out}} \\ & - \Delta\left(\frac{1}{T}\right) \Delta Q \\ & - \left(\frac{1}{TT^*}\right) \Delta P \Delta(T\phi) - \Delta\left(\frac{1}{T}\right) \Delta q - \Delta\left(\frac{1}{T}\right) \Delta(rh_r) + \Delta\left(\frac{\mu}{T}\right)^T \Delta r \end{aligned} \tag{6.9}$$

where the first line denotes availability flow and dissipation in the mass exchange unit, the second line denotes availability flow out, the third line denotes availability flow due to external heat input, and the final line denotes availability flow that is exchanged between phases. Eq. (6.9) is written in compact form using

$$\begin{aligned} X^T &= \left(\frac{1}{T_{\text{out}}} - \frac{1}{T_{\text{in}}}, -\left(\frac{\mu}{T}\right)^T_{\text{out}} + \left(\frac{\mu}{T}\right)^T_{\text{in}}\right) \\ J^T &= \left(fh, fx^T\right)_{\text{in}} \end{aligned}$$

and the intrinsic availability

$$\begin{aligned} \tilde{A} =& (w^* - w)^T \tilde{z} = -\Delta\left(\frac{1}{T}\right) u - \Delta\left(\frac{P}{T}\right) v + \Delta\left(\frac{\mu}{T}\right)^T x \\ \tilde{A}^* =& (w - w^*)^T \tilde{z}^* = \Delta\left(\frac{1}{T}\right) u^* + \Delta\left(\frac{P}{T}\right) v^* - \Delta\left(\frac{\mu}{T}\right)^T x^* \end{aligned}$$

where $\tilde{z} = (u, v, x_1, \cdots x_{n_c})^T$, where u is the molar internal energy, v is the molar volume, and x_k is the mole fraction of component k.

6.3 A Lyapunov function for the multi-component distillation column

A candidate Lyapunov function for the distillation column can now be constructed directly from the stacking of mass exchange units. The candidate

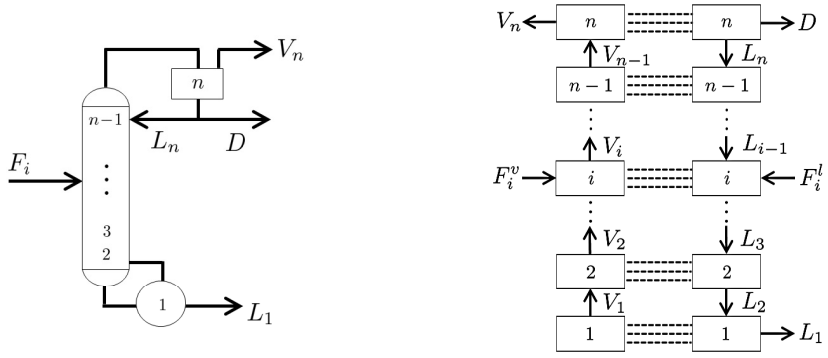

Figure 6.3: Schematic of distillation column and equivalent stack of mass exchange units. Each tray is modeled as an equilibrium stage numbered from bottom to top.

Lyapunov function is

$$W(z, z^*) = A_{tot}(w^*, z) + \frac{\epsilon_0}{2} \sum_{i=1}^{n} (N_i^{tot} - N_i^{tot,*})^2 \tag{6.10}$$

where N_i^{tot} is the total molar hold up on each tray i and $A_{tot}(w^*, z)$ is the total availability which is the sum of availabilities from each mass exchange unit used to construct a distillation column [138]. The availability measures the distance between the entropy curve and the supporting tangent hyperplane. The availability is zero at the point where the hyperplane is tangent where $w^* = w$. The inclusion of the molar hold up term in the candidate Lyapunov function ensures that

$$\begin{aligned} W(z, z^*) &> 0, \quad \forall z \neq z^* \\ W(z^*, z^*) &= 0. \end{aligned} \tag{6.11}$$

If the rate of change of the Lyapunov function candidate is uniformly negative then asymptotic stability of the distillation column then follows [28]. The rate of change of the Lyapunov function candidate is

$$\frac{dW}{dt} = \frac{dA_{tot}}{dt} + \epsilon_0 \sum_{i=1}^{n} (N_i^{tot} - N_i^{tot,*}) \frac{dN_i^{tot}}{dt} \tag{6.12}$$

where the rate of change of the total availability for the multi-component distillation column is given by

$$\begin{aligned} \frac{dA_{tot}}{dt} = & - L_1(\tilde{A}_1^l + \tilde{A}_1^{l,*}) - D(\tilde{A}_n^l + \tilde{A}_n^{l,*}) - V_n(\tilde{A}_n^v + \tilde{A}_n^{v,*}) \\ & - \frac{\Delta P_1 \Delta(T_1 L_1 v_1^l)}{T_1 T_1^*} - \frac{\Delta P_n \Delta(T_n V_n v_n^v + T_n D v_n^l)}{T_n T_n^*} \\ & - \Delta\left(\frac{1}{T_1}\right) \Delta Q_R + \Delta\left(\frac{1}{T_n}\right) \Delta Q_C \\ & - (\Delta X^T \Delta J)_{tot} \end{aligned} \tag{6.13}$$

where the equilibrium exchange rates between vapor and liquid mass exchange units are equivalent in opposite directions, i.e. $r_i^v = -r_i^l$, $h_{r,i}^v = -h_{r,i}^l$, $q_i^v = -q_i^l$, and $\phi_i^v = -\phi_i^l$, and therefore cancel. For simplicity we have assumed that there are no deviations in the feed such that $F_i = F_i^*$. It is important to note that $\tilde{A}_i^* \geq 0$ such that the availability flows obeys the inequalities

$$L_1(\tilde{A}_1^l + \tilde{A}_1^{l,*}) \geq L_1 \tilde{A}_1^l$$

$$D(\tilde{A}_n^l + \tilde{A}_n^{l,*}) \geq D\tilde{A}_n^l$$

$$V_n(\tilde{A}_n^v + \tilde{A}_n^{v,*}) \geq V_n \tilde{A}_n^v$$

where by addition we also get

$$L_1(\tilde{A}_1^l + \tilde{A}_1^{l,*}) + D(\tilde{A}_n^l + \tilde{A}_n^{l,*}) + V_n(\tilde{A}_n^v + \tilde{A}_n^{v,*}) \geq L_1 \tilde{A}_1^l + D\tilde{A}_n^l + V_n \tilde{A}_n^v$$

such that

$$\begin{aligned} L_1\tilde{A}_1^l + D\tilde{A}_n^l + V_n\tilde{A}_n^v &= \frac{L_1}{N_1^l}N_1^l\tilde{A}_1^l + \frac{D}{N_n^l}N_1^n\tilde{A}_n^l + \frac{V_n}{N_n^v}N_n^v\tilde{A}_n^v \\ &\geq \epsilon_1\Phi(w^*, z) \end{aligned} \tag{6.14}$$

with

$$\epsilon_1 = \min\left\{\frac{L_1}{N_1^l}, \frac{D}{N_n^l}, \frac{V_n}{N_n^v}\right\}$$

and

$$\Phi(w^*, z) = A_1^l(w^*, z) + A_n^l(w^*, z) + A_n^v(w^*, z)$$

where $\Phi(w^*, z) > 0$, $\forall w^* \neq w$ and $\Phi(w^*, z) = 0$, $w^* = w$. We can now state explicitly what controls will render the distillation column to be asymptotically stable.

Theorem 6.1 *The distillation column model by the dynamical system* (6.1) *with equilibrium conditions* (6.2) *has a steady state which is asymptotically stable using the feedback controls*

$$\begin{aligned} \Delta(TL_1v_1^l) &= K_1\Delta P_1 && \textit{reboiler pressure control} \\ \Delta Q_R &= -K_2\Delta T_1 && \textit{reboiler temperature control} \\ L_2 - L_1 - V_1 &= -K_3\Delta N_1^{tot} && \textit{rebolier liquid level control} \\ \Delta(T_nV_nv_n^v + T_nDv_n^l) &= K_4\Delta P_n && \textit{condenser pressure control} \\ \Delta Q_C &= K_5\Delta T_n && \textit{condenser temperature control} \\ V_{n-1} - V_n - L_n - D &= -K_6\Delta N_n^{tot} && \textit{condenser liquid level control} \end{aligned} \tag{6.15}$$

where the controller gains are positive $K_j > 0$ and the hydrodynamics of the internal trays of the column introduce negligible deviation from steady-state of the internal volumetric flow rates and internal pressures.

Proof. Beginning with the Lyapunov function candidate $W(z, z^*)$ given

in Eq. (6.10) and the rate of change given by Eq. (6.12), with Eq. (6.13), we can see that application of the temperature controller for the reboiler given by

$$\Delta Q_R = -K_2 \Delta T_1 = K_2 T_1 T_1^* \Delta\left(\frac{1}{T_1}\right)$$

and similarly for the condenser

$$\Delta Q_C = K_5 \Delta T_n = -K_5 T_n T_n^* \Delta\left(\frac{1}{T_n}\right)$$

along with the pressure controllers and inequality (6.14) renders the availability rate of change

$$\begin{aligned}\frac{dA_{tot}}{dt} \leq & -\epsilon_1 \Phi(w^*, z) - K_1 \frac{\Delta P_1^2}{T_1 T_1^*} - K_4 \frac{\Delta P_n^2}{T_n T_n^*} \\ & - K_2 T_1 T_1^* \Delta\left(\frac{1}{T_1}\right)^2 - K_5 T_n T_n^* \Delta\left(\frac{1}{T_n}\right)^2 \\ & - \left(\Delta X^T \Delta J\right)_{tot}\end{aligned} \tag{6.16}$$

where the dissipation terms $(\Delta X^T \Delta J)_{tot} \geq 0$ following the derivation in Appendix D. The remaining terms in the Lyapunov function candidate rate of change (6.12) deal with molar hold up. By inventory balance we note that for an internal tray in the distillation column without feed we have

$$\frac{dN_i^{tot}}{dt} = V_{i-1} + L_{i+1} - V_i - L_i \tag{6.17}$$

so that for the condenser and rebolier we set $dN_i^{tot}/dt = -K\Delta N_i^{tot}$, while the internal trays in the column are assumed to operate at steady state such that $dN_i^{tot}/dt = 0$, $i = 2, \ldots n-1$. Thus the rate of change of the Lyapunov

function is

$$\begin{aligned}\frac{dW}{dt} \leq & -\epsilon_1\Phi(w^*,z) - K_1\frac{\Delta P_1^2}{T_1T_1^*} - K_2T_1T_1^*\Delta\left(\frac{1}{T_1}\right)^2 \\ & - K_3\epsilon_0(\Delta N_1^{tot})^2 - K_4\frac{\Delta P_n^2}{T_nT_n^*} \\ & - K_5T_nT_n^*\Delta\left(\frac{1}{T_n}\right)^2 - K_6\epsilon_0(\Delta N_n^{tot})^2 \\ & - (\Delta X^T\Delta J)_{tot}\end{aligned} \tag{6.18}$$

where the sum terms of the right-hand-side are negative definite and asymptotic stability directly follows. □

There are two critical assumptions used to show the stability of the muli-component distillation column, specifically that the feed does not have any deviation from steady-state and that the hydrodynamics of the internal trays introduce negligible deviation from steady state of the volumetric flow rates and the pressure. These assumptions make clear our objective with this stability analysis: while it is likely apparent to practicing process engineers that standard controllers have good disturbance rejection qualities such that disturbances in the feed can be rejected out of the process after a long enough time scale and that the design of internal trays (typically sieve trays with weirs) provide good hydrodynamic stability, the proper pairing of controlled variables to manipulated variables which results in a stable multi-component distillation column is not obvious. For instance, the heat duty in the condenser is commonly manipulated to control a mole fraction specification in the distillate, rather than the temperature as we show in our analysis. Unfortunately controlling a mole fraction by manipulating the heat duty can lead to input multiplicity where an identical mole fraction can be attained at different temperatures [143, 144]. Our analysis shows directly, for the first time, what controls lead to asymptotic stability for the multi-component distillation

column.

In addition, we attempted to extend the work of Aggarwal and Ydstie by using contraction analysis to show stability [136]. The analysis proved very limited. Details can be found in Appendix E.

6.4 Summary

In this chapter we showed how the second law of thermodynamics can be used to analyze contraction and stability of non-linear systems. We showed that contraction of non-linear systems may be found using a candidate Lyapunov function constructed using the Hessian of the entropy, however the third derivatives of the entropy are needed which are only known in specific cases in which the entropy function is known in closed form. Stability analysis using the second law proves more fruitful. We used this stability analysis to show that the multi-component distillation column is stable provided proper controls are used and that the hydrodynamics of the internal trays introduce negligible deviation from steady-state.

Nomenclature

A	availability
$\tilde{A}_i^l$	molar availability of the liquid mixture on tray i
$\tilde{A}_i^v$	molar availability of the vapor mixture on tray i
D	distillate molar flow rate
f	molar flow rate in mass exchange unit
F_i	feed molar flow rate into tray i

h_i^f molar enthaply of feed going into tray i

h_i^l molar enthaply of liquid mixture on tray i

h_i^v molar enthaply of vapor mixture on tray i

J fluxes

K_j controller gain

L_i liquid molar flow rate from tray i to $i+1$

N_i vector containing the number of moles of each component on tray i

N_k number of moles of component k

P pressure

q external heat flow transferred between phases

Q_C heat flow rate into condenser

Q_i heat flow rate into tray i

Q_R heat flow rate into reboiler

r molar exchange rate between phases

S entropy

T temperature

U internal energy

V volume

V_i vapor molar flow rate from tray i to $i+1$

W Lyapunov function

w_i driving potentials of tray i

X driving forces

x_i vector containing liquid mole fractions of each component on tray i

y_i vector containing vapor mole fractions of each component on tray i

z	inventories
z^*	set point in inventories
z_i^f	vector containing mole fractions of each component in feed
Δz	deviation from set point
μ_k	chemical potential of species k
ϕ	exchange of fluid volume between phases

Chapter 7

Conclusion and Suggestions for Future Work

In this work we demonstrated how to analyze key non-linear transport and separation problems with the use of optimization, dynamics and stability analysis. This work began by showing how a general length based DNA separation problem can be posed as a non-convex non-linear programming problem. By using this formalism we were able to optimize the micelle end-labeled DNA separation technique modeled as using conventional capillary electrophoresis. In chapter 2 we identified that 600 bases could be resolved in under 50 minutes using a single capillary. Significant reductions in run time were identified when the optimization problem was reformulated for parallel capillaries. The optimal division of the separation task results in resolving 600 bases of DNA in under 5 minutes. Even more improvements were observed by using alternate detection modes. By reformulating the optimization problem, in chapter 3 to account for counter-flows and the use of snap-shot detection in conjunction with a microfluidic device, it was shown that 600 bases of DNA can be resolved in under 4.5 minutes using a controlled counter-flow and under 3.5

minutes using snap-shot detection. In chapter 4 we used Brownian dynamics simulations to show how end-labeled DNA electrophoresis can be integrated in to the entropic trapping DNA separation technique. The simulations predict significant improvements in the resolution capability of entropic trapping. Furthermore we demonstrate, through the use of a scaling analysis, that the difference in the diffusion coefficients of long and short DNA is increased by the addition of a drag tag, which results in improved separation performance. In chapter 5 we proposed a novel integration technique that makes use of linear regression to periodically extrapolate the simulation into the future such that computational time can be saved. In chapter 6 we used thermodynamics to show stability of a distillation column. We show that pressure, temperature, and level controllers on the condenser and reboiler will lead to asymptotic stability assuming that the trays operate at steady state.

7.1 Future work

1. **Experimental validation of optimization results for micelle end-labeled free solution electrophoresis**

   The future work for micelle ELFSE should focus on the experimental validation of the optimization results. At the time of this writing, only the single capillary conventional capillary electrophoresis has been verified by other workers in the lab. The other methods proposed in this thesis are currently in progress of being validated. Some feedback between the optimization and the experiments will likely be required although we do not expect significant changes to the formalism and results presented in this work.

2. **Optimal surfactant buffer design**

One of the key design variables is the size of the micelle drag tag. Although the optimization can inform the user of the optimal drag tag size, it cannot give any indication of how to achieve that size. This step is currently done in the lab by testing multiple surfactant concentrations. There is significant potential here use optimization to design large micelles that have low time average polydispersity. Recent advances in molecular design [145, 146] make this a reasonable endeavor although it is still difficult to design mixed micelle systems appropriately [147].

3. **Validation of end-labeled DNA electrophoresis in an entropic trap**

   Our Brownian dynamics simulations of entropic trapping compare well with the scaling observed from published experimental results. We expect improved agreement if hydrodynamic interactions are included in the simulation. Hydrodynamic interactions make an already expensive simulation significantly more expensive. It will therefore likely be more beneficial to attempt to experimentally validate the improved performance we predict with simulations.

4. **Utilize techniques of reduced order modeling with projective integration**

   The prediction accuracy of models derived by linear regression may, in some cases, be improved by the use of techniques such as partial-least squares, principle component analysis, and the LASSO, to name a few. This may be difficult to implement as the focus is on efficient model building and extrapolation. Perhaps the most difficult aspect of using reduced order modeling with projective integration is that the user has to be able to restart a detailed simulation after an extrapolation by a

reduced order model. This can be done using an observer algorithm although this increased computational cost will likely undo any benefit derived from using projective integration.

5. **Include detailed hydrodynamic model of internal trays in stability proof of the multi-component distillation column**

   In our stability analysis of the multi-component distillation we assumed no deviations from steady state for the internal trays. The stability proof we utilize in this work uses thermodynamics to indicate if the dynamics system will be asymptotically stable. A fairly detailed description of the transport phenomena will likely be required for the stability proof to work.

Appendix A

Numerical Methods for Brownian Dynamics Simulations

Stochastic differential equations (SDE) can be difficult to work with numerically. SDE model quantities that vary randomly overtime and are, therefore, not classically differentiable. Unlike classical calculus which is one unified theory, Stochastic calculus currently enjoys two prevailing theories, Itō and Stratonovich, which interpret the SDE differently. While Itō calculus has properties that make it useful for mathematical analysis and some physical models, Stratonovich calculus utilizes the same integration rules as deterministic calculus and is generally better suited for modeling physics [112, 148]. For the Brownian dynamics simulations we use the Euler-Maruyama method, which integrates the SDE numerically in the sense of Itō. A straightforward conversion exists between Itō and Stratonovich calculus [112]. The Euler-Maruyama method has accuracy of weak order 1 and strong order 1/2 so that the statistical moments of the true solution to the SDE and the numerical solution are within $\mathcal{O}(\delta t)$ difference of each other, but the trajectories themselves are only within $\mathcal{O}(\delta t^{1/2})$ of each other where δt is the integration step width. In this

work, we are primarily interested in the statistical moments of the solution of the SDE, so Euler-Maruyama is an adaquate solution method.

The Euler-Maruyama method for SDE (4.7) yields the stochastic difference equation

$$r_i^{k+1} = r_i^k + \left(Pe\, u_i^k + F_i^{S,k} + F_i^{EV,k} \right) \delta t + \sqrt{2\delta t}\, n_i^k \tag{A.1}$$

where $r_i^k = r_i(t^k) = \left[x_i(t^k), y_i(t^k), z_i(t^k) \right]^T$, Pe is the Peclet number, $u_i^k = u(r_i^k)$ is the unit vector field pointing in the direction of the velocity field at bead i, $F_i^{S,k} = F^S(r_{i-1}^k, r_i^k, r_{i+1}^k)$ is the dimensionless spring force acting on bead i, $F_i^{EV,k} = F^{EV}\left(r_1^k, r_2^k, \ldots, r_{N_b}^k\right)$ is the dimensionless excluded volume force, and n_i^k is a random number drawn from a normal distribution with zero mean and unit variance. Eq. (A.1) uses explicit Euler's method which will produce accurate integrations when the difference equation is stable which holds for relatively small integration steps. For most problems of interest, the difference equation must be stepped out to long horizons which introduces significant computational burden for small integration step widths.

Unfortunately large integration step widths cause numerical instabilities. As the distance between beads approaches maximum extension the spring force law (4.9) becomes extremely large so that differential equation become stiff. Numerical instability caused by stiffness can be removed by using an implicit integration method. Here we employ a semi-implicit Euler's method

$$r_i^{k+1} = r_i^k + \left(Pe\, u_i^k + F_i^{S,k+1} + F_i^{EV,k} \right) \delta t + \sqrt{2\delta t}\, n_i^k \tag{A.2}$$

where the spring force term is evaluated at the next time step $F_i^{S,k+1} = F^S(r_{i-1}^{k+1}, r_i^{k+1}, r_{i+1}^{k+1})$. The semi-implicit method is only used when the explicit method (A.1) causes over-extension, which is referred to as the "adaptive" integration method [101, 103].

The semi-implicit integration results in a series of non-linear equations in r_i^{k+1} for all i. The equations are solved using the predictor-corrector method developed by Somasi, et al. which has favorable computational efficiency over Newton's method [118]. The predictor-correct method uses a two stage corrector to evaluate the spring force $F_i^{S,k+1}$ since it requires two adjacent displacement vectors to compute.

Step 1. In the predictor stage the candidate solution r_i^p for the next time step is computed using Eq. (A.1). If the candidate solution does not introduce any over-stretching, i.e. $\left\|r_{i+1}^p - r_i^p\right\| \leq 1$, $i = 1 \ldots N_b - 1$ then the candidate solution is accepted, $r_i^{k+1} \leftarrow r_i^p$, and the integration continues. Otherwise, over-stretching has occurred and the solution must be rectified in the next two corrector stages.

Step 2. In the first corrector stage, Eq. (A.2) is re-written in terms of displacement vectors $Q_i^c = r_{i+1}^c - r_i^c$, such that

$$Q_i^c + 2f_i^c \frac{Q_i^c}{q_i^c}\delta t = Q_i^k + \left(Pe\left(u_{i+1}^k - u_i^k\right) + f_{i-1}^c \frac{Q_i^c}{q_i^c} + f_{i+1}^p \frac{Q_i^p}{q_i^p} + F_{i+1}^{EV,k} - F_i^{EV,k} \right) \delta t + \sqrt{2\delta t}\left(n_{i+1}^k - n_i^k\right) \tag{A.3}$$

where $q_i^c = \|Q_i^c\|$ is the distance between adjacent beads. The equation is solved sequentially through $i = 1 \ldots N_b - 1$ so that the right hand side is known at each iteration i. To solve Eq. (A.3), the left hand side is expanded out using the spring force law Eq. (4.9) yielding a seventh order polynomial in the distance q_i^c

$$a_7 \left(q_i^c\right)^7 + a_5 \left(q_i^c\right)^5 - R_i \left(q_i^c\right)^4 + a_3 \left(q_i^c\right)^3 + 2R_i \left(q_i^c\right)^2 + a_1 q_i^c - R_i = 0 \tag{A.4}$$

where R_i is the magnitude of the right hand side of Eq. (A.3) and the poly-

nomial coefficients are given by

$$\begin{aligned} a_1 &= 1 + 2\delta t\lambda - 14\delta t + 2\delta t C_s + 2\delta t D_s \\ a_3 &= -2 + 14\delta t - 4\delta t C_s - 6\delta t D_s \\ a_5 &= 1 + 2\delta t C_s + 6\delta t D_s \\ a_7 &= -2\delta t D_s \end{aligned} \tag{A.5}$$

where λ is the number of persistence lengths per spring and the spring force law coefficients C_s and D_s are given by Eq. (4.10). The polynomial (A.4) is guaranteed to have a root between zero and unity which correctly bounds the extension of the beads. Once q_i^c is found by solving Eq. (A.4) the vector Q_i^c can be found using Eq. (A.3).

Step 3. In the second corrector stage, we find the candidate solution Q^{k+1} using the magnitude of the spring force law f_{i+1}^c from the first corrector stage, such that

$$\begin{aligned} Q_i^{k+1} + 2f_i^{k+1}\frac{Q_i^{k+1}}{q_i^{k+1}}\delta t = Q_i^k + \left(Pe\left(u_{i+1}^k - u_i^k\right) + f_{i-1}^{k+1}\frac{Q_i^{k+1}}{q_i^{k+1}} + f_{i+1}^c\frac{Q_i^c}{q_i^c}\right)\delta t \\ + \left(F_{i+1}^{EV,k} - F_i^{EV,k}\right)\delta t + \sqrt{2\delta t}\left(n_{i+1}^k - n_i^k\right) \end{aligned} \tag{A.6}$$

As with the previous corrector step, Eq. (A.6) can be re-written as a polynomial in $q_i^{k+1} = \left\|Q_i^{k+1}\right\|$ and solved to yield the next update. If the residual is greater than the tolerance, i.e. $\sum_{i=1}^{N_b-1}\left(q_i^{k+1} - q_i^c\right)^2 \geq \eta^2$ where $\eta = 10^{-6}$, then we replace the corrector value with the current candidate, $Q_i^c \leftarrow Q_i^{k+1}$, and repeated step 3 until convergence. Once the algorithm has converged, the next time step for the position r_i^{k+1} can be found using Eq. (A.2) and calculate $F_i^{S,k+1}$ using the terms found during the final corrector stage.

Appendix B

Oil Reservoir Model

Here we present the model for a two-dimensional, oil-water reservoir of constant height h_z [22, 149–151]. Conversation of mass in a reservoir containing a compressible fluid obeys

$$\frac{\partial}{\partial t}(\rho^m \phi S^m) + \nabla \cdot (\rho^m v^m) = q^m \tag{B.1}$$

where ρ^m is the density of fluid m, ϕ is the porosity of the reservoir, S^m is the saturation (volume fraction) of fluid m, v^m is the fluid velocity, and q^m is the production or injection of fluid m. The velocity of a fluid in porous media is given by Darcy's law

$$v^m = -\frac{k^m}{\eta^m} K \nabla P^m \tag{B.2}$$

where k^m is the relative permeability , η^m is the fluid viscosity, K is the absolute permeability of the reservoir, and P^m the pressure of fluid m. In this work we take the capillary pressure to be zero such that $P^w = P^o = P$.

The permeability is a measure of the ease of migration of a fluid through the porous rock in the reservoir. If the reservoir is already occupied by another fluid then the ease of migration is lowered be a factor k_m. In this work we

model the relative permeability of a oil-water system by the Corey model [152]

$$\begin{aligned} k^o =& k^{o,0}(1-S)^{n_1} \\ k^w =& k^{w,0}S^{n_2} \end{aligned} \tag{B.3}$$

where $k^{o,0}$ and $k^{w,0}$ are the relative permeability references for oil and water, respectively, n_1 and n_2 are Corey exponents, and

$$S = \frac{S^w - S^{w,c}}{1 - S^{o,r} - S^{w,c}} \tag{B.4}$$

where S^w is the saturation of water, $S^{w,c}$ is the connate water saturation, $S^{o,r}$ is the residual oil saturation. The fraction S is projected to $S \in [0,1]$ so that $k^o \in [0, k^{o,0}]$ and $k^w \in [0, k^{w,0}]$.

At high pressure, both the fluid and the rock are compressible. We model the compressibility of oil, water, and the rock using compressibility factors

$$c_o = \frac{1}{\rho^o}\frac{\partial \rho^o}{\partial P}, \qquad c_w = \frac{1}{\rho^w}\frac{\partial \rho^w}{\partial P}, \qquad c_r = \frac{1}{\phi}\frac{\partial \phi}{\partial P} \tag{B.5}$$

where we take the compressibility factors to be constant. Integration of the compressibility factors yields exponential functions for the density of oil, water, and the porosity. A first order Taylor expansion yields a good approximation and takes on the form

$$\rho^m = \rho^{m,0}\left[1 + c_m(P - P^0)\right], \qquad \phi = \phi^0\left[1 + c_r(P - P^0)\right] \tag{B.6}$$

where $\rho^{m,0}$ is the reference density at P^0.

The equations (B.1) – (B.4), (B.6) yield two partial differential equations in P and S^w (or $S^o = 1 - S^w$). The PDEs are non-linear and are discretized

in space using a block centered finite volume method to yield the ODEs [149]

$$\begin{aligned}\frac{d}{dt}\left(\frac{\phi S^m}{B^m}\right)_{i,j} V_b =& T^m_{i+\frac{1}{2},j}\left(P_{i+1,j}-P_{i,j}\right)+T^m_{i-\frac{1}{2},j}\left(P_{i-1,j}-P_{i,j}\right)\\ &+T^m_{i,j+\frac{1}{2}}\left(P_{i,j+1}-P_{i,j}\right)+T^m_{i,j-\frac{1}{2}}\left(P_{i,j-1}-P_{i,j}\right)+Q^m_{i,j}\end{aligned} \tag{B.7}$$

where $B^m = \rho^{m,0}/\rho^m$ is the formation volume factor, $V_b = \Delta x\,\Delta y\,h_z$ is the volume of the block, and $P_{i,j}$ indicates the pressure at the center of block (i,j). The transmissibility determines the flow rate from one block to another and is calculated at the block edge $(i+\frac{1}{2},j)$ by

$$T^m_{i+\frac{1}{2},j} = \frac{k^m_{i+\frac{1}{2},j}}{\eta^m_{i+\frac{1}{2},j}B^m_{i+\frac{1}{2},j}}\frac{K_{i+\frac{1}{2},j}}{\Delta x} \tag{B.8}$$

where $\eta^m_{i+\frac{1}{2},j} = (\eta^m_{i,j}+\eta^m_{i+1,j})/2$ and $B^m_{i+\frac{1}{2},j} = (B^m_{i,j}+B^m_{i+1,j})/2$ is the viscosity and the block formation factor of the fluid at the block edge, respectively. The absolute permeability at the block edge is calculated using a harmonic mean due to its resistor like character such that

$$K_{i+\frac{1}{2},j} = \frac{2}{\dfrac{1}{K_{i,j}}+\dfrac{1}{K_{i+1,j}}}. \tag{B.9}$$

The relative permeability is calculated using an upstreaming weighting so that shock formation is consistent with analytical models [151, 153]

$$k^m_{i+\frac{1}{2},j} = \begin{cases} k^m_{i,j} & \text{if } P_{i,j} \geq P_{i+1,j} \\ k^m_{i+1,j} & \text{if } P_{i,j} < P_{i+1,j} \end{cases}. \tag{B.10}$$

The source and sink term $Q^m_{i,j}$ accounts for the injection and production of the fluid m. In this work we either set $Q^m_{i,j}$ to a constant flow rate or we set a constant downhole well pressure P_{well} and employ the Peaceman model [154]

to calculate the flow rate

$$Q^m_{i,j} = \frac{k^m_{i,j}}{B^m_{i,j}\eta^m_{i,j}} K_{i,j} J_{\text{well}} \left(P_{i,j} - P_{\text{well}}\right) \tag{B.11}$$

where $J_{\text{well}} = 2\pi h_{\text{well}} / \ln(r_{eq}/r_{\text{well}})$ is a constant well production term with height and radius of the well h_{well} and r_{well}, respectively, and equivalent radius of the block given by

$$r_{eq} = 0.14\sqrt{\Delta x^2 + \Delta y^2}. \tag{B.12}$$

Appendix C

Availability of the Mass Exchange Unit

Starting from Eq. (6.9) the expression for the rate of change of the availability is re-arranging in terms of flow and dissipation.

Using the definition for the specific molar enthalpy

$$h = u + Pv$$

where u is the molar internal energy, P is the pressure, and v is the molar volume, we get using the Δ-notation

$$\Delta(fh) = f(u + Pv) - f^*(u^* + (Pv)^*)$$

Hence

$$\Delta\left(\frac{1}{T}\right)\Delta(fh) = \Delta\left(\frac{1}{T}\right)f(u + Pv) - \Delta\left(\frac{1}{T}\right)f^*(u^* + (Pv)^*) \qquad \text{(C.1)}$$

Now we expand the work term in equation (C.1). First we note that

$$\begin{aligned}\Delta\left(\frac{1}{T}\right)Pv - \Delta\left(\frac{P}{T}\right)v &= \left(\frac{1}{T} - \frac{1}{T^*}\right)Pv - \left(\frac{P}{T} - \frac{P^*}{T^*}\right)v \\ &= -\frac{\Delta P}{T^*}v\end{aligned}$$

Hence

$$\Delta\left(\frac{1}{T}\right)Pv = \Delta\left(\frac{P}{T}\right)v - \frac{\Delta P}{T^*}v \tag{C.2}$$

Similarly we get

$$\Delta\left(\frac{1}{T}\right)(Pv)^* = \Delta\left(\frac{P}{T}\right)v^* - \frac{\Delta P}{T}v^* \tag{C.3}$$

By substituting equations (C.2) and (C.3) into equation (C.1) we have

$$\begin{aligned}\Delta\left(\frac{1}{T}\right)\Delta(fh) =& f\left[\Delta\left(\frac{1}{T}\right)u + \Delta\left(\frac{P}{T}\right)v - \frac{\Delta P}{T^*}v\right] \\ &- f^*\left[\Delta\left(\frac{1}{T}\right)u^* + \Delta\left(\frac{P}{T}\right)v^* - \frac{\Delta P}{T}v^*\right] \\ =& f\left[\Delta\left(\frac{1}{T}\right)u + \Delta\left(\frac{P}{T}\right)v\right] \\ &- f^*\left[\Delta\left(\frac{1}{T}\right)u^* + \Delta\left(\frac{P}{T}\right)v^*\right] - \frac{1}{TT^*}\Delta P\Delta(Tfv)\end{aligned}$$

Hence

$$\Delta\left(\frac{1}{T}\right)\Delta(fh) = \Delta\left(\frac{1}{T}\right)\Delta(fu) + \Delta\left(\frac{P}{T}\right)\Delta(fv) - \frac{1}{TT^*}\Delta P\Delta(Tfv) \tag{C.4}$$

This equation will be used to simplify the first two terms on the right hand side of equation (6.6). But, before doing the substitutions, we develop a few more identities. For the feed we have

$$\Delta\left(\frac{1}{T}\right)\Delta(fh)_{\text{in}} = \Delta\left(\frac{1}{T}\right)_{\text{in}}\Delta(fh)_{\text{in}} + \left[\Delta\left(\frac{1}{T}\right) - \Delta\left(\frac{1}{T}\right)_{\text{in}}\right]\Delta(fh)_{\text{in}}$$

Hence from equation (C.4)

$$\Delta\left(\frac{1}{T}\right)\Delta(fh)_{\text{in}} = \left(\Delta\left(\frac{1}{T}\right)\Delta(fu) + \Delta\left(\frac{P}{T}\right)\Delta(fv) - \frac{1}{TT^*}\Delta P\Delta(Tfv)\right)_{\text{in}} + \left[\Delta\left(\frac{1}{T}\right) - \Delta\left(\frac{1}{T}\right)_{\text{in}}\right]\Delta(fh)_{\text{in}}$$

We can also combine the work terms associated with the change of volume in equation (6.6) by noting that

$$\begin{aligned}\Delta\left(\frac{1}{T}\right)\Delta(P\phi) - \Delta\left(\frac{P}{T}\right)\Delta\phi &= \left(\frac{1}{T} - \frac{1}{T^*}\right)(P\phi - (P\phi)^*) - \left(\frac{P}{T} - \frac{P^*}{T^*}\right)(\phi - \phi^*) \\ &= -\frac{P\phi}{T^*} + \frac{P^*\phi}{T^*} - \frac{(P\phi)^*}{T} + \frac{P\phi^*}{T} \\ &= -\frac{\Delta P\phi}{T^*} + \frac{\Delta P\phi^*}{T}\end{aligned}$$

Hence

$$\Delta\left(\frac{1}{T}\right)\Delta(P\phi) - \Delta\left(\frac{P}{T}\right)\Delta\phi = -\frac{1}{TT^*}\Delta P\Delta(T\phi) \tag{C.5}$$

The identities displayed in equations (C.4) – (C.5) are now used to re-arrange equation (6.6) so that it has a more useful form. First we get the expression

$$\begin{aligned}\frac{dA}{dt} = &-\left(\Delta\left(\frac{1}{T}\right)\Delta(fu) + \Delta\left(\frac{P}{T}\right)(fv) - \frac{1}{TT^*}\Delta P\Delta(Tfv)\right)_{\text{in}} \\ &- \left(\Delta\left(\frac{1}{T}\right) - \Delta\left(\frac{1}{T_{\text{in}}}\right)\right)\Delta(fh)_{\text{in}} \\ &+ \left(\Delta\left(\frac{1}{T}\right)\Delta(fu) + \Delta\left(\frac{P}{T}\right)\Delta(fv) - \frac{1}{TT^*}\Delta P\Delta(TFv)\right)_{\text{out}} \\ &- \Delta\left(\frac{1}{T}\right)\Delta(rh_r) - \Delta\left(\frac{1}{T}\right)(\Delta Q + \Delta q) - \frac{1}{TT^*}\Delta P\Delta(T\phi) \\ &+ \left(\Delta\left(\frac{\mu}{T}\right)^T\Delta(fx)\right)_{\text{in}} + \left(\Delta\left(\frac{\mu}{T}\right) - \Delta\left(\frac{\mu}{T}\right)_{\text{in}}\right)^T\Delta(fx)_{\text{in}} \\ &- \left(\Delta\left(\frac{\mu}{T}\right)^T\Delta(fx)\right)_{\text{out}} + \Delta\left(\frac{\mu}{T}\right)^T\Delta r\end{aligned}$$

By re-arranging the terms we get the more transparent expression

$$\begin{aligned}
\frac{dA}{dt} &= -\left(\Delta\left(\frac{1}{T}\right)\Delta(fu)+\Delta\left(\frac{P}{T}\right)(fv)-\Delta\left(\frac{\mu}{T}\right)^{T}\Delta(fx)\right)_{\text{in}} \\
&+\left(\Delta\left(\frac{\mu}{T}\right)-\Delta\left(\frac{\mu}{T}\right)_{\text{in}}\right)^{T}\Delta(fx)_{\text{in}}-\left(\Delta\left(\frac{1}{T}\right)-\Delta\left(\frac{1}{T}\right)_{\text{in}}\right)\Delta(fh)_{\text{in}} \\
&+\left(\frac{1}{TT^{*}}\Delta P\Delta(Tfv)\right)_{\text{in}}-\left(\frac{1}{TT^{*}}\Delta P\Delta(Tfv)\right)_{\text{out}} \\
&+\left(\Delta\left(\frac{1}{T}\right)\Delta(fu)+\Delta\left(\frac{P}{T}\right)\Delta(fv)-\Delta\left(\frac{\mu}{T}\right)^{T}\Delta(fx)\right)_{\text{out}} \\
&-\Delta\left(\frac{1}{T}\right)\Delta(rh_{r})+\Delta\left(\frac{\mu}{T}\right)^{T}\Delta r-\Delta\left(\frac{1}{T}\right)(\Delta Q+\Delta q)-\frac{1}{TT^{*}}\Delta P\Delta(T\phi)
\end{aligned}$$

This expression simplifies considerable once we define vectors of thermodynamic driving forces and flows so that

$$\begin{aligned}
X^{T} &= \left(\frac{1}{T}-\frac{1}{T_{\text{in}}},-\frac{\mu}{T}^{T}+\left(\frac{\mu}{T}\right)_{\text{in}}^{T}\right) \\
J^{T} &= \left(fh, fx^{T}\right)
\end{aligned}$$

and the intrinsic availability

$$\begin{aligned}
\tilde{A} &= (w^{*}-w)^{T}\tilde{z}=-\Delta\left(\frac{1}{T}\right)u-\Delta\left(\frac{P}{T}\right)v+\Delta\left(\frac{\mu}{T}\right)^{T}x \\
\tilde{A}^{*} &= (w-w^{*})^{T}\tilde{z}^{*}=\Delta\left(\frac{1}{T}\right)u^{*}+\Delta\left(\frac{P}{T}\right)v^{*}-\Delta\left(\frac{\mu}{T}\right)^{T}x^{*}
\end{aligned}$$

where $\tilde{z}=(u,v,x_1,\cdots x_{n_c})^{T}$, where u is the molar internal energy, v is the molar volume, and x_k is the mole fraction of component k. The rate of change

of the availability is then given by

$$\begin{aligned}\frac{dA}{dt} =& f_{\text{in}}\left(\tilde{A}+\tilde{A}^{*}\right)_{\text{in}}+\left(\frac{1}{TT^{*}}\right)_{\text{in}}\Delta P_{\text{in}}\Delta(Tfv)_{\text{in}}-\Delta X^{T}\Delta J\\ &-f_{\text{out}}\left(\tilde{A}+\tilde{A}^{*}\right)_{\text{out}}-\left(\frac{1}{TT^{*}}\right)_{\text{out}}\Delta P_{\text{out}}\Delta(Tfv)_{\text{out}}\\ &-\Delta\left(\frac{1}{T}\right)\Delta Q-\left(\frac{1}{TT^{*}}\right)\Delta P\Delta(T\phi)\\ &-\Delta\left(\frac{1}{T}\right)\Delta q-\Delta\left(\frac{1}{T}\right)\Delta(rh_{r})+\Delta\left(\frac{\mu}{T}\right)^{T}\Delta r\end{aligned}$$

Appendix D

Dissipation in a distillation column

Here we determine the sign of the dissipation term in the distillation column. We begin with the function

$$E = (w_2 - w_1)^T j_1 \tag{D.1}$$

where $w^T = [1/T, P/T, -\mu_1/T, \cdots, -\mu_{n_c}/T]$ is are the potential variables and $j^T = [fu, fv, fx_1, \cdots, fx_{n_c}]$ are the fluxes, where f is a molar flow rate. The entropy flux $w_1^T j_1$ is concave and homogeneous degree one such that E is convex and also homogeneous degree one. We now define a driving force

$$\chi = \frac{\partial E}{\partial j_1} = w_2 - w_1 \tag{D.2}$$

which follows since Euler's theorem ensures

$$\frac{\partial w_1}{\partial j_1} = 0$$

for w_1 which is homogenous degree zero. We then get

$$\frac{\partial \chi}{\partial j_1} = R = \frac{\partial^2 E}{\partial j_1^2} \geq 0$$

Hence $Rdf_1 = d\chi$ so that

$$(\chi - \chi^*)^T (j_1 - j_1^*) \geq 0 \tag{D.3}$$

and, similarly, we get

$$(\chi - \chi^*)^T (j_2 - j_2^*) \leq 0. \tag{D.4}$$

Recalling that $\chi = w_2 - w_1$ where $w^T = [1/T, P/T, -\mu_1/T, \cdots, -\mu_{n_c}/T]$ and $j^T = [fu, fv, fx_1, \cdots, fx_{n_c}]$ we can express inequility (D.3) in the more useful form

$$\begin{aligned} \left(\Delta\left(\frac{1}{T}\right)_2 - \Delta\left(\frac{1}{T}\right)_1\right)\Delta(fu)_1 + \left(\Delta\left(\frac{P}{T}\right)_2 - \Delta\left(\frac{P}{T}\right)_1\right)\Delta(fv)_1 \\ - \left(\Delta\left(\frac{\mu}{T}\right)_2 - \Delta\left(\frac{\mu}{T}\right)_1\right)^T \Delta(fx)_1 \geq 0 \end{aligned} \tag{D.5}$$

The dissipation term in the mass exchange unit is of the form

$$\begin{aligned} \Delta X^T \Delta J = \left(\Delta\left(\frac{1}{T}\right)_{\text{out}} - \Delta\left(\frac{1}{T}\right)_{\text{in}}\right)\Delta(fh)_{\text{in}} \\ - \left(\Delta\left(\frac{\mu}{T}\right)_{\text{out}} - \Delta\left(\frac{\mu}{T}\right)_{\text{in}}\right)^T \Delta(fx)_{\text{in}} \end{aligned} \tag{D.6}$$

In order to utilize inequalities (D.3) and (D.4) in Eq. (D.6), we must first rearrange some terms. We recall from Appendix C Eq. (C.4)

$$\Delta\left(\frac{1}{T}\right)\Delta(fh) = \Delta\left(\frac{1}{T}\right)\Delta(fu) + \Delta\left(\frac{P}{T}\right)\Delta(fv) - \frac{\Delta P \Delta(Tfv)}{TT^*}. \tag{C.4}$$

Using Eq. (C.4) in (D.6) yields

$$\begin{aligned}\Delta X^T \Delta J =& \Delta\left(\frac{1}{T}\right)_{\text{out}} \Delta(fu)_{\text{in}} + \Delta\left(\frac{P}{T}\right)_{\text{out}} \Delta(fv)_{\text{in}} - \frac{\Delta P_{\text{in}} \Delta(T_{\text{out}} f_{\text{in}} v_{\text{in}})}{T_{\text{out}} T^*_{\text{out}}} \\ & - \Delta\left(\frac{1}{T}\right)_{\text{in}} \Delta(fu)_{\text{in}} - \Delta\left(\frac{P}{T}\right)_{\text{in}} \Delta(fv)_{\text{in}} + \frac{\Delta P_{\text{in}} \Delta(T_{\text{in}} f_{\text{in}} v_{\text{in}})}{T_{\text{in}} T^*_{\text{in}}} \\ & - \left(\Delta\left(\frac{\mu}{T}\right)_{\text{out}} - \Delta\left(\frac{\mu}{T}\right)_{\text{in}}\right)^T \Delta(fx)_{\text{in}}\end{aligned}$$

and with some more rearranging we get

$$\begin{aligned}\Delta X^T \Delta J = & \left(\Delta\left(\frac{1}{T}\right)_{\text{out}} - \Delta\left(\frac{1}{T}\right)_{\text{in}}\right) \Delta(fu)_{\text{in}} \\ & + \left(\Delta\left(\frac{P}{T}\right)_{\text{out}} - \Delta\left(\frac{P}{T}\right)_{\text{in}}\right) \Delta(fv)_{\text{in}} \\ & - \left(\Delta\left(\frac{\mu}{T}\right)_{\text{out}} - \Delta\left(\frac{\mu}{T}\right)_{\text{in}}\right)^T \Delta(fx)_{\text{in}} \\ & - \frac{\Delta P_{\text{in}} \Delta(T_{\text{out}} f_{\text{in}} v_{\text{in}})}{T_{\text{out}} T^*_{\text{out}}} + \frac{\Delta P_{\text{in}} \Delta(T_{\text{in}} f_{\text{in}} v_{\text{in}})}{T_{\text{in}} T^*_{\text{in}}}\end{aligned} \tag{D.7}$$

for which inequality (D.5) directly applies. The dissipation in a mass exchange unit is thus positive $\Delta X^T \Delta J \geq 0$ provided the pressure deviations from steady state are negligible.

In this work the distillation column is modeled as a stack of mass exchange units. The stack of mass exchange units have a slightly more complicated dissipation term. For convenience we consider here the two stage distillation column which is composed of a reboiler and a condenser. The dissipation term for the two stage column is

$$\begin{aligned}&\Delta X_1^T \Delta J_1^l + \Delta X_2^T \Delta J_2^v = \left(\Delta\left(\frac{1}{T}\right)_1 - \Delta\left(\frac{1}{T}\right)_2\right) \Delta(L_2 h_2^l) \\ &+ \left(\Delta\left(\frac{1}{T}\right)_2 - \Delta\left(\frac{1}{T}\right)_1\right) \Delta(V_1 h_1^v) - \left(\Delta\left(\frac{\mu}{T}\right)_1 - \Delta\left(\frac{\mu}{T}\right)_2\right)^T \Delta(L_2 x_2) \\ &- \left(\Delta\left(\frac{\mu}{T}\right)_2 - \Delta\left(\frac{\mu}{T}\right)_1\right)^T \Delta(V_1 y_1)\end{aligned} \tag{D.8}$$

where L_2 is the liquid molar flow rate from the condenser to the reboiler and

V_1 is the vapor molar flow rate from the reboiler to the condenser. We again utilize Eq. (C.4) such that

$$\begin{aligned}\Delta X_1^T \Delta J_1^l + \Delta X_2^T \Delta J_2^v = &- \left(\Delta\left(\frac{1}{T_2}\right) - \Delta\left(\frac{1}{T_1}\right)\right)\Delta(L_2 u_2^l) \\ &- \left(\Delta\left(\frac{P_2}{T_2}\right) - \Delta\left(\frac{P_2}{T_1}\right)\right)\Delta(L_2 v_2^l) + \left(\Delta\left(\frac{1}{T_2}\right) - \Delta\left(\frac{1}{T_1}\right)\right)\Delta(V_1 u_1^v) \\ &+ \left(\Delta\left(\frac{P_1}{T_2}\right) - \Delta\left(\frac{P_1}{T_1}\right)\right)\Delta(V_1 v_1^v) + \frac{\Delta P_2 \Delta(T_2 L_2 v_2^l)}{T_2 T_2^*} \\ &- \frac{\Delta P_2 \Delta(T_1 L_2 v_2^l)}{T_1 T_1^*} + \frac{\Delta P_1 \Delta(T_1 V_1 v_1^v)}{T_1 T_1^*} - \frac{\Delta P_1 \Delta(T_2 V_1 v_1^v)}{T_1 T_1^*}.\end{aligned} \tag{D.9}$$

We can see from the expression above that there are cross terms introduced by the stacking of mass exchange units. We thus add by zero to find

$$\begin{aligned}\Delta\left(\frac{P_2}{T_2}\right) - \Delta\left(\frac{P_2}{T_1}\right) &= \left(\Delta\left(\frac{P_2}{T_2}\right) - \Delta\left(\frac{P_1}{T_1}\right)\right) + \left(\Delta\left(\frac{P_1}{T_1}\right) - \Delta\left(\frac{P_2}{T_1}\right)\right) \\ &= \left(\Delta\left(\frac{P_2}{T_2}\right) - \Delta\left(\frac{P_1}{T_1}\right)\right) - \Delta\left(\frac{P_2 - P_1}{T_1}\right)\end{aligned} \tag{D.10}$$

such that, with some rearranging, we get

$$\begin{aligned}\Delta X_1^T \Delta J_1^l + \Delta X_2^T \Delta J_2^v = &\left(\Delta\left(\frac{1}{T_2}\right) - \Delta\left(\frac{1}{T_1}\right)\right)\left(\Delta(V_1 u_1^v) - \Delta(L_2 u_2^l)\right) \\ &+ \left(\Delta\left(\frac{P_2}{T_2}\right) - \Delta\left(\frac{P_1}{T_1}\right)\right)\left(\Delta(V_1 v_1^v) - \Delta(L_2 v_2^l)\right) \\ &- \left(\Delta\left(\frac{\mu_2}{T_2}\right) - \Delta\left(\frac{\mu_1}{T_1}\right)\right)^T \left(\Delta(V_1 y_1) - \Delta(L_2 x_2)\right) \\ &+ \frac{\Delta P_2 \Delta(T_2 L_2 v_2^l)}{T_2 T_2^*} - \frac{\Delta P_2 \Delta(T_1 L_2 v_2^l)}{T_1 T_1^*} + \frac{\Delta P_1 \Delta(T_1 V_1 v_1^v)}{T_1 T_1^*} - \frac{\Delta P_1 \Delta(T_2 V_1 v_1^v)}{T_1 T_1^*} \\ &+ \Delta\left(\frac{P_2 - P_1}{T_1}\right)\Delta(L_2 v_2^l) - \Delta\left(\frac{P_2 - P_1}{T_2}\right)\Delta(V_1 v_1^v).\end{aligned} \tag{D.11}$$

Again we see the net dissipation of the two stage distillation column is positive using inequality (D.3) and (D.4) provided the pressures do not deviate

significantly from steady-state. For the n stage column we get

$$
\begin{aligned}
(\Delta X^T \Delta J)_{tot} = \sum_{i=1}^{n-1} \Bigg\{ & \left(\Delta\left(\frac{1}{T}\right)_{i+1} - \Delta\left(\frac{1}{T}\right)_{i} \right) \left(\Delta(V_i u_i^v) - \Delta(L_{i+1} u_{i+1}^l) \right) \\
& + \left(\Delta\left(\frac{P}{T}\right)_{i+1} - \Delta\left(\frac{P}{T}\right)_{i} \right) \left(\Delta(V_i v_i^v) - \Delta(L_{i+1} v_{i+1}^l) \right) \\
& - \left(\Delta\left(\frac{\mu}{T}\right)_{i+1} - \Delta\left(\frac{\mu}{T}\right)_{i} \right) \left(\Delta(V_i y_i) - \Delta(L_{i+1} x_{i+1}) \right) \\
& + \frac{\Delta P_{i+1} \Delta(T_{i+1} L_{i+1} v_{i+1}^l)}{T_{i+1} T_{i+1}^*} - \frac{\Delta P_{i+1} \Delta(T_i L_{i+1} v_{i+1}^l)}{T_i T_i^*} + \frac{\Delta P_i \Delta(T_i V_i v_i^v)}{T_i T_i^*} \\
& - \frac{\Delta P_i \Delta(T_{i+1} V_i v_i^v)}{T_i T_i^*} + \Delta\left(\frac{P_{i+1} - P_i}{T_i} \right) \Delta(L_{i+1} v_{i+1}^l) - \Delta\left(\frac{P_{i+1} - P_i}{T_{i+1}} \right) \Delta(V_i v_i^v) \Bigg\}.
\end{aligned}
\tag{D.12}
$$

where the pressure in the internal trays are assumed to not deviate from steady-state such that

$$
\begin{aligned}
(\Delta X^T \Delta J)_{tot} = \sum_{i=1}^{n-1} \Bigg\{ & \left(\Delta\left(\frac{1}{T}\right)_{i+1} - \Delta\left(\frac{1}{T}\right)_{i} \right) \left(\Delta(V_i u_i^v) - \Delta(L_{i+1} u_{i+1}^l) \right) \\
& + \left(\Delta\left(\frac{P}{T}\right)_{i+1} - \Delta\left(\frac{P}{T}\right)_{i} \right) \left(\Delta(V_i v_i^v) - \Delta(L_{i+1} v_{i+1}^l) \right) \\
& - \left(\Delta\left(\frac{\mu}{T}\right)_{i+1} - \Delta\left(\frac{\mu}{T}\right)_{i} \right) \left(\Delta(V_i y_i) - \Delta(L_{i+1} x_{i+1}) \right) \Bigg\} \geq 0
\end{aligned}
\tag{D.13}
$$

using inequality (D.3) and (D.4) for each tray.

Appendix E

Contraction Analysis for Process Systems

In this appendix we discuss how the second law of thermodynamics can be utilized to show contraction of non-linear systems. We begin the chapter with contraction analysis which is a method used to show when a dynamical system evolves to a universal trajectory regardless of initial conditions. Properties of the entropy function, specifically that it is concave and homogeneous degree one, lead to contraction conditions that are useful in some cases. We later restrict our view to stability of non-linear systems and show, for an example, that the steady states of distillation columns are stable due to the physical implications of the second law of thermodynamics.

Contraction analysis is a method to determine if different trajectories of a dynamical system will converge together over time. Several researchers have utilized contraction in a non-linear system to analyze stability and design control systems [155–158]. Contraction may also be useful to exploit when using approximation methods such as projective integration. If a dynamical system is strongly contracting then the error introduced by an approximation

will decrease to zero with time.

In contraction analysis, the trajectories are considered differentially close to each such that variational calculus can be deployed. For a general dynamical system given by

$$\dot{z} = f(z,t), \quad z(0) = z_0 \tag{E.1}$$

where $z \in \mathbb{R}^n$ is a vector of the states and t is time, the first variation δz is a measure of displacement between the nearest trajectories corresponding to the system (E.1) with different initial condition. The dynamical system (E.1) is said to be contracting if $\delta z \to 0$ as $t \to \infty$. The rate of change of the first

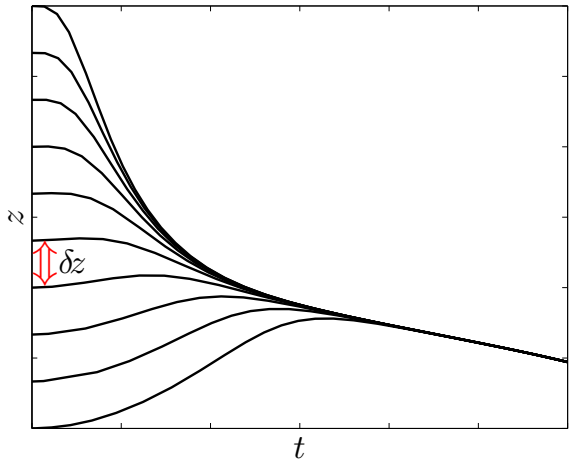

Figure E.1: A contracting dynamical system.

variation δz is calculated by

$$\delta\dot{z} = \frac{\partial f}{\partial z}\delta z \tag{E.2}$$

which is related to the first-order Taylor expansion of the rate of change of the displacement. We now define some metric of the distance between trajectories, such that

$$W = \delta z^T M \delta z > 0 \tag{E.3}$$

where $M(z,t)$ is a (symmetric) positive definite matrix and $W = 0$ if and only

if $\delta z = 0$. The rate of change of the function W is then given by

$$\dot{W} = \delta z^T \left(\frac{\partial f}{\partial z}^T M + M \frac{\partial f}{\partial z} + \dot{M} \right) \delta z. \tag{E.4}$$

The contraction condition due to Lohmiller and Slotine [156] then follows. Given a dynamical system (E.1) for any trajectory, which start in a ball of constant radius according to the metric $M(z,t)$, if the function W is uniformly decreasing with time within the ball then

$$\left(\frac{\partial f}{\partial z}^T M + M \frac{\partial f}{\partial z} + \dot{M} \right) \leq -\epsilon M \tag{E.5}$$

where ϵ is a strictly positive scalar and the dynamical system (E.1) will exponentially converge to a single trajectory. Furthermore, Lohmiller and Slotine [156] made use of a converse theorem to show that this condition is necessary and sufficient for exponential convergence of all trajectories in the ball measured by $\delta z^T M \delta z$.

The complications in this analysis arises with identification of matrix $M(z,t)$ which must simultaneously satisfy conditions (E.3) and (E.5). The identity matrix has been shown to be useful in a few cases [156–158], but its use weakens the convergence conditions to be only sufficient. Another option is to use the thermodynamic entropy of the dynamical system as proposed by Aggarwal and Ydstie [136].

We express the entropy in the form

$$S = w^T z \tag{E.6}$$

where w is vector of potentials and z is a vector of inventories such that

$$\begin{aligned} w &= \left[\frac{1}{T}, \frac{P}{T}, -\frac{\mu_1}{T}, \cdots, -\frac{\mu_{n_c}}{T}\right]^T \\ z &= [U, V, N_1, \cdots, N_{n_c}]^T \end{aligned} \tag{E.7}$$

where T is the temperature, P is the pressure, μ_k is the chemical potential of component k, U is the internal energy, V is the volume, N_k is the number of moles of component k, and n_c is the total number of components. The important properties of the entropy that we would like to exploit include that it is homogenous degree one and concave in z [138]. The homogeneous degree one property, for instance, yields the Gibbs-Duhem equation [139]

$$dw^T z = 0 \tag{E.8}$$

which allows us to define the potentials directly from the entropy, i.e. $dS = w^T dz$ or

$$w = \frac{\partial S}{\partial z}. \tag{E.9}$$

The first variation of the potentials is then given by

$$\delta w = \frac{\partial w}{\partial z}\delta z \tag{E.10}$$

where $\partial w/\partial z = \partial^2 S/\partial z^2$ is the Hessian of the entropy. It then follows that the quantity

$$\Psi = -\delta w^T \delta z = -\delta z^T \frac{\partial^2 S}{\partial z^2}\delta z \tag{E.11}$$

is non-negative. Although entropy in concave, its concavity is imparted by a concave hull over states that are physically inaccessible, which causes the Hessian to be negative semi-definite [136]. We can therefore use Ψ in a con-

traction analysis provided there are sufficient controls to meet the properties detailed above.

The homogeneous degree one property of the entropy can also be exploited in the analysis. The potential variables are homogeneous degree zero $w(\lambda z) = w(z)$ which follows since they are calculated using the gradient of the entropy which is homogeneous degree one. The potentials $w(z)$ are known as intrinsic variables and are independent of the size of the system. For a homogeneous degree zero function we have the property

$$\frac{\partial w(\lambda z)}{\partial(\lambda z)} = \lambda^{-1}\frac{\partial w(z)}{\partial z}. \tag{E.12}$$

It then follows that

$$\delta w(\lambda z, \lambda\delta z) = \frac{\partial w(\lambda z)}{\partial(\lambda z)}\lambda\delta z = \frac{\partial w(z)}{\partial z}\delta z \tag{E.13}$$

such that δw is homogeneous degree zero in z and δz. Euler's theorem of homogeneous functions can then be used to show

$$\frac{\partial \delta w}{\partial z}z + \frac{\partial \delta w}{\partial \delta z}\delta z = 0. \tag{E.14}$$

Recalling the definition of δw from Eq. (E.10) we then get

$$\frac{\partial}{\partial z}\left(\frac{\partial w}{\partial z}\delta z\right)z + \frac{\partial w}{\partial z}\delta z = 0 \tag{E.15}$$

where differentiation of $\partial w/\partial z$ with respect to z results in a rank 3 tensor. To avoid introducing tensor notation, we define the matrices

$$P = \frac{\partial}{\partial z}\left(\frac{\partial w}{\partial z}\delta z\right), \quad Q = \frac{\partial w}{\partial z} \tag{E.16}$$

where $P(z, \delta z)$ and $Q(z)$.

We then differentiate Eq. (E.15) with respect to time to show

$$\dot{P}z + Pf(z,t) + \dot{Q}\delta z + Q\frac{\partial f}{\partial z}\delta z = 0 \tag{E.17}$$

using Eq. (E.1) and Eq. (E.2). We now pre-multiply by δz^T to find the relation

$$\delta z^T \dot{P} z + \delta z^T P f(z,t) + \delta z^T \dot{Q}\delta z + \delta z^T Q\frac{\partial f}{\partial z}\delta z = 0. \tag{E.18}$$

The inner products produce scalars which are symmetric such that

$$\begin{aligned}\frac{1}{2}\delta z^T(\dot{P}+\dot{P}^T)z + \frac{1}{2}\delta z^T(P+P^T)f(z,t) \\ + \delta z^T\dot{Q}\delta z + \frac{1}{2}\delta z^T\left(Q\frac{\partial f}{\partial z} + \frac{\partial f}{\partial z}^T Q\right)\delta z = 0.\end{aligned} \tag{E.19}$$

At this point we can see how the entropy can be used in a contraction analysis. A contracting system obeys the necessary and sufficient conditions outlined in Eq. (E.3) – (E.5). In some cases it may be possible to infer the necessary signs of the matrices from Eq. (E.19). However, in order to do so, the sign of the third derivatives of the entropy with respect to the states z are needed such that the sign of the matrix P can be inferred. This would typically require the entropy function to be known in closed form. The relation shown above is derived in a similar manner as the Gibbs-Duhem equation from classical thermodynamics [139].

Bibliography

[1] Ramkumar Karuppiah and Ignacio E Grossmann, "Global optimization for the synthesis of integrated water systems in chemical processes", *Computers & Chemical Engineering* **30**(4), pp. 650–673 (2006).

[2] C. A. Floudas, J. L. Klepeis, and P. M. Pardalos, "Global optimization approaches in protein folding and peptide docking", *DIMACS Series in Discrete Mathematics and Theoretical Computer Science* **47**, pp. 141 – 171 (1999).

[3] Nilanjan Adhya, Mohit Tawarmalani, and Nikolaos V Sahinidis, "A lagrangian approach to the pooling problem", *Industrial & Engineering Chemistry Research* **38**(5), pp. 1956–1972 (1999).

[4] Jeremy G Van Antwerp, Richard D Braatz, and Nikolaos V Sahinidis, "Globally optimal robust process control", *Journal of Process Control* **9**(5), pp. 375–383 (1999).

[5] Ken McKinnon and Marcel Mongeau, "A generic global optimization algorithm for the chemical and phase equilibrium problem", *Journal of Global Optimization* **12**(4), pp. 325–351 (1998).

[6] C. A. Floudas, I. G. Akrotirianakis, S. Caratzoulas, C. A. Meyer, and J. Kallrath, "Global optimization in the 21st century: Advances and

challenges", *Computers & Chemical Engineering* **29**(6), pp. 1185–1202 (2005).

[7] C.S. Adjiman, S. Dallwig, C.A. Floudas, and A. Neumaier, "A global optimization method, [alpha]BB, for general twice-differentiable constrained nlps–i. theoretical advances", *Computers & Chemical Engineering* **22**(9), pp. 1137–1158 (1998).

[8] M. Tawarmalani and N. V. Sahinidis, "A polyhedral branch-and-cut approach to global optimization", *Mathematical Programming* **103**, pp. 225–249 (2005).

[9] Mohit Tawarmalani and Nikolaos V Sahinidis, *Convexification and global optimization in continuous and mixed-integer nonlinear programming: theory, algorithms, software, and applications* volume 65, Springer (2002).

[10] Nikolaos V. Sahinidis, *BARON 11.4.0: Global Optimization of Mixed-Integer Nonlinear Programs,* User's Manual (2012).

[11] Youdong Lin and Linus Schrage, "The global solver in the LINDO API", *Optimization Methods & Software* **24**(4-5), pp. 657–668 (2009).

[12] G.P. McCormick, "Computability of global solutions to factorable nonconvex programs: Part I convex underestimating problems", *Mathematical programming* **10**(1), pp. 147–175 (1976).

[13] Faiz A Al-Khayyal and James E Falk, "Jointly constrained biconvex programming", *Mathematics of Operations Research* **8**(2), pp. 273–286 (1983).

[14] Ignacio Quesada and Ignacio E. Grossmann, "A global optimization algorithm for linear fractional and bilinear programs", *Journal of Global Optimization* **6**(1), pp. 39–76 (1995).

[15] Mohit Tawarmalani and NikolaosV. Sahinidis, "Semidefinite relaxations of fractional programs via novel convexification techniques", *Journal of Global Optimization* **20**, pp. 133–154 (2001).

[16] Edward M.B. Smith and Constantinos C. Pantelides, "A symbolic reformulation/spatial branch-and-bound algorithm for the global optimisation of nonconvex MINLPs", *Computers & Chemical Engineering* **23**(4), pp. 457–478 (1999).

[17] Hanif D. Sherali and Cihan H. Tuncbilek, "A global optimization algorithm for polynomial programming problems using reformulation-linearization technique", *Journal of Global Optimization* **2**, pp. 101 – 112 (1992).

[18] Sigurd Skogestad, "Dynamics and control of distillation columns: A tutorial introduction", *Chemical Engineering Research and Design* **75**(6), pp. 539–562 (1997).

[19] Howard H. Rosenbrock, "Theorem of dynamic conversion for distillation", *Transactions of the Institution of Chemical Engineers* **38**, pp. 279–287 (1960).

[20] Howard H. Rosenbrock, "Lyapunov function with applications to some nonlinear physical problems", *Automatica* **1**, pp. 31–53 (1962).

[21] J.D. Brouwer, D.Roald .and Jansen, "Dynamic optimization of waterflooding with smart wells using optimal control theory", *SPE journal* **9**(04), pp. 391–402 (2004).

[22] Jan-Dirk Jansen, Okko H Bosgra, and Paul MJ Van den Hof, "Model-based control of multiphase flow in subsurface oil reservoirs", *Journal of Process Control* **18**(9), pp. 846–855 (2008).

[23] Geir Nævdal, D Roald Brouwer, and Jan-Dirk Jansen, "Waterflooding using closed-loop control", *Computational Geosciences* **10**(1), pp. 37–60 (2006).

[24] Roland Probst and Benjamin Shapiro, "Three-dimensional electrokinetic tweezing: device design, modeling, and control algorithms", *Journal of Micromechanics and Microengineering* **21**(2), pp. 027004 (2011).

[25] FJ Cao, M Feito, and H Touchette, "Information and flux in a feedback controlled brownian ratchet", *Physica A: Statistical Mechanics and its Applications* **388**(2), pp. 113–119 (2009).

[26] M Feito and FJ Cao, "Time-delayed feedback control of a flashing ratchet", *Physical Review E* **76**(6), pp. 061113 (2007).

[27] Chi-Tsong Chen, *Linear system theory and design*, Oxford University Press, Inc. (1995).

[28] Hassan K Khalil, *Nonlinear systems* volume 3, Prentice hall Upper Saddle River (2002).

[29] Shane T. Grosser, Jeffrey M. Savard, and James W. Schneider, "Identification of PCR products using PNA amphiphiles in micellar electrokinetic chromatography", *Analytical Chemistry* **79**, pp. 9513 – 9519 (2007).

[30] Jeffrey M. Savard, Shane T. Grosser, and James W. Schneider, "Length-dependent DNA separations using multiple end-attached peptide nu-

cleic acid amphiphiles in micellar electrokinetic chromatography", *Electrophoresis* **29**, pp. 2779 – 2789 (2008).

[31] John. M. Butler, *Forensic DNA Typing: Biology and Technology behind STR markers*, Academic Press, San Diego, CA, USA (2001).

[32] Yining Shi, "DNA sequencing and multiplex STR analysis on plastic microfluidic devices", *Electrophoresis* **27**, pp. 3703 – 3711 (2006).

[33] Ying Wu, Minna Nystrm-Lahti, Jan Osinga, Maaike W. G. Looman, Pivi Peltomki, Lauri A. Aaltonen, Albert de la Chapelle, Robert M. W. Hofstra, and Charles H. C. M. Buys, "MSH2 and MLH1 mutations in sporadic replication error-positive colorectal carcinoma as assessed by two-dimensional DNA electrophoresis", *Genes, Chromosomes and Cancer* **18**(4), pp. 269–278 (1997).

[34] Mario F. Fraga, Esther Uriol, L. Borja Diego, Mara Berdasco, Manel Esteller, Mara Jess Caal, and Roberto Rodrguez, "High-performance capillary electrophoretic method for the quantification of 5-methyl 2'-deoxycytidine in genomic dna: Application to plant, animal and human cancer tissues", *Electrophoresis* **23**(11), pp. 1677–1681 (2002).

[35] Jennifer C. Albrecht, Akira Kotani, Jennifer S. Lin, Steven A. Soper, and Annelise E. Barron, "Simultaneous detection of 19 K-*ras* mutations by free-solution conjugate electrophoresis of ligase detection reaction products on glass microchips", *Electrophoresis* **00**, pp. 1 – 8 (2013).

[36] F. Sanger, S. Nicklen, and A. R. Coulson, "DNA sequencing with chain-terminating inhibitors", *Proceedings of the National Academy of Sciences* **74**(12), pp. 5463–5467 (1977).

[37] Christopher P. Fredlake, Daniel G. Hert, Cheuk Wai Kan, Thomas N. Chiesl, Brian E. Root, Ryan E. Forster, and Annelise E. Barron, "Ultrafast DNA sequencing on a microchip by a hybrid separation mechanism that gives 600 bases in 6.5 minutes", *Proceedings of the National Academy of Sciences* **105** (2008).

[38] Jennifer C. Albrecht, Jennifer S. Lin, and Annelise E. Barron, "A 265-base DNA sequencing read by capillary electrophoresis with no separation matrix", *Analytical Chemistry* **80**, pp. 509 – 515 (2011).

[39] H. Ren, A.E. Karger, F. Oaks, S. Menchen, G.W. Slater, and G. Drouin, "Separating DNA sequencing fragments without a sieving matrix", *Electrophoresis* **20**(12), pp. 2501–2509 (1999).

[40] R.J. Meagher, J. Won, J.A. Coyne, J. Li, and A.E. Barron, "Sequencing of dna by free-solution capillary electrophoresis using a genetically engineered protein polymer drag-tag", *Analytical Chemistry* **80**, pp. 2842 – 2848 (2008).

[41] Gary W Slater and Jaan Noolandi, "New biased-reptation model for charged polymers", *Physical review letters* **55**(15), pp. 1579 (1985).

[42] Jaan Noolandi, Gary W Slater, Ha Lim, and Jean L Viovy, "Generalized tube model of biased reptation for gel electrophoresis of dna", *Science* **243**(4897), pp. 1456–1458 (1989).

[43] David C Schwartz and Charles R Cantor, "Separation of yeast chromosome-sized DNAs by pulsed field gradient gel electrophoresis", *Cell* **37**(1), pp. 67–75 (1984).

[44] Thomas AJ Duke, Robert H Austin, Edward C Cox, and Shirley S Chan,

"Pulsed-field electrophoresis in microlithographic arrays", *Electrophoresis* **17**(6), pp. 1075–1079 (1996).

[45] Jan Sudor and Milos V Novotny, "Separation of large DNA fragments by capillary electrophoresis under pulsed-field conditions", *Analytical chemistry* **66**(15), pp. 2446–2450 (1994).

[46] R Anand, "Pulsed field gel electrophoresis: a technique for fractionating large dna molecules", *Trends in Genetics* **2**, pp. 278–283 (1986).

[47] Jongyoon Han, SW Turner, and Harold G. Craighead, "Entropic trapping and escape of long DNA molecules at submicron size constriction", *Physical review letters* **83**(8), pp. 1688 (1999).

[48] Jongyoon Han and Harold G. Craighead, "Separation of long DNA molecules in a microfabricated entropic trap array", *Science* **288**(5468), pp. 1026–1029 (2000).

[49] Jongyoon Han and Harold G. Craighead, "Characterization and optimization of an Entropic Trap for DNA separation", *Analytical Chemistry* **74**, pp. 394 – 401 (2002).

[50] Jianping Fu, Juhwan Yoo, and Jongyoon Han, "Molecular sieving in periodic free-energy landscapes created by patterned nanofilter arrays", *Physical review letters* **97**(1), pp. 018103 (2006).

[51] Jianping Fu, Reto B Schoch, Anna L Stevens, Steven R Tannenbaum, and Jongyoon Han, "A patterned anisotropic nanofluidic sieving structure for continuous-flow separation of dna and proteins", *Nature nanotechnology* **2**(2), pp. 121–128 (2007).

[52] Jongyoon Han, Jianping Fu, and Reto B Schoch, "Molecular sieving using nanofilters: past, present and future", *Lab on a Chip* **8**(1), pp. 23–33 (2008).

[53] Walter Reisner, Niels B Larsen, Henrik Flyvbjerg, Jonas O Tegenfeldt, and Anders Kristensen, "Directed self-organization of single DNA molecules in a nanoslit via embedded nanopit arrays", *Proceedings of the National Academy of Sciences* **106**(1), pp. 79–84 (2009).

[54] Yu Zhang, Juan J de Pablo, and Michael D Graham, "An immersed boundary method for Brownian dynamics simulation of polymers in complex geometries: Application to DNA flowing through a nanoslit with embedded nanopits", *The Journal of Chemical Physics* **136**(1), pp. 014901 (2012).

[55] Patrick S Doyle, Jérôme Bibette, Aurélien Bancaud, and Jean-Louis Viovy, "Self-assembled magnetic matrices for DNA separation chips", *Science* **295**(5563), pp. 2237–2237 (2002).

[56] Nicolas Minc, Claus Fütterer, Kevin D. Dorfman, Aurélien Bancuad, Charlie Gosse, Cécile Goubault, and Jean-Louis Viovy, "Quantitative microfluidic separation of DNA in self-assembled magnetic matrixes", *Analytical Chemistry* **76**, pp. 3770 – 3776 (2004).

[57] Noritada Kaji, Yojiro Tezuka, Yuzuru Takamura, Masanori Ueda, Takahiro Nishimoto, Hiroaki Nakanishi, Yasuhiro Horiike, and Yoshinobu Baba, "Separation of long DNA molecules by quartz nanopillar chips under a direct current electric field", *Analytical chemistry* **76**(1), pp. 15–22 (2004).

[58] Jia Ou, Jaeseol Cho, Daniel W Olson, and Kevin D Dorfman, "DNA

electrophoresis in a sparse ordered post array", *Physical Review E* **79**(6), pp. 061904 (2009).

[59] J. M. Deutsch, "Theoretical studies of DNA during gel electrophoresis", *Science* **240**, pp. 922 – 924 (1988).

[60] Ju Min Kim and Patrick S Doyle, "Design and numerical simulation of a DNA electrophoretic stretching device", *Lab on a Chip* **7**(2), pp. 213–225 (2007).

[61] Prateek D Patel and Eric SG Shaqfeh, "A computational study of DNA separations in sparse disordered and periodic arrays of posts", *The Journal of chemical physics* **118**(6), pp. 2941–2951 (2003).

[62] Daniel W. Olson, Sarit Dutta, Nabil Laachi, Mingwei Tian, and Kevin D. Dorfman, "Continuous-time random walk models of DNA electrophoresis in a post array: Part II Mobility and sources of band broadening", *Electrophoresis* **32**, pp. 581 – 587 (2011).

[63] C. William Gear and Ioannis G Kevrekidis, "Projective methods for stiff differential equations: problems with gaps in their eigenvalue spectrum", *SIAM Journal on Scientific Computing* **24**(4), pp. 1091–1106 (2003).

[64] Ioannis G Kevrekidis, C William Gear, James M Hyman, Panagiotis G Kevrekidid, Olof Runborg, and Constantinos Theodoropoulos, "Equation-free, coarse-grained multiscale computation: Enabling mocroscopic simulators to perform system-level analysis", *Communications in Mathematical Sciences* **1**(4), pp. 715–762 (2003).

[65] Ioannis G Kevrekidis and Giovanni Samaey, "Equation-free multiscale computation: Algorithms and applications", *Annual review of physical chemistry* **60**, pp. 321–344 (2009).

[66] Antonio A Alonso and B Erik Ydstie, "Stabilization of distributed systems using irreversible thermodynamics", *Automatica* **37**(11), pp. 1739–1755 (2001).

[67] Jean-Louis Viovy, "Electrophoresis of DNA and other polyelectrolytes: Physical mechanisms", *Reviews of Modern Physics* **72**, pp. 813–872 (2000).

[68] Claude Desruisseaux, Didier Long, Guy Drouin, and Gary W. Slater, "Electrophoresis of composite molecular objects. 1. relation between friction, charge and ionic strength in free solution", *Macromolecules* **34**, pp. 44 – 52 (2001).

[69] Stephen B. Istivan, *Gel-free Separations of DNA via Transient Attachment to Surfactant Micelles*, PhD thesis Carnegie Mellon University Pittsburgh, PA 15213 (2012).

[70] Nancy C. Stellwagen, Cecilia Gelfi, and Pier Giorgio Righetti, "The free solution mobility of DNA", *Biopolymers* **42**(6), pp. 687–703 (1997).

[71] Paul D. Grossman and Joel C. Colburn, *Capillary Electrophoresis: Theory and Practice*, Academic Press (1992).

[72] John.C. Giddings, *Unified Separation Science*, Wiley (1991).

[73] Kevin D. Dorfman, Scott B. King, Daniel W. Olson, Joel D. P. Tree, and Douglass R. Tree, "Beyond gel electrophoresis: Microfluidic separations, fluorescence, burst analysis, and DNA stretching", *Chemical Reviews* **doi: 10.1021** (2012).

[74] Prince E. Rouse, "A theory of the linear viscoelastic properties of dilute

solutions of coiling polymers", *The Journal of Chemical Physics* **21**, pp. 1272–1281 (1953).

[75] Bruno H. Zimm, "Dynamics of polymer molecules in dilute solution: viscoelasticity, flow birefringence and dielectric loss", *The Journal of Chemical Physics* **24**, pp. 269–279 (1956).

[76] Laurette C McCormick and Gary W Slater, "A theoretical study of the possible use of electroosmotic flow to extend the read length of DNA sequencing by end-labeled free solution electrophoresis", *Electrophoresis* **27**(9), pp. 1693–1701 (2006).

[77] Geoffrey I. Taylor, "Dispersion of soluble matter in solvent flowing slowly through a tube", *Proceedings of the Royal Society of London. A* **219**, pp. 186–203 (1953).

[78] Geoffrey I. Taylor, "The dispersion of matter in turbulent flow through a pipe", *Proceedings of the Royal Society of London. A* **223**, pp. 446–468 (1954).

[79] Geoffrey I. Taylor, "Conditions under which dispersion of a solute in a stream of solvent can be used to measure molecular diffusion", *Proceedings of the Royal Society of London. A* **225**, pp. 473–477 (1954).

[80] Rutherford Aris, "On the dispersion of a solute in a fluid flowing through a tube", *Proceedings of the Royal Society of London. A* **235**, pp. 67–77 (1956).

[81] J. H. Knox and I. H. Grant, "Miniaturisation in pressure and electroendosmotically driven liquid chromatography: Some theoretical considerations", *Chromatographia* **24**, pp. 135 – 147 (1987).

[82] J. H. Knox, "Thermal effects and band spreading in capillary electro-separation", *Chromatographia* **26**, pp. 329 – 337 (1988).

[83] Anton J. Pfeiffer, Tamal Mukherjee, and Steinar Hauan, "Design and optimization of compact microscale electrophoretic separation systems", *Industrial & Engineering Chemistry Research* **43**, pp. 3539 – 3553 (2004).

[84] Stewart K Griffiths and Robert H Nilson, "Band spreading in two-dimensional microchannel turns for electrokinetic species transport", *Analytical chemistry* **72**(21), pp. 5473–5482 (2000).

[85] J.I. Molho, A.E. Herr, B.P. Mosier, J.G. Santiago, T.W. Kenny, R.A. Brennen, G.B. Gordon, and B. Mohammadi, "Optimization of turn geometries for microchip electrophoresis", *Analytical Chemistry* **73**(6), pp. 1350–1360 (2001).

[86] Yi Wang, Qiao Lin, and Tamal Mukherjee, "System-oriented dispersion models of general-shaped electrophoresis microchannels", *Lab on a Chip* **4**, pp. 453 – 463 (2004).

[87] Christopher T. Culbertson, Stephen C. Jacobson, and J. Michael Ramsey, "Microchip devices for high-efficiency separations", *Analytical Chemistry* **72**(23), pp. 5814–5819 (2000).

[88] Wei Wei and Edward S Yeung, "DNA capillary electrophoresis in entangled dynamic polymers of surfactant molecules", *Analytical chemistry* **73**(8), pp. 1776–1783 (2001).

[89] Georges F Carle, Mark Frank, and Maynard V Olson, "Electrophoretic separations of large DNA molecules by periodic inversion of the electric field", *Science* **232**(4746), pp. 65–68 (1986).

[90] Zhenqing Li, Xiaoming Dou, Yi Ni, and Yoshinori Yamaguchi, "Separation of long DNA fragments by inversion field capillary electrophoresis", *Analytical and Bioanalytical Chemistry* **401**(5), pp. 1661–1667 (2011).

[91] Yongseong Kim and Michael D Morris, "Pulsed field capillary electrophoresis of multikilobase length nucleic acids in dilute methyl cellulose solutions", *Analytical chemistry* **66**(19), pp. 3081–3085 (1994).

[92] K. L. Sebastian and Alok K.R. Paul, "Kramers problem for a polymer in a double well", *Physical Review E* **62**(1), pp. 927–939 (2000).

[93] Takahiro Sakaue, "DNA electrophoresis in designed channels", *The European Physical Journal E* **19**(4), pp. 477–487 (2006).

[94] Frédéric Tessier, Josée Labrie, and Gary W. Slater, "Electrophoretic separation of long polyelectrolytes in submolecular-size constricitons: A Monte Carlo study", *Macromolecules* **35**, pp. 4791 – 4800 (2002).

[95] Zhong Chen and Fernando A Escobedo, "Simulation of chain-length partitioning in a microfabricated channel via entropic trapping", *Molecular Simulation* **29**(6-7), pp. 417–425 (2003).

[96] Martin Streek, Friederike Schmid, Thanh Tu Duong, and Alexandra Ros, "Mechanisms of DNA separation in entropic trap arrays: a Brownian dynamics simulation", *Journal of biotechnology* **112**(1), pp. 79–89 (2004).

[97] Ajay S. Panwar and Satish Kumar, "Time scales in polymer electrophoresis through narrow constrictions: A Brownian dynamics study", *Macromolecules* **39**, pp. 1279 – 1289 (2006).

[98] Yong Min Lee and Yong Lak Joo, "Brownian dynamics simulations of polyelectrolyte molecules traveling through an entropic trap array during electrophoresis", *The Journal of Chemical Physics* **127**(12), pp. 124902 (2007).

[99] Joe S Hur, Eric SG Shaqfeh, and Ronald G Larson, "Brownian dynamics simulations of single DNA molecules in shear flow", *Journal of Rheology* **44**(4), pp. 713–742 (2000).

[100] Patrick S. Doyle, Benoit Ladoux, and Jean-Louis Viovy, "Dynamics of a tethered polymer in shear flow", *Physical Review Letters* **84**, pp. 4769–4772 (2000).

[101] Jaeseol Cho and Kevin D. Dorfman, "Brownian dynamics simulations of electrophoretic DNA separations in a sparse ordered post array", *Jounal of Chromatography A* **1217**, pp. 5522 – 5528 (2010).

[102] Ju Min Kim and Patrick S Doyle, "Brownian dynamics simulations of a DNA molecule colliding with a small cylindrical post", *Macromolecules* **40**(25), pp. 9151–9163 (2007).

[103] Ju Min Kim and Patrick S Doyle, "A Brownian dynamics-finite element method for simulating DNA electrophoresis in nonhomogeneous electric fields", *The Journal of chemical physics* **125**(7), pp. 074906 (2006).

[104] YL Chen, MD Graham, JJ de Pablo, GC Randall, M Gupta, and PS Doyle, "Conformation and dynamics of single DNA molecules in parallel-plate slit microchannels", *Physical Review E* **70**, pp. 060901 (2004).

[105] Richard M Jendrejack, David C Schwartz, Michael D Graham, and Juan J de Pablo, "Effect of confinement on DNA dynamics in microflu-

idic devices", *The Journal of chemical physics* **119**(2), pp. 1165–1173 (2003).

[106] Murugappan Muthukumar and CY Kong, "Simulation of polymer translocation through protein channels", *Proceedings of the National Academy of Sciences* **103**(14), pp. 5273–5278 (2006).

[107] Chung Y Kong and Murugappan Muthukumar, "Modeling of polynucleotide translocation through protein pores and nanotubes", *Electrophoresis* **23**(16), pp. 2697–2703 (2002).

[108] Manish Chopra and Ronald G Larson, "Brownian dynamics simulations of isolated polymer molecules in shear flow near adsorbing and nonadsorbing surfaces", *Journal of Rheology* **46**(4), pp. 831–862 (2002).

[109] Jing Tang, Stephen L Levy, Daniel W Trahan, Jeremy J Jones, Harold G Craighead, and Patrick S Doyle, "Revisiting the conformation and dynamics of dna in slitlike confinement", *Macromolecules* **43**(17), pp. 7368–7377 (2010).

[110] Marshall Fixman, "Dynamics of polymer chains", *Journal of Chemical Physics* **42**(11), pp. 3831 – 3837 (1965).

[111] Anthony Balducci, Pan Mao, Jongyoon Han, and Patrick S Doyle, "Double-stranded DNA diffusion in slitlike nanochannels", *Macromolecules* **39**(18), pp. 6273–6281 (2006).

[112] Hans Christian Öttinger, *Stochastic processes in polymeric fluids: tools and examples for developing simulation algorithms*, Springer Berlin (1996).

[113] John F Marko and Eric D Siggia, "Stretching DNA", *Macromolecules* **28**(26), pp. 8759–8770 (1995).

[114] Thomas T Perkins, Douglas E Smith, Ronald G Larson, and Steven Chu, "Stretching of a single tethered polymer in a uniform flow", *Science* , pp. 83–83 (1995).

[115] Patrick T Underhill and Patrick S Doyle, "Alternative spring force law for bead-spring chain models of the worm-like chain", *Journal of Rheology (1978-present)* **50**(4), pp. 513–529 (2006).

[116] Richard M Jendrejack, David C Schwartz, Juan J de Pablo, and Michael D Graham, "Shear-induced migration in flowing polymer solutions: Simulation of long-chain dna in microchannels", *The Journal of chemical physics* **120**(5), pp. 2513–2529 (2004).

[117] DM Heyes and JR Melrose, "Brownian dynamics simulations of model hard-sphere suspensions", *Journal of non-newtonian fluid mechanics* **46**(1), pp. 1–28 (1993).

[118] Madan Somasi, Bamin Khomami, Nathanael J Woo, Joe S Hur, and Eric SG Shaqfeh, "Brownian dynamics simulations of bead-rod and bead-spring chains: numerical algorithms and coarse-graining issues", *Journal of non-newtonian fluid mechanics* **108**(1), pp. 227–255 (2002).

[119] Chiu Tai Andrew Wong and Murugappan Muthukumar, "Scaling theory of polymer translocation into confined regions", *Biophysical journal* **95**(8), pp. 3619–3627 (2008).

[120] Armand Ajdari and Jacques Prost, "Free-flow electrophoresis with trapping by a transverse inhomogeneous field.", *Proceedings of the National Academy of Sciences* **88**(10), pp. 4468–4471 (1991).

[121] Nishith Vora and Prodromos Daoutidis, "Nonlinear model reduction of chemical reaction systems", *AIChE Journal* **47**(10), pp. 2320–2332 (2001).

[122] Michael Baldea and Prodromos Daoutidis, "Control of integrated process networksa multi-time scale perspective", *Computers & chemical engineering* **31**(5), pp. 426–444 (2007).

[123] V. R. Saksena, J. O'reilly, and P. V. Kokotovic, "Singular perturbations and time-scale methods in control theory: survey 1976–1983", *Automatica* **20**(3), pp. 273–293 (1984).

[124] Constantinos I Siettos, Michael D Graham, and Ioannis G Kevrekidis, "Coarse Brownian dynamics for nematic liquid crystals: Bifurcation, projective integration, and control via stochastic simulation", *Journal of Chemical Physics* **118**(22), pp. 10149–10156 (2003).

[125] R Rico-Martínez, C. William Gear, and Ioannis G Kevrekidis, "Coarse projective kMC integration: Forward/reverse initial and boundary value problems", *Journal of Computational Physics* **196**(2), pp. 474–489 (2004).

[126] B. Erik Ydstie, Lester S. Kershenbaum, and Roger W. H. Sargent, "Theory and application of an extended horizon self-tuning controller", *AICHE journal* **31**(11), pp. 1771–1780 (1985).

[127] B. Erik Ydstie, A. H. Kemna, and L. K. Liu, "Multivariable extended-horizon adaptive control", *Computers & Chemical Engineering* **12**(7), pp. 733–743 (1988).

[128] Richard M Jendrejack, Juan J de Pablo, and Michael D Graham, "Stochastic simulations of DNA in flow: Dynamics and the effects of

hydrodynamic interactions", *The Journal of chemical physics* **116**, pp. 7752 (2002).

[129] Martijn Handels, Maarten J. Zandvliet, D. Roald Brouwer, and Jan-Dirk Jansen, "Adjoint-based well-placement optimization under production constraints", *SPE Journal* **13**(04), pp. 392–399 (2008).

[130] Trevor Hastie, Robert Tibshirani, and Jerome Friedman, *The elements of statistical learning*, Springer (2009).

[131] Ake Björck, *Numerical methods for least squares problems*, Siam (1996).

[132] Behnam Jafarpour and Dennis B McLaughlin, "History matching with an ensemble kalman filter and discrete cosine parameterization", *Computational Geosciences* **12**(2), pp. 227–244 (2008).

[133] Behnam Jafarpour, Dennis B McLaughlin, et al., "Reservoir characterization with the discrete cosine transform", *SPE Journal* **14**(01), pp. 182–201 (2009).

[134] Andreas Acrivos and Neal R Amundson, "Applications of matrix mathematics to chemical engineering problems", *Industrial & Engineering Chemistry* **47**(8), pp. 1533–1541 (1955).

[135] M. F. Doherty and J. D. Perkins, "On the dynamics of distillation processes–IV Uniqueness and stability of the steady state in homogeneous continuous distillations", *Chemical Engineering Science* **37**(3), pp. 381 – 392 (1982).

[136] Mohit Aggarwal and B Erik Ydstie, "Note on flash and distillation systems", *AIChE Journal* **59**(9), pp. 3322–3332 (2013).

[137] P Rouchon and Y Creff, "Geometry of the flash dynamics", *Chemical Engineering Science* **48**(18), pp. 3141–3147 (1993).

[138] Kendell R Jillson and B Erik Ydstie, "Process networks with decentralized inventory and flow control", *Journal of Process Control* **17**(5), pp. 399–413 (2007).

[139] Donald G. Miller, "Duhem and the Gibbs-Duhem equation", *Journal of Chemical Education* **40**, pp. 648 – 649 (1963).

[140] Zhaojia Lin, "Modeling and simulation of equilibrium staged systems", Master's thesis Carnegie Mellon University Pittsburgh, PA 15213 (2009).

[141] Arvind U Raghunathan, M Soledad Diaz, and Lorenz T Biegler, "An MPEC formulation for dynamic optimization of distillation operations", *Computers & chemical engineering* **28**(10), pp. 2037–2052 (2004).

[142] B. Erik Ydstie, Zhaojia Lin, and Max A. Fahrenkopf, "Stability of the multi-component flash", *To be published* (2014).

[143] Fernando Tiscareño, Alejandro Gómez, Arturo Jiménez, and Rafael Chávez, "Multiplicity of the solutions of the flash equations", *Chemical engineering science* **53**(4), pp. 671–677 (1998).

[144] Miguel Vaca, Arturo Jimnez, and Rosendo Monroy-Loperena, "On the multiple solutions of the flash equations", *Chemical Engineering Science* **61**(12), pp. 3850 – 3857 (2006).

[145] Apurva P Samudra and Nikolaos V Sahinidis, "Optimization-based framework for computer-aided molecular design", *AIChE Journal* **59**(10), pp. 3686–3701 (2013).

[146] Srinivas Nageswaran Moorkanikkara and Daniel Blankschtein, "New theoretical framework for designing nonionic surfactant mixtures that exhibit a desired adsorption kinetics behavior", *Langmuir* **26**(24), pp. 18728–18733 (2010).

[147] Anat Shiloach and Daniel Blankschtein, "Predicting micellar solution properties of binary surfactant mixtures", *Langmuir* **14**(7), pp. 1618–1636 (1998).

[148] Patrick S Doyle, Eric SG Shaqfeh, and Alice P Gast, "Dynamic simulation of freely draining flexible polymers in steady linear flows", *Journal of Fluid Mechanics* **334**, pp. 251–291 (1997).

[149] John R Fanchi, *Principles of applied reservoir simulation*, Gulf Professional Publishing (2005).

[150] MR Carlson, *Practical reservoir simulation: using, assessing, and developing results*, PennWell Books (2003).

[151] Donald W Peaceman, *Fundamentals of numerical reservoir simulation*, Elsevier (1977).

[152] Mojdeh Delshad and Gary A Pope, "Comparison of the three-phase oil relative permeability models", *Transport in Porous Media* **4**(1), pp. 59–83 (1989).

[153] SE Buckley and MC Leverett, "Mechanism of fluid displacement in sands", *Transactions of the American Institute of Mining Engineers* **146** (1941).

[154] Donald W Peaceman, "Interpretation of well-block pressures in numerical reservoir simulation with nonsquare grid blocks and anisotropic per-

meability", *Society of Petroleum Engineers Journal* **23**(03), pp. 531–543 (1983).

[155] A Pavlov, A Pogromsky, Nathan van de Wouw, and Henk Nijmeijer, "Convergent dynamics, a tribute to Boris Pavlovich Demidovich", *Systems & Control Letters* **52**(3), pp. 257–261 (2004).

[156] Winfried Lohmiller and Jean-Jacques E Slotine, "On contraction analysis for non-linear systems", *Automatica* **34**(6), pp. 683–696 (1998).

[157] Winfried Lohmiller and Jean-Jacques E Slotine, "Nonlinear process control using contraction theory", *AIChE journal* **46**(3), pp. 588–596 (2000).

[158] Wei Wang and Jean-Jacques E Slotine, "Contraction analysis of time-delayed communications and group cooperation", *Automatic Control, IEEE Transactions on* **51**(4), pp. 712–717 (2006).